Advances in micro-structured optical fibres and their applications

Wang, Aimin

Award date:
2007

Awarding institution:
University of Bath

ADVANCES IN MICROSTRUCTURED OPTICAL FIBRES AND THEIR APPLICATIONS

Submitted by Aimin Wang
for the degree of
Doctor of Philosophy
of the University of Bath
2007

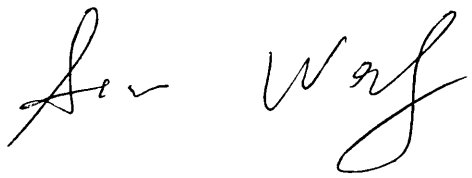

ProQuest LLC
789 East Eisenhower Parkway
P.O. Box 1346
Ann Arbor, MI 48106-1346

Abstract

This thesis describes the fabrications, characterisations, and the related applications of four different microstructured optical fibres: a highly birefringent lamellar core fibre, two kinds of all-solid photonic bandgap fibres based on circular and rectangular high-index cladding rods respectively, and a highly nonlinear photonic crystal fibre formed from tellurite glass.

A polarisation-maintaining fibre, in which the birefringence is due to artificially introduced anisotropy in the core material, was fabricated and characterised. The beat length was measured by direct observation at three different wavelengths, giving a shortest result of 85 μm at a wavelength of 543 nm. The measured phase-index birefringence is about one third of that expected, which is explained by diffusion between the core layers, which are each less than 200 nm thick. By taking account of this diffusion, we can accurately model the experimental beat length and differential group delay over a wide wavelength range.

An all-solid photonic bandgap fibre was incorporated in a Neodymium fibre laser to suppress the four-level laser transition $^4F_{3/2}$-$^4I_{11/2}$. Lasing at 907 nm on the three-level transition $^4F_{3/2}$-$^4I_{9/2}$ was demonstrated when pumping at 808 nm. The maximum slope efficiency obtained was 32% with a threshold pump power of 70 mW.

Experimental measurements of all-solid photonic bandgap fibres based on circular high index cladding rods revealed an unexpected variation of bend loss across different bandgaps. This behaviour was confirmed by calculations of photonic band structure, and explained with reference to the differing field distributions of the modes of the cladding rods. Another kind of all-solid photonic bandgap fibre based on an array of oriented rectangular rods with different symmetry was fabricated and characterised. Observed near-field patterns of cladding modes clearly identify the cut-off rod modes at the bandgap edges. The bend losses in this fibre depend on the bend direction, and can be understood by the directional coupling properties of the different rod modes and the modelled density of cladding states.

A highly nonlinear tellurite photonic crystal fibre with zero dispersion wavelength of 1.4 μm was fabricated and characterised. High nonlinearity and high transmission coefficient in the mid-infrared region make this fibre quite useful to generate broad mid-infrared supercontinuum when pumped with a mode-locked Er fibre laser system. Pumping with the similar femtosecond pulses (to those produced with an Er fibre laser system) using an OPA generated supercontinuum, which extended to 2.8 μm at the long wavelength edge.

Acknowledgements

There are a lot of people I should thank for their help and support both in my PhD work and in the three years of my oversea life in UK.

First of all, I would like to thank my supervisor, Jonathan Knight, who provided me this chance to work in the Centre for Photonics and Photonic Materials (CPPM) in Bath, for making me clear what research work would be like, and for all his help, support, suggestions, ideas and research attitudes, which are very helpful for both my future work and life.

Thank must go to Alan George, a fibre fabrication expert, who provided me with many ideas and assistances in fibre fabrications, and for the time he spent proof reading this thesis.

To David Bird and Greg Pearce for their powerful band structures codes which enabled me to easily carry out the related numerical simulations.

To Tim Birks, William Wadsworth, Toshiki Taru and Alexey Yulin for their very inspiring and helpful discussions.

To Kevin Cook and Jim Stone for proof reading this thesis to make it readable.

To Wendy Lambson for her help in glass plate polishing and HF etching.

To Fetah Benabid, Sergio G. Leon-Saval, Francois Couny and Phil Light for their generous help in the laboratories.

To Feng Luan, Wei Ding, Chunle Xiong and Ke Lai, my chinese friends in this group, for being so supportive during the course of my PhD study. Without you, the work would have become difficult and life boring.

In fact I would like to thank everyone in the CPPM for making my PhD enjoyable.

Finally, I would like to thank my wife, Zhou Jin, and my parents. Even though they could not accompany me for the last 38 months, the support from them had alway inspirited me to finish my PhD as soon as possible.

Contents

List of Figures

List of Tables

Chapter 1

Introduction

Optical fibres are cylindrical waveguides composed of dielectric materials, which guide light from one end to the other. Starting with basic signal transmission experiments based on silica glass optical fibres in the 1960s [1], their rapid development has resulted in the emergence of a multibillion dollar industry, establishing silica-glass fibre based communication networks around the world. This spectacular achievement is due to the remarkable properties of optical fibres. Low-loss propagation at optical frequencies (reaching 0.15 dB/km at the wavelength of 1550 nm) and high bandwidth allow high-bit-rate signals to be transmitted and received over long distances. Immunity to external electromagnetic interferences makes fibres able to work in almost any environment. Furthermore, they are formed from abundant and inexpensive silica glass materials, and their flexibility and strength have contributed to the economic feasibility of replacing coaxial copper system. Optical fibres are also broadly used in many other application areas, such as optical imaging and various types of sensors. To satisfy the different application requirements, glass materials of optical fibres can be selected, and the geometries of fibre structures can be designed and realized in the fibre's fabrication.

Although a variety of optical fibres are available for different applications, the adjustable design parameters for a conventional single-mode fibre are limited to the core diameter and the index difference, until recently continuing technological advances in microstructure fabrication open new vistas in optical fibre engineering and design. The main family members of these newly-developed microstructured

optical fibres, which have periodically patterned structures with a periodicity of the same order of magnitude (μm) as the light wavelength, are referred to as Photonic Crystal Fibres (PCFs) [2, 3]. Corresponding to different kinds of microstructured fibre cladding, the PCFs can have different guiding mechanisms, which are quite different from conventional optical fibres. According to different guiding mechanisms, PCFs can be divided into two categories: Index Guiding PCFs (with modified total internal reflection guidance) and Photonic Bandgap Fibres (PBGFs with bandgap guidance). The photonic crystal structures and their abundant variations endow the microstructured optical fibres with many novel optical properties and broad applicabilities in various application areas.

During the course of my PhD research, I have fabricated and characterised four different kinds of microstructured fibres. Their guiding mechanisms, optical properties, and the related applications in linear and nonlinear optics will be introduced in this thesis. Chapter 2 reviews previous work in conventional optical fibres, including guiding mechanism, linear and nonlinear effects, and their fabrication methods. Chapter 3 provides an overview of recently developed PCFs, mainly focusing on the guiding mechanisms, novel properties, state-of-the-art fabrication techniques, and their developments along the time scale. Chapters 4 to 7 present the main body of my PhD work. Chapter 4 presents a fabricated highly birefringent conventional optical fibre, whose high birefringence is introduced by artificially structuring the core on a sub-wavelength scale. I have realized this novel kind of form birefringence for the first time in an optical fibre with the birefringence reaching 6.4×10^{-3} at the wavelength of 543 nm, and it is the highest birefringence reported in a single mode optical fibre till now. I selected the suitable commercial silicate glasses, fabricated and characterised this lamellar core fibre. The birefringence and differential group delay (DGD) modelling for this fibre was also accomplished by myself. A silica glass all-solid PBGF is introduced in Chapter 5, which was used in a Neodymium (Nd) fibre laser system to demonstrated its excellent in-line optical filtering function of PBGF for the first time. The competitive four level transition of Nd doped fibre was completely suppressed and robust three level lasing was obtained. Compared to use of a W-index fibre, which was used by previous researchers, the PBGF has a high wavelength discrimination, and in principle could also be used to suppress gain at shorter wavelengths, which is not possible with the W-type fibre. I designed and fabricated this all-solid PBGF, and set up a Nd fibre laser system incorporating our PBGF as an optical filter. This kind of low-index-contrast all-solid

PBGF with low-index contrast is quite useful to understand the nature of photonic bandgaps, especially bend loss, which is hard to be observed in hollow-core PBGF. I designed and fabricated all-solid PBGFs with 1% and 2% index contrast, and first observed the novel bend losses for different bandgaps. The related work is described as part of Chapter 6. Chapter 6 mainly demonstrates another all-solid PBGF with different symmetry of high index cladding rods. Previous research only concentrated on all-solid PBGF fibres in which the raised-index cladding elements were circular. I have designed, fabricated and characterised a new kind of all-solid PBGF based on an array of oriented rectangular high-index rods. Arising from this different symmetry, directional bend losses, relative to the orientation of the rectangular rods, have been expected and observed, which was explained according to the density of states of the cladding (Dr. G.J. Pearce did this calculation) and the directional coupling properties of different cladding rod modes. Chapter 8 introduces a highly nonlinear extruded PCF formed from tellurite glass. The high nonlinearity and high transmission coefficient at mid-infrared region of tellurite glass makes this kind of tellurite PCF a good candidate for mid-infrared supercontinuum generation. I fabricated the tellurite glasses, did glass extrusion and fabricated this small-core tellurite PCF. With a pump of femtosecond pulse laser at a wavelength of 1.5 μm a broad supercontinuum spectrum from 0.75-2.8 μm has also been measured by myself. Chapter 8 is the summary of this thesis. And the appendix shows the publication list of my PhD work during this thesis.

Chapter 2

Review of optical fibres

2.1 Introduction

At the heart of a lightwave communication system is the silica glass optical fibre, which acts as the transmission channel carrying the light beam loaded with information. It is a flexible glass waveguide with cylindrical symmetry, consisting of a high-index dielectric core (usually doped silica) and a lower refractive index cladding. Guided light can propagate along this high index core with fixed transverse field distributions. With different glasses as the material and different geometry designs of its core and cladding, an optical fibre can behave with different optical properties, suitable for many application areas, such as optical imaging and various types of sensors.

This chapter briefly reviews the main aspects of linear and nonlinear fibre optics, focusing on conventional optical fibres. The first two sections outline the guidance mechanism and fundamental linear characterisations of conventional optical fibres. The summary of nonlinear optical processes in optical fibres is discussed in Section 2.4. The last section provides the manufacturing techniques used to fabricate conventional optical fibres.

2.2 Guiding mechanism

A conventional optical fibre with cylindrical symmetry is composed of the central core region (refractive index n_{core}) and its surrounding lower refractive index cladding ($n_{clad} < n_{core}$). Light launched into one end of the fibre can be confined to the waveguiding core and propagate along the fibre to the other end. This guidance is achieved by the phenomenon of *Total Internal Reflection* (TIR). A ray of light will be totally reflected at a boundary between two dielectric media when incident from the medium with higher refractive index at an angle of incidence greater than a critical value θ_c determined by Snell's Law:

$$\theta_c = \arcsin(n_{clad}/n_{core}) \tag{2.1}$$

A schematic diagram of an optical fibre structure and total internal reflection is provided in Fig.2.1.

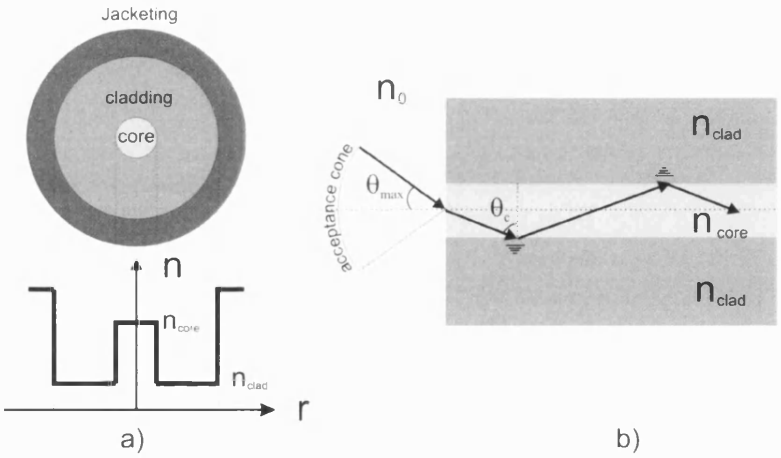

Figure 2.1: (a) Schematic of the cross-section and refractive index profile of a conventional step-index optical fibre; (b) Guiding mechanism. The light with input angle smaller than θ_{max} can be guided in the optical fibre.

2.3 Linear properties of optical fibres

The linear properties of guided light in optical fibres are summarized in this section.

2.3.1 Fibre modes & Single mode operation

Fibre mode

Modes are stable patterns that optical waves form as they pass through a waveguide. To discuss the guided modes in an optical fibre, which is an excellent approximation of a two-dimensional structure without variations along its length, it is useful to consider the β-value in the fibre - the component of the total propagation constant which is along the fibre axis. Note that when light with free-space wavevector k encounters an interface between two materials with different refractive indices, the component of the wavevector parallel to the interface remains unchanged during the interaction. Since all interfaces in a fibre are parallel to the fibre axis except the input and output faces, light launched into the fibre with a given value of β should maintain that value until it leaves the fibre. The largest value of β that can exist in an infinite homogeneous medium with refractive index n is $\beta = nk_0$ (k_0 is the vacuum wavevector), with all smaller values allowed. The vacuum wavevector, $k_0 = 2\pi/\lambda = \omega/c$, where λ is the free-space wavelength of the light, c is the vacuum light speed, and ω is the light frequency. An effective modal index n_{eff} can be derived from β-value by β/k. To form a guided mode in a conventional fibre, the refractive index of the core is raised to make the core modes have higher β-values, which cannot propagate in the cladding.

The number and intensity profiles of these guided modes depend on the light wavelength and the physical parameters of the waveguide. Mathematically, these modes correspond to the solutions of Maxwell's equations, which satisfy boundary conditions of the waveguide structure in an optical fibre. However, these exact solutions are complicated to evaluate, and the theory can be simplified for a weakly guiding optical fibre [4] ($\Delta = (n_{core} - n_{clad})/n_{clad} \ll 1$), which is valid for typical telecommunication grade fibres. In such a fibre, the field components of a mode in the direction of propagation are small compared to components perpendicular to that direction. The launched linearly polarised light can maintain its linear polarisation along the fibre. *Linearly Polarised Modes* are used to describe the guided modes under this weakly guiding approximation. These are designated LP_{lm}, where the integers l and m respectively describe the azimuthal and radial variations of the field in the core.

Normalised Frequency (V parameter) and *Normalised Propagation Constant* (b)

are useful to describe the mode properties in an optical fibre. The normalised frequency is defined as [5]:

$$V = \frac{2\pi r}{\lambda}\sqrt{n_{core}^2 - n_{clad}^2} \tag{2.2}$$

where r is the radius of the core, and the normalised propagation constant b is given by [4]

$$b = [(\beta^2/k_0^2) - n_{clad}^2]/(n_{core}^2 - n_{clad}^2) \approx [(\beta/k_0) - n_{clad}]/(n_{core} - n_{clad}) \tag{2.3}$$

The normalised propagation constants of the first 8 low order LP modes are shown in Fig. 2.2 [4].

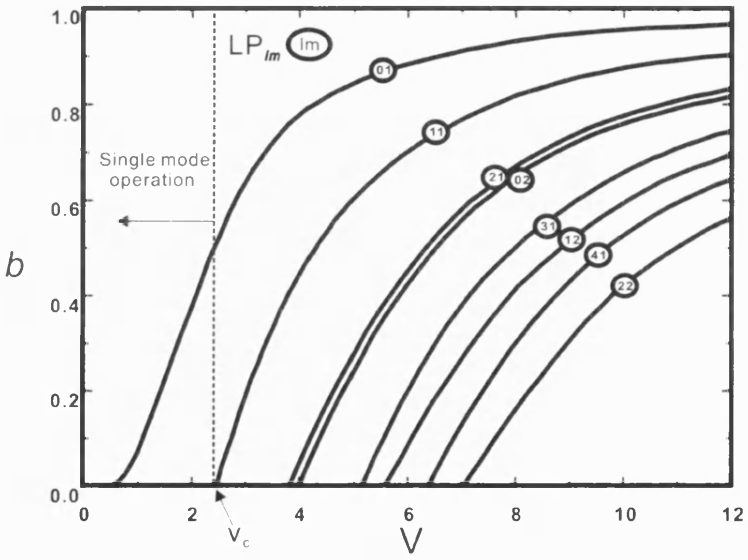

Figure 2.2: Normalised propagation constant b as a function of the normalised frequency V (modified from [4]).

Single mode operation

When a mode is not permitted to be confined in the fibre core any more, it is called *Cut-off*. Except for the fundamental mode (LP_{01}), every mode has a cut-off condition. To confirm the single mode operation in a conventional step-index fibre, $V < V_c = 2.405$ is necessary (see Fig. 2.2). This value is given by the first zero of the J_0 Bessel function (one solution to the cylindrically symmetric waveguide) [5]. Optical fibres designed to satisfy this condition are called single-mode fibres. The cut-off wavelength (λ_c) for a single-mode fibre can be obtained

from Eq.(2.2)

$$\lambda_c = \frac{2\pi r}{2.405}\sqrt{n_{core}^2 - n_{clad}^2} \tag{2.4}$$

When the wavelength is longer than λ_c, the fibre become multimode. In practice, even though $V/V_c < 1$ must be satisfied for the single mode operation, V/V_c cannot be too small, because the fibre microbending losses increase as it becomes smaller. Hence the typical V-value is chosen to be close to V_c. For a typical value of index different $n_{core} - n_{clad} = 0.005$, the cut-off wavelength λ_c is chosen to be about 1.2 μm, with the core diameter of about 8-9 μm.

Compared to the multimode optical fibre, the single mode fibre is preferable as it retains the fidelity of each light pulse over longer distances and exhibits no dispersion caused by multiple guided modes; thus more information can be transmitted per unit time, providing a broader bandwidth.

2.3.2 Numerical aperture

Numerical aperture is an expression of the extent of the fibre's ability to accept, in its bound modes, non-normal incident rays. (American National Standard T1.523-2001)

Defined as the sine of the maximum angle (measured outside the fibre with respect to the z axis) of an incident light ray, the *numerical aperture* can be expressed as:

$$NA = n_0 \sin\theta_{max} = \sqrt{(n_{core}^2 - n_{clad}^2)} \tag{2.5}$$

Normally light is launched in to fibres from air, so n_0 is usually 1. In a multimode fibre, NA can be explained by using the geometric optics approach and Snell's Law (refer to Fig. 2.1(b)): only a light ray with a sufficiently small incident angle ($\theta < \theta_{max}$) can be coupled in and out of the fibre. The NA of a single mode fibre can be understood as the divergence of the beam, analogous to the diffraction pattern from an aperture.

2.3.3 Loss

Silica material absorption, contaminations absorption bands and Rayleigh scattering are the main contributors for the loss spectrum of a silica glass optical fibre, shown in Fig. 2.3 [6].

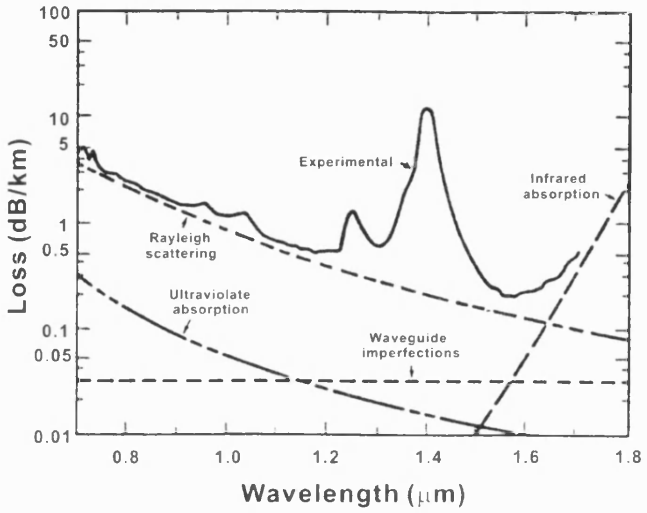

Figure 2.3: Loss spectrum of a single-mode fibre produced in 1979. Wavelength dependence of several fundamental loss mechanisms is also shown [6].

The absorption losses are due to the interaction of the light with the material when propagating in the glass. For silica glass resonance absorption occurs in the ultraviolet (electronic resonance, below 0.5 μm) and mid-infrared (vibrational resonance, beyond 2 μm) regions, with little light being absorbed in the middle wavelength region from 0.5-2.0 μm. However, impurities with their own absorption bands can significantly affect the fibre attenuation spectrum even by a small amount. From a practical point of view, the most important impurity in a silica glass optical fibre is the OH ion, which enters the glass in the form of water vapor. In Fig. 2.3, the attenuation peaks near 1.4 μm, 1.23 μm and 0.95 μm all originate from OH-absorption. Transition-metal impurities such as Fe, Cu, Co, Ni, Mn, and Cr absorb strongly in the wavelength range 0.6-1.6 μm, contributing to the fibre impurity loss. Their amount should be reduced to below 1 part per billion to obtain a loss level below 1 dB/km. Such high-purity silica can be obtained by using modern techniques. Rayleigh scattering arises from density fluctuations frozen into the fused silica during manufacture, which scatter light in all directions. These fluctuations are caused by small (compared to the wavelength of

light) defects in the structure, such as irregularities produced during the fabrication process, and the dopants which are used to modify the refractive index of the core glass. This fundamental scattering loss varies as λ^{-4} and is dominant at short wavelengths. The combined effects of these wavelength-dependent absorption and scattering mechanisms make the telecommunication industry focus on the low loss windows around 1.3 and 1.55 μm (see Fig. 2.3). Modern fibre transmission loss at 1.55 μm has been decreased to 0.15 dB/km.

Confinement loss and bend loss also contribute to the fibre losses. Confinement loss expresses the inability of the core to confine the guided mode. The low index step between core and cladding and size irregularities can cause the guided core modes to be coupled to the cladding modes. The finite cladding allows these energy to leave the fibre system. Bend loss originates from the resonant coupling of light from the core to radiation modes in the cladding on the outside of a bend. In a straight well-confined optical fibre this coupling does not occur because the radiation modes have a lower effective index n_{eff} than the core mode. The bent fibre can be modelled as a straight fibre with a modified refractive index profile:

$$n(x) = n_0(x)[1 + (1 - \chi)x/R] \tag{2.6}$$

where x is the linear coordinate outward from the local centre of curvature with an origin at the centre of the fibre, $n_0(x)$ is the unmodified index profile, R is the radius of curvature, and χ a correction due to the elasto-optic effect (χ =0.22 for silica) [7]. Hence the modified index increases linearly with distance on the outside of a bend. At some point, when it rises above the n_{eff} of the core mode, coupling can occur to radiation modes causing the bend loss. Working at shorter wavelengths and increasing the index contrast can improve the fibre resistance to bend loss.

2.3.4 Dispersion

In an optical fibre, dispersion is used to describe any process by which a propagating optical signal is degraded due to the various wave frequencies of the signal having different propagation velocities. A monochromatic wave propagates in an optical fibre with a speed of $c/n(\omega) = \omega/\beta$, which is known as the *Phase Velocity* v_p. However, real optical signals are usually optical pulses, which are composed

of a group of frequencies very close to each other around a central frequency ω_0. The envelope of an optical pulse moves at the speed of $c/n_g = (\frac{d\omega}{d\beta})_{\omega=\omega_0}$, called its *Group Velocity* v_g (n_g is the group refractive index). In fact, group velocity is a function of frequency, which is directly responsible for pulse broadening in an optical fibre. This phenomenon is referred to as *Group Velocity Dispersion* (*GVD*).

By expanding the mode propagation constant $\beta(\omega)$ in a Taylor series about the central frequency ω_0, the dispersion can be written as [8]:

$$\beta(\omega) = n(\omega)\frac{\omega}{c} = \beta_0 + \beta_1(\omega - \omega_0) + \frac{1}{2}\beta_2(\omega - \omega_0)^2 + ... \tag{2.7}$$

where

$$\beta_m = \left(\frac{d^m\beta}{d\omega^m}\right)_{\omega=\omega_0} \qquad (m = 1, 2, 3, ...) \tag{2.8}$$

furthermore,

$$\beta_1 = \frac{1}{c}\left[n + \omega\frac{dn}{d\omega}\right] = \frac{n_g}{c} = \frac{1}{v_g} \tag{2.9}$$

$$\beta_2 = \frac{d\beta_1}{d\omega} = \frac{d\frac{1}{v_g}}{d\omega} = \frac{1}{c}\left(2\frac{dn}{d\omega} + \omega\frac{d^2n}{d\omega^2}\right) \tag{2.10}$$

β_1 is inversely proportional to group velocity v_g and proportional to group refractive index n_g. β_2, known as the *GVD Parameter*, is related to the group velocity variation with frequency. Fig. 2.4 [8] presents β_2 against wavelength for silica glass. The wavelength at which β_2 is zero is called the *Zero Dispersion Wavelength* (ZDW). β_m with $m > 2$ are usually referred to as the higher-order dispersion coefficients. In fibre optics, the *Dispersion Parameter* D is more convenient to describe the group velocity dispersion against wavelength, defined as $D = \frac{d\beta_1}{d\lambda}$ and expressed in units of ps·nm^{-1}km^{-1}. The relation between D and β_2 can be obtained by:

$$D = -\frac{2\pi c}{\lambda^2}\beta_2 \approx \frac{\lambda}{c}\frac{d^2n}{d\lambda^2} \tag{2.11}$$

In an optical waveguide, the dispersion effect mainly arises from two mechanisms: (1) from material refractive index variation with wavelength (*Material Dispersion*) and (2) from changes in mode confinement with wavelength in the waveguide (*Waveguide Dispersion*). Compared to material dispersion, waveguide

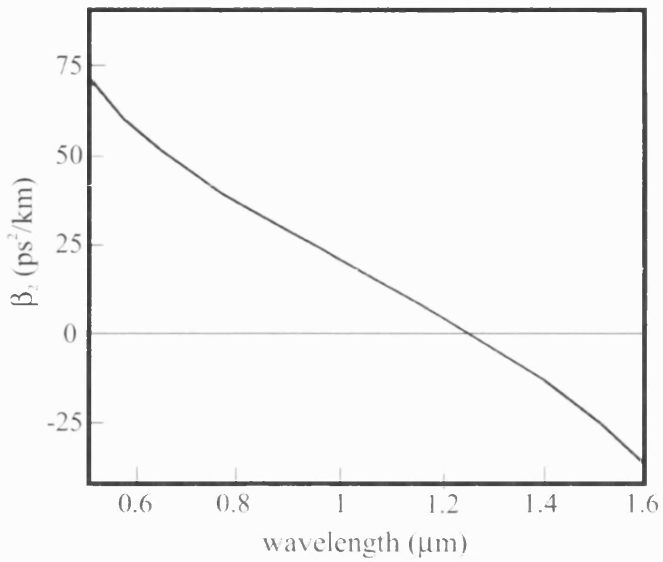

Figure 2.4: β_2 with the function of wavelength for fused silica [8].

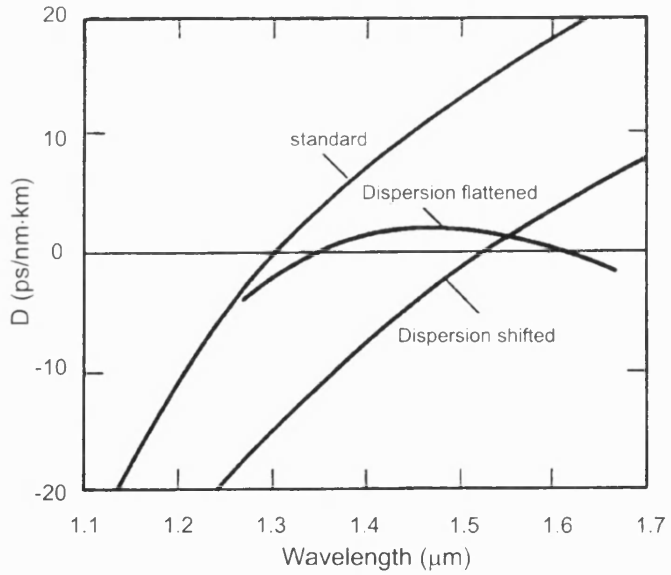

Figure 2.5: Typical wavelength dependence of dispersion parameter D for standard, dispersion shifted and dispersion flattened fibres [6].

dispersion is easier to modify to engineer the desired dispersion properties. By controlling the core radius and the index profile, different kinds of conventional fibre with novel dispersion properties have been designed and manufactured, such as the dispersion flattened fibre and the dispersion shifted fibre, whose dispersion curves are shown in Fig. 2.5 [6].

2.3.5 Birefringence

A single mode optical fibre is not truly single mode. It can guide two degenerate modes polarised in two orthogonal directions. In a stress-free fibre with perfectly cylindrical symmetry, a mode excited with its polarisation in x direction would not couple to the mode with the orthogonal y-polarisation state. In real fibres, limited by the practical fabrication process, small departures from cylindrical symmetry, such as random fluctuations in the core shape and size, are unavoidable. They may also experience nonuniform stresses in practice due to fibre bends or twists. These effects break the mode degeneracy, and the mode propagation constant β will become slightly different for modes polarised in the x and y directions. This is known as modal birefringence of optical fibres. The degree of modal birefringence is defined as [8]:

$$B_m = \frac{|\beta_x - \beta_y|}{k_0} = |n_x - n_y| \tag{2.12}$$

where β_x and β_y are the propagation constants of these two orthogonally polarised modes and n_x and n_y are their modal refractive indices. For a fibre with given value of B_m, the two polarised modes exchange their powers in a periodic fashion as they propagate along the fibre with a period of

$$L_B = \frac{2\pi}{|\beta_x - \beta_y|} = \frac{\lambda}{|n_x - n_y|} = \frac{\lambda}{B_m} \tag{2.13}$$

which is called the *Beat Length*. The axis along which the modal index is smaller is called the fast axis, and the axis with larger modal index is called slow axis.

In a standard optical fibre, typically, $B_m \approx 10^{-7}$, and $L_B \approx 10$ m at a wavelength of 1 μm. The birefringence can always change randomly under the influence of unintentional factors, so light launched into such a fibre with linear polarisation can rapidly reach a state of arbitrary polarisation.

In a highly birefringent fibre ($B_m > 10^{-4}$), linearly polarised light can maintain its polarisation state during propagation when its linear polarisation direction is along one principal axis, either the slow axis or fast axis. Otherwise, its polarisation state would continuously change along the fibre length, from linear to elliptical and back to linear again with a periodic beat length. Fig. 2.6 [8] schematically shows this kind of polarisation state change when linear polarised light is coupled into an optical fibre at 45° with respect to the slow and fast axes. Such a highly birefringent fibre is called *Polarisation Maintaining Fibre* (PM fibre). The large birefringence (up to 10^{-4}) is introduced intentionally in these fibres, dominating the random birefringence fluctuations ($\sim 10^{-7}$) and thus preserving the polarisation state. In other words, due to the big difference between the two orthogonal modal propagation constants (β_x and β_y), a mode excited with its polarisation in the slow axis (or the fast axis) will not couple to the mode with the orthogonal polarisation state, even under the influence of random external birefringence.

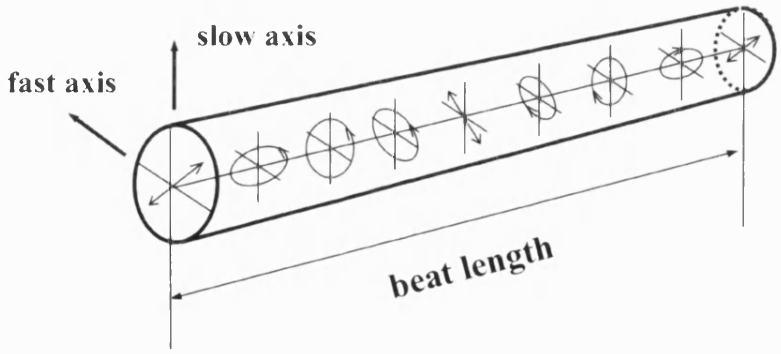

Figure 2.6: Polarisation state evolution in a fibre with birefringence when linear polarised light is coupled into an optical fibre at 45° with respect to the slow and fast axes.

Two methods have been used to achieve the required birefringence. The shape of the refractive index profile defining the fibre core has been made non-circular (shape or form birefringence) or the material forming the fibre has itself been made birefringent by introducing stresses (stress birefringence) [9, 10]. Panda [11] and bow-tie fibres [12] achieve high birefringence through induced stress, while fibres with an elliptical core [13] and side air holes [14] present a high birefringence due to asymmetry in core geometry. Fig. 2.7 shows schematic cross sections of three different commercially available PM fibres. For an elliptical core

PM fibre, the magnitude of the birefringence depends on the geometry of the core and the core-cladding index difference [15]. For Panda and Bow-Tie PM fibres the birefringence relies on the stress imposed on the structure as well as on the core-cladding index difference. The large directional stress distribution, which causes the final fibre birefringence, is normally produced by using two rods of borosilicate glass inserted on either side of the core region before the preform is drawn to fibre. Typically, $B_m \approx 10^{-4}$, and $L_B \approx 1$ cm at a wavelength of 1 μm for such fibres. In Chapter 4, a different type of form birefringence will be introduced in our highly birefringent lamellar core fibre, which has the largest birefringence yet reported in an single-mode optical fibre.

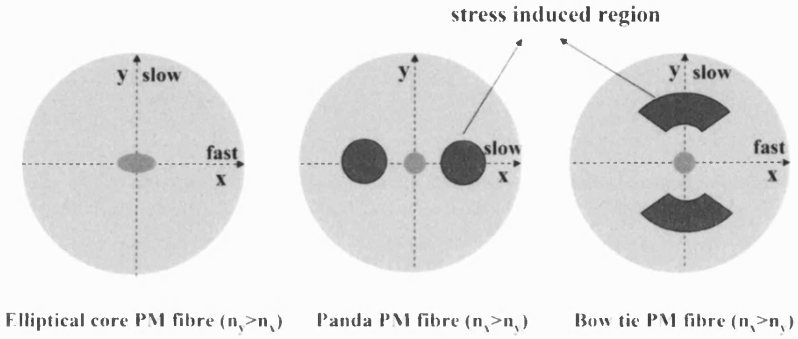

Figure 2.7: Schematic cross sections of three different commercial PM fibres.

2.4 Nonlinear effects in fibres

The response of any dielectric to light becomes nonlinear for intense electromagnetic fields, and optical fibres are no exception. The typical fibre material silica, has a relatively small nonlinear refractive index, but the comparatively small cross section of optical fibres and the long propagation length make nonlinear effects important in practical telecommunication system. This section provides a brief summary of some of the main concepts in nonlinear fibre optics, which are partly based on material from the book *Nonlinear Fiber Optics* written by G.P. Agrawal [8].

2.4.1 Origin of optical nonlinearity in fibres

The nonlinear response of a dielectric medium to an externally applied electric field **E** can be described through the polarisation vector **P**, which is induced by the electric dipoles. The general relation between polarisation **P** and electric field **E** can be expressed as [16]:

$$\mathbf{P} = \epsilon_0 \left(\chi^{(1)} \cdot \mathbf{E} + \chi^{(2)} : \mathbf{EE} + \chi^{(3)} : \mathbf{EEE} + \cdots \right) \tag{2.14}$$

where ϵ_0 is the vacuum permittivity and $\chi^{(j)}$ $(j = 1, 2, \ldots)$ is the j^{th} order susceptibility, a tensor of rank $(j+1)$. $\chi^{(1)}$, a second rank tensor, describes linear polarisation $\mathbf{P}_L$ and has the largest contribution to **P**. Terms of second and higher orders in Eq.(2.14) are collectively referred to as the nonlinear polarisation, $\mathbf{P}_{NL}$. Most work in nonlinear optics involves second and third order processes, characterised by $\chi^{(2)}$ and $\chi^{(3)}$. Higher order processes are weak, and generally unimportant in practical applications.

As a tensor of rank $(j+1)$, $\chi^{(j)}$ contains $3^{(j+1)}$ elements [17], which make the expression of **P** very complicated. In fact, the symmetry of materials can reduce the number of independent terms. In isotropic media, such as glass materials, $\chi^{(2)}$ vanishes due to the inversion symmetry, and the number of independent elements in $\chi^{(1)}$ and $\chi^{(3)}$ is reduced to only one (all light wavelengths are far from any resonance of silica). As discussed above, we consider only the lowest order nonlinearity, and express the polarisation intensity as:

$$P = \epsilon_0 \left(\chi^{(1)} E + \chi^{(3)} E^3 \right) = P_L + P_{NL} \tag{2.15}$$

where P_{NL} is the nonlinear response of the fibre material to the applied electric field.

2.4.2 Nonlinear fibre parameters

Nonlinear refractive index n_2

The nonlinear response of P_{NL} is related to a refractive index change in the fibre.

The nonlinear part of the refractive index can be written as:

$$\Delta n = n_2 |E|^2 \tag{2.16}$$

where $|E|^2$ is the optical intensity inside the fibre, and n_2 is called the *Nonlinear Refractive Index*, related to $\chi^{(3)}$ by the relation

$$n_2 = \frac{3}{8n} Re(\chi^{(3)}_{xxxx}) \tag{2.17}$$

where Re means real part, and the optical field is assumed to be linearly polarised so that only one component $\chi^{(3)}_{xxxx}$ contributes to the nonlinear refractive index.

Effective area A_{eff}

Although confined by the core-cladding boundary of an optical fibre, the light energy guided in the core penetrates into the cladding layer for a short distance and does not have a uniform intensity. *Effective Area* (A_{eff}) is used to express this property and is defined as:

$$A_{eff} = \frac{(\int\int_{-\infty}^{\infty} |F(x,y)|^2 dxdy)^2}{\int\int_{-\infty}^{\infty} |F(x,y)|^4 dxdy} \tag{2.18}$$

where $F(x,y)$ is the electric field distribution and $|F(x,y)|^2$ is the intensity of the near-field for the fundamental fibre mode. The fundamental fibre mode is often approximated by a Gaussian distribution of the form $F(x,y) \approx exp[-(x^2 + y^2)/w^2])$, where w is the mode width. It can be obtained by fitting the exact distribution to a Gaussian form. Fig. 2.8 [8] shows the dependence of w/r on the fibre parameter V defined by Eq.(2.2), where r is the radius of the fibre core. The effective area can be written as $A_{eff} = \pi w^2$. Therefore, the effective area of an optical fibre can be obtained according to the calculated V-value from Eq.(2.2) and Fig. 2.8.

Nonlinear coefficient γ

When studying nonlinear effects in optical fibres, nonlinear coefficient γ is an important nonlinear parameter of an optical fibre and is defined as:

$$\gamma = \frac{n_2 \omega_0}{c A_{eff}} \tag{2.19}$$

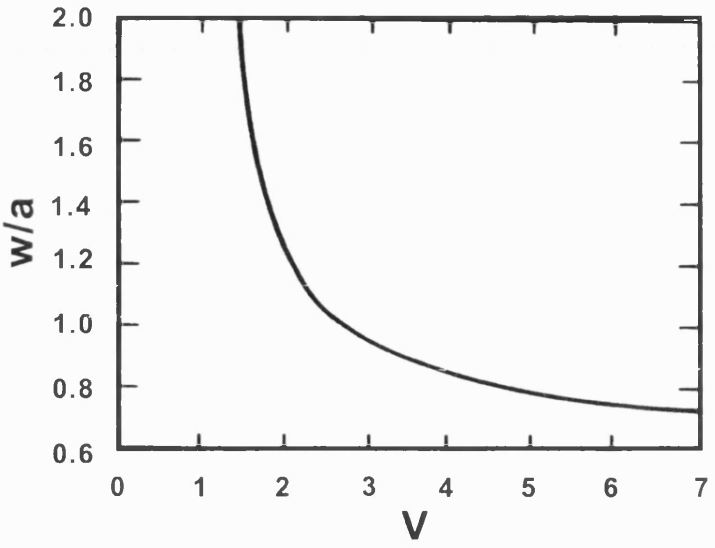

Figure 2.8: Variation of mode-width parameter w with normalized frequency V [8].

High nonlinear coefficient γ can be obtained by choosing a fibre glass material with high nonlinear refractive index and designing the fibre to have a small A_{eff}.

For silica glass, the nonlinear refractive index n_2 =2.2×10^{-20}m^2/W [18]. Typically, for a conventional optical fibre, A_{eff} can vary in the range 20-100 μm^2 in the 1.5 μm region. As a result, nonlinear coefficient γ will have values in the range 1-10 km^{-1}W^{-1}.

2.4.3 Stimulated inelastic scattering processes

In elastic scattering processes, the photon energy (or the frequency) of scattered light is unchanged, as in Rayleigh scattering. By contrast, inelastic scattering processes can change the frequency of the scattered light because the optical field can transfer part of its energy to the nonlinear medium. Two examples of inelastic scattering are *Stimulated Raman Scattering* (*SRS*) and *Stimulated Brillouin Scattering* (*SBS*).

During the SRS process, some pump photons give up their energy to generate other photons with reduced energy. The remaining energy is absorbed as excited

vibrational states of the glass material. The photons can be scattered to higher frequency photons as well, by absorbing optical phonons with the correct energy and momentum. If the scattered photon energy is lower than the pump frequency, it is referred to as the Stokes wave; if scattered photon energy is higher, it is referred to as the anti-Stokes wave. Brillouin scattering is very similar to Raman scattering. The main difference is that optical phonons participate in Raman scattering, whereas acoustic phonons participate in Brillouin scattering.

2.4.4 Parametric processes

In the stimulated scattering processes, optical fibres play an active role through molecular vibrations or density variations. In some other nonlinear processes, optical fibres play a passive role, only mediating the interaction of a number of optical waves. These processes are referred to as *Parametric Processes.* The parametric processes are directly related to the nonlinear polarisation $\mathbf{P}_{NL}$. In optical fibres $\chi^{(2)}$ is zero, and $\mathbf{P}_{NL}$ can be expressed as $\mathbf{P}_{NL} = \epsilon_0 \chi^{(3)} \vdots \mathbf{EEE}$. The third-order parametric processes generally involve nonlinear interactions of four optical waves, with frequencies ω_1, ω_2, ω_3 and ω_4, and include phenomena such as third-harmonic generation, *Four Wave Mixing* (*FWM*), and parametric amplification. FWM in optical fibres has been studied extensively as it is quite efficient at generating new frequencies, and will be discussed in this section.

Significant FWM occurs only if matchings of the frequencies as well as of the wave vectors are satisfied in an optical fibre. The latter requirement is often referred to as *Phase Matching.* There are two types of FWM process. In one process, three photons $(\omega_1, \omega_2, \omega_3)$ transfer their energy to a single photon at the frequency of ω_4 $(\omega_4 = \omega_1 + \omega_2 + \omega_3)$. For this process it is difficult to satisfy the phase-matching condition in an optical fibre with high efficiency. The other process is corresponding to the case in which two photons (ω_1, ω_2) are annihilated and simultaneously two new photons (ω_3, ω_4) are generated $(\omega_3 + \omega_4 = \omega_1 + \omega_2)$. The phase matching for this process at zero power is

$$\Delta\beta = \beta_3 + \beta_4 - \beta_1 - \beta_2 = (n_3\omega_3 + n_4\omega_4 - n_1\omega_1 - n_2\omega_2)/c = 0 \qquad (2.20)$$

Phase matching for the case where $\omega_1 = \omega_2$ is comparatively easy and is the most relevant for optical fibres. This process manifests that a strong pump with

frequency ω_p creates two sidebands located symmetrically at frequencies of ω_3 and ω_4 with a frequency shift of $\Omega = \omega_3 - \omega_p = \omega_p - \omega_4$, where we assume that $\omega_3 < \omega_4$. In direct analogy with SRS, the two sidebands ω_3 and ω_4 are referred to as the Stokes and anti-Stokes bands.

2.4.5 Pulses in fibres

Nonlinear effects become increasingly important when light pulses propagate in optical fibres. The high peak intensities of pulses with widths ranging from $\sim$ 10 ns to 10 fs lead to significant enhancement of nonlinear effects. In this section, only basic concept and brief equations without detailed mathematic solution processes are introduced.

Nonlinear pulse propagation

According to the Maxwell's Equation and Eq.(2.15), the wave equation governing propagation of optical pulses in nonlinear dispersive fibres can be written in the form [8]:

$$\nabla^2\mathbf{E} - \frac{1}{c^2}\frac{\partial^2\mathbf{E}}{\partial t^2} = \mu_0\frac{\partial^2\mathbf{E}}{\partial t^2} + \mu_0\frac{\partial^2\mathbf{P}_{NL}}{\partial t^2} \tag{2.21}$$

where μ_0 is the vacuum permeability. To solve Eq.(2.21), several simplifying assumptions are made: 1) $\mathbf{P}_{NL}$ is treated as a small perturbation to $\mathbf{P}_L$, so that the perturbation theory can be used. 2) The optical field is assumed to maintain its polarisation when propagating in fibres so that a scalar approach is valid. This is not real for optical fibres (except for the PM fibre), but the approximation works very well in practice; 3) The optical field is assumed to be quasi-monochromatic, meaning pulse frequency width is smaller than its own frequency. It is valid for pulses as short as 100 fs.

Since the field distribution change little during the propagation of a pulse in optical fibres, by using the method of separation of variables, the electric field $\mathbf{E}(\mathbf{r}, t)$ can be written as

$$\mathbf{E}(\mathbf{r}, t) = \frac{1}{2}\hat{x}[F(x, y)A(z, t)e^{i(\beta_0 z - \omega_0 t)} + c.c.] \tag{2.22}$$

where $F(x, y)$ is the field distribution in the cross section of the fibre, $A(z, t)$ is

the slowly varying pulse envelope, ω_0 is the central frequency and $\beta_0 = \beta(\omega_0)$.

When solving Eq.(2.21), a frame of reference moving with the pulse at the group velocity v_g is used by making the transformation, $T = t - z/v_g$. The solution for $A(z,T)$ can be written as

$$\frac{\partial A}{\partial z} + \frac{i\beta_2}{2}\frac{\partial^2 A}{\partial t^2} + \frac{\alpha}{2}A = i\gamma|A|^2 A \tag{2.23}$$

where α is the absorption coefficient of the fibre, and the dispersion terms higher than two order are neglected. Equation (2.23) is referred to as *nonlinear Schrdöinger equation* (*NLSE*), which describes propagation of optical pulses in single-mode fibres. The effects of fibre losses (α term), dispersion (β_2 terms, Eq.(2.10)) and fibre nonlinearity (γ term, Eq.(2.19)) are all included in this equation, affecting the propagation properties of pulses in fibres.

Soliton forming

In this subsection, the effects of dispersion and nonlinearity on the soliton phenomenon in optical fibres are discussed.

As we discussed in Section 2.3.4, group velocity dispersion is purely a linear effect, which does not cause the spectrum of a pulse to change, but does cause different frequency components of a pulse to travel at slightly different speeds along the fibre. This causes pulse broadening. For the normal dispersion regime ($\beta_2 > 0$) red components travel faster, whilst for the anomalous dispersion regime ($\beta_2 < 0$) blue components travel faster.

As we discussed in Section 2.4.2, when an optical wave propagates in an optical fibre, the medium refractive index will change with light intensity in the form of $n = n_0 + n_2|E|^2$, where n_0 is the linear refractive index. Substituting this in Eq.(2.22) generates an additional time-varying phase term, which arises from the nonlinearity. This can be obtained by the form of $\delta\phi(t) = n_2 k_0 |F(x,y)|^2 |A(z,t)|^2 z$, where k_0 is the vacuum wavevector at the frequency of ω_0. This nonlinear phase shift results in a frequency shift $\delta\omega$

$$\delta\omega(t) = -\frac{\partial}{\partial t}\delta\phi(t) = -n_2 k_0 z |F(x,y)|^2 \frac{\partial}{\partial t}|A(z,t)|^2 \tag{2.24}$$

This frequency shift increases with propagation length, and can obviously be

larger than the original frequency width of a pulse causing the frequency broadening. It is also related to the pulse shape. At the leading edge of a pulse ($A(z,t)$ has a positive slope over time), $\delta\omega < 0$, so red shift occurs; At the tailing edge, where the pulse has a negative slope, blue shift happens. This phenomenon is referred to as *Self Phase Modulation* (*SPM*).

GVD causes the pulse shape to broaden while keeping the spectrum unchanged, whereas SPM does not affect the pulse shape but broadens the pulse spectrum. For a realistic optical fibre with anomalous dispersion ($\beta_2 < 0$), both GVD and SPM effects occur, and these joint effects can result in a stable pulse solution with unchanged pulse shape and spectrum, referred to as an *Optical Soliton.*

A hyperbolic secant pulse propagates in an ideal lossless optical fibre with anomalous GVD ($\beta_2 < 0$), which has the form of $A(0,T) \propto sech(T/T_0)$. Its width T_0 and peak power P_0 are chosen such that N, defined as

$$N = \sqrt{\frac{L_D}{L_{NL}}} = \left(\frac{\gamma P_0 T_0^2}{|\beta_2|}\right)^{\frac{1}{2}} \tag{2.25}$$

is an integer, where dispersion length L_D and nonlinear length L_{NL} provide the length scales over which the dispersive or nonlinear effects become important for pulse evolution along a fibre [8]. For the case of $N = 1$, GVD and SPM cancel each other, so that the pulse maintains its shape and spectrum without changing when propagating, referred to as the fundamental soliton. For $N > 1$, SPM dominates initially but GVD catches up soon. In the end the two effects cause the pulse to follow a periodic evolution pattern, referred to as *Nth-order Solitons.*

High-order effects

In the above discussions, higher-order (> 2) dispersion and stimulated inelastic scattering processes (SRS and SBS) are neglected for optical pulses propagating in an optical fibre. The high order dispersion terms become important for ultrashort pulses due to their wide bandwidth. *Soliton Self-Frequency Shift* (*SSFS*), due to intrapulse Raman scattering, was discovered when Mitschke et al and Gordon studied sub-picosecond pulses in single-mode PM optical fibres [19, 20]. They observed a continuous shift in the optical frequency of a soliton as it travelled along a fibre. When the spectrum width of the soliton is large enough (normally in silica fibres the pulse duration < 1 ps), the high-frequency components of the

pulse can amplify the low-frequency components as Raman pump. The soliton then experiences a continuous red-shift as it propagates along the fibre. *Pulse Self-steepening* and *Optical Shock* effects can also occur for ultrashort pulses. Physically, the group velocity of a pulse is intensity dependent: the high intensity peak has a slower transmission speed than the pulse wings, so that the peak tends to shift toward the trailing edge, causing self-steepening and optical shock.

2.4.6 Supercontinuum Generation

Supercontinuum Generation (*SCG*) refers to the extreme broadening of an optical spectrum as the light passes through an optical medium. This phenomenon can be explained as an interplay of all the aforementioned nonlinear effects. SCG has many applications in fields such as optical coherence tomography [21], spectroscopy and telecommunications. Compact and precise frequency chains are widely used in metrology through the use of the frequency comb, which results from the femtosecond pulse train excitation of the supercontinuum spectrum [22].

SCG occurs in many different operating regimes, and the ways in which the supercontinuum builds up can be drastically different. Two simple examples are provided here. 1). When launching ps pulses into a fibre in the normal dispersion regime [23], SRS first extends the spectrum to the long wavelength side, and then by FWM high frequency optical waves can be generated. The red shift components serving as parametric pumps can amplify the high frequency light. 2). When using fs pulses in the anomalous dispersion regime [24], the interaction of SPM and anomalous dispersion creates high order solitons. Similar results can be obtained in the normal dispersion regime, where the initial spectral broadening is attributed to SPM [24]. The contributions from other effects such as the Raman effect, self-steepening and third-order dispersion lead to fission of the higher-order soliton [25, 26, 27]. With energy emitted as blue shifted *Non-solitonic Radiation* (NSR), a fundamental soliton is formed and further red shifted due to the Raman self-frequency shift. As the pump power is further increased more self shifting solitons appear while the original one continues to move toward the long wavelength region. Since all solitons and their corresponding NSR have different central frequencies a broadband continuum is generated, whose width is increased by increasing soliton numbers.

Photonic Crystal Fibres (*PCF*) have received a lot of attention in SCG since it emerged [21, 23, 24, 25, 26, 27, 28, 29, 30, 31]. In a PCF, small effective area and control over waveguide dispersion can be easily achieved, increasing the attainable nonlinearity and allowing pumping near zero dispersion wavelength. All these novel properties of PCF will be introduced in the next chapter, and a highly nonlinear tellurite PCF used to generate mid-infrared supercontinuum will be introduced in Chapter 7.

2.5 Manufacturing methods

There are various methods to fabricate conventional types of optical fibre. Normally, the manufacturing process involves two stages. In the first stage a cylindrical preform with the desired refractive-index and geometrical profile is made. In the second stage, the preform is drawn into a fibre by feeding it into a furnace at an appropriate speed and drawing it down to fibre. These two steps are introduced in this section.

2.5.1 Fibre preform fabrication

This subsection focuses on two kinds of fibre preform manufacturing method: the *Rod-in-tube* method and *Chemical Vapour Deposition* method.

Rod-in-Tube method

Rod-in-tube is the simplest and earliest way to make a conventional step-index optical fibre. The process involves inserting a rod of high-index glass into a tube with lower refractive index. The two are then heated and the tube melts onto the rod, forming a new glass rod, which is called the fibre preform. The schematic diagram of this process is shown in Fig. 2.9.

To reduce the transmission attenuation of the final fibre, the core-cladding interface must be kept extremely clean and smooth during the fabrication process. Mechanical polishing alone cannot remove the tiny cracks and debris, which remain on the rod surface and cause scattering of guided light in the final fibre.

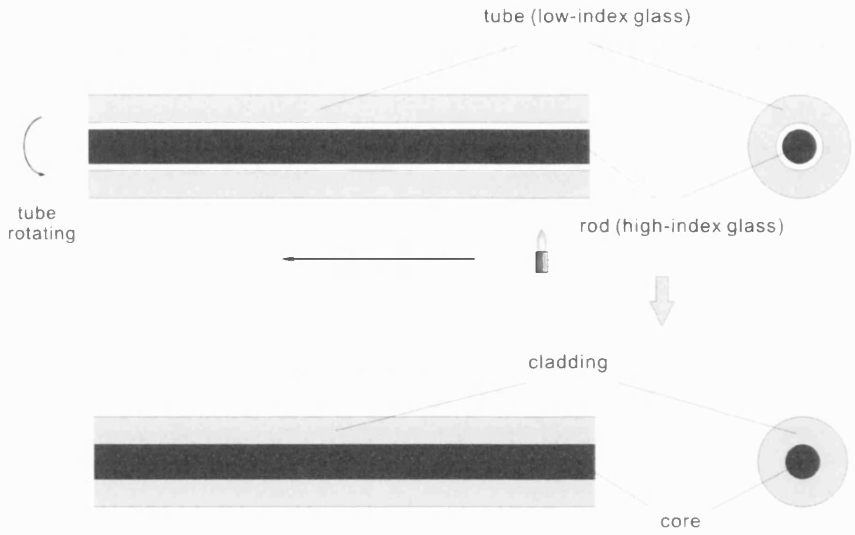

Figure 2.9: Schematic of Rod-in-tube method to fabricate the step-index optical fibre preform.

Instead, fire polishing is used to remove the metal contaminations by oxygenation and clean the rod surface before inserting it into the tube. The inner surface of the cladding tube can be chemically polished to obtain a smooth surface without contaminations.

Fibres produced by this method usually have relatively high attenuation and are used for short-distance image transmission or illumination. At present, this method is preferable for soft glass optical fibres, since the other manufacturing method - chemical-vapour deposition has only been developed to fabricate low-loss commercial silica glass optical fibres.

Chemical-vapour deposition method

The chemical-vapour deposition method includes *Modified Chemical Vapour Deposition* (*MCVD*), *Outside Vapour Deposition* (*OVD*), *Vapour Axial Deposition* (*VAD*), and *Plasma Activated Chemical Vapour Deposition* (*PCVD*).

Key features of these techniques [32] are: 1) that the desired glass constituents are available in the form of volatile gaseous compounds of high purity, 2) that these compounds can be mixed almost ideally in the gas phase, and 3) that reactions, deposition, and purification occur directly in the gas phase at the

gas/solid interface or on soot particles smaller than 10^3 Å. The fluffy fused-silica soot is commonly formed by reacting $SiCl_4$ (and $GeCl_4$ for the doped core) with oxygen to generate SiO_2 (and GeO_2 for the doped core) during the thermally activated (MCVD, OVD, VAD) or plasma activated (PCVD) processes. The crucial variations of these different methods are in the way the soot is deposited and melted to form the final preform.

As an example, the MCVD method [33, 34], is described here. It can be explained by means of Fig. 2.10, which shows a sketch of a MCVD apparatus for optical fibre preform preparation. The substrate for MCVD deposition is a silica tube, which is located between a vapour/gas pump and a exhaust pumping system. The chemicals react to deposit a fine glass soot layer onto the inner wall of a silica tube, while the waste gas is pumped out to an exhaust. The main chemical reactions occurring in the silica tube are listed as

$$SiCl_4 + O_2 \overset{1800°C}{\Longrightarrow} SiO_2 + 2Cl_2 \tag{2.26}$$

$$GeCl_4 + O_2 \overset{1800°C}{\Longrightarrow} GeO_2 + 2Cl_2 \tag{2.27}$$

The typical temperature of a burner torch is high enough (1800 $°C$) to fuse these deposited materials to transparent glass film, but not so high to cause distortions of the substrate tube. The burner torch is moved back and forth to spread soot uniformly along the tube length, building up the preform layer by layer. When a sufficient cladding thickness is obtained, the core is formed by adding index-raising dopants, such as $GeCl_4$ and $POCl_3$. By changing the flow rates of the dopant vapours layer by layer, a core with different index profiles can be fabricated, such as the graded-index core and the triangle-index core. When all the core materials have been deposited, the torch temperature is raised to collapse the tube into a solid rod, forming the final preform.

The MCVD process is also called the inner-vapour-deposition method, since the core and cladding materials are deposited inside a silica tube. By contrast, for OVD and VAD processes, the soot is deposited on the outside of a rotating mandrel. Different from the above three methods, PCVD uses a nonisothermal low-pressure plasma to stimulate gas-phase reactions for the deposition of doped and undoped silica. The working temperature can be about 600-700 $°C$ lower that that for other three thermal activated methods.

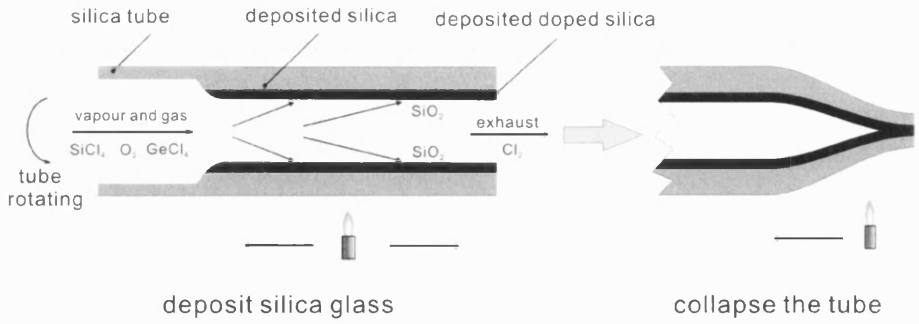

Figure 2.10: Schematic of the modified chemical vapour deposition (MCVD) procedure to fabricate a conventional optical fibre prefrom

After the preform is fabricated, a fibre drawing tower is used to draw it to the final fibre with desired diameter.

2.5.2 Fibre drawing process

A schematic diagram of the fibre drawing process is presented in Fig. 2.11. Fibres can be drawn from a prepared preform by vertically feeding the preform end into the hot zone of a furnace while pulling the softened glass at a higher rate. The temperature of the furnace typically ranges from 1800 °C to 2100 °C. The structure of the preform is closely maintained in the final fibre. The target of this step is just to reduce the transverse scale of the structure while greatly increasing its length. The feed speed is typically a few mm/min, while the drawing speed might range from a few m/min to a few km/min. The ratio of these two speeds determines the final fibre diameter. A laser monitor is used to measure the fibre diameter continuously and control the pulling speed via a feedback system. The fibre diameter can be maintained constant with the fluctuation smaller than 0.1% by this technique. A polymer coating is applied to the fibre just after the diameter monitor to improve the durability and preserve the transmission properties of the fibre. The drawing tension of the fibre is also monitored before it is finally wound around a drum. It may take several hours to draw from several km to a few hundred km length fibre from a single preform. The most common diameter of the commercial conventional optical fibre is 125 μm, 250 μm after polymer coating.

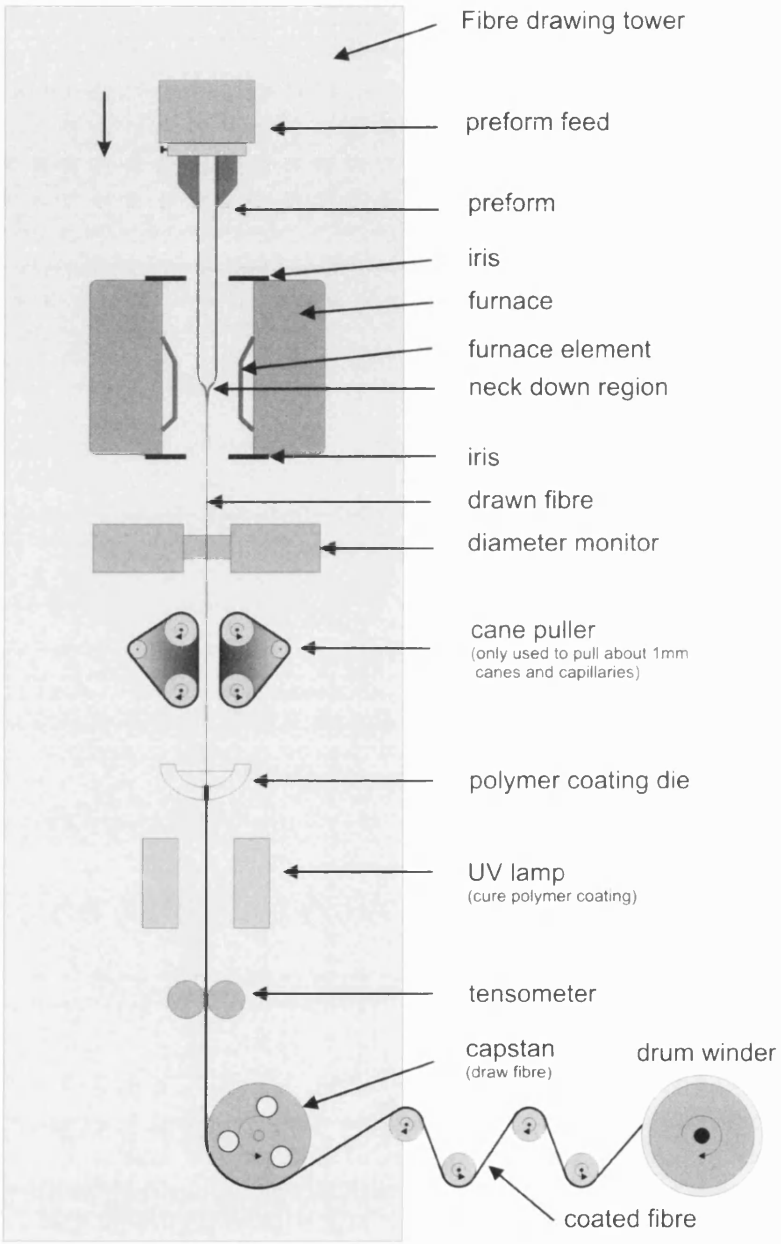

Figure 2.11: Apparatus used for fibre drawing

Chapter 3

Photonic crystal fibres

3.1 Introduction

Chapter 2 described the many advantages of conventional optical fibre, which has become the pre-eminent medium of communicating information in the 20th century. However, the adjustable parameters for designing a conventional single-mode fibre are localised to the core diameter and the index difference, limiting its application ranges. In fact, for different applications optical fibres represent a careful trade-off between their optical properties, such as optical attenuation, optical nonlinearity, group velocity dispersion and polarisation effects. The basic physical concept of optical fibres remained unchanged until the 1990s when a new family of optical fibres demonstrated an almost endless variety of new fibre structures [35, 36, 37, 38, 39]. This new class of fibres can be referred to by the general name *Photonic Crystal Fibres* (*PCFs*) [2, 3]. Compared with conventional fibres, PCFs provide more degrees of freedom to design and fabricate fibres with novel optical properties, broadening the range of possible application areas.

Referring to Fig. 3.1, the cladding of a PCF has a periodic two-dimensional modulation of refractive index on the scale of optical wavelength, corresponding to all the periodic inclusions (refractive index: n_{inc}) embedded in the matrix material (refractive index: n_{mat}). The core is composed of the same material as the matrix glass (refractive index: $n_c = n_{mat}$), and can be regarded as a defect in the periodic structure of the cladding, which comprises one or more missing unit

cells. This kind of refractive index distribution extends along the entire length of the fibre. If a high index core is surrounded by periodic low index inclusions (for example, air holes) in the cladding, light can be guided in the core by a form of total internal reflection (TIR). Such fibres are referred to as *Index Guiding PCFs*. (Unless otherwise stated, all index-guiding PCF in this thesis are based on air holes as the low index cladding inclusions.) By contrast, if the refractive index of the core (matrix) material is lower than that of the inclusions in the cladding, guided modes still exist at certain frequencies, corresponding to the photonic bandgaps formed in the cladding. These kinds of fibres are referred to as *Photonic Bandgap Fibres* (*PBGFs*) [39, 40]. Refractive index profiles of a PBGF and an index-guiding PCF are shown in Fig. 3.1. Note that if the hollow-core PBGF has the structure in Fig. 3.1 with air matrix, it would not be self-supporting, so fine strands of glass are used to link all the inclusions, forming the actual fibre.

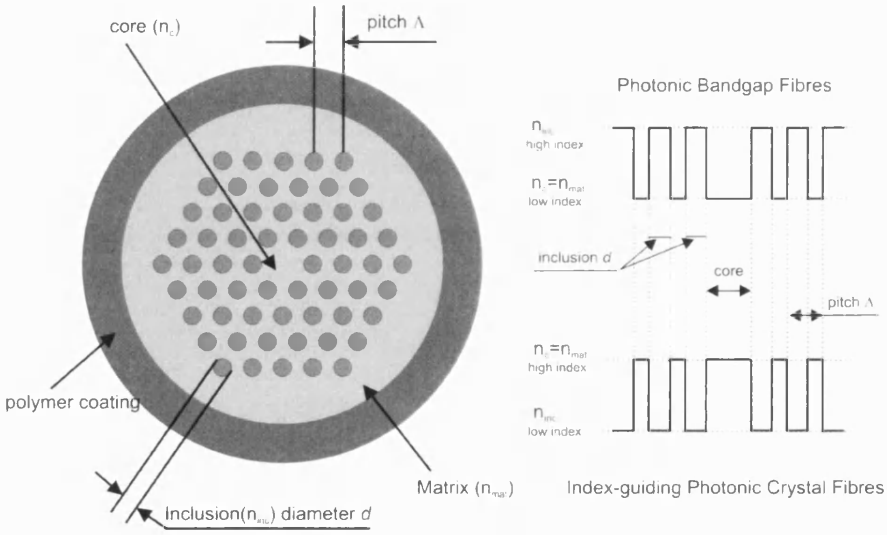

Figure 3.1: The basic structure of PCFs. The refractive index profiles for Photonic Bandgap Fibres and index-guiding PCFs are also provided here.

Except for the refractive index contrast and core size, which completely determine the waveguide structure of an conventional step-index fibre, the inclusion diameter d and the index modulation period, pitch Λ, are also crucial for PCFs, affecting their optical properties. The great versatility of the design and fabrication processes enables a multitude of different kinds of fibre structures to be obtained. This chapter describes the different guiding mechanisms of PCFs, their

novel properties, fabrication methods, and developments.

3.2 Guiding mechanism

To form a guided mode in the core, light needs to be introduced into the core with a value of β that is inhibited in the cladding. The sketch of core and cladding modal refractive indices for different kinds of fibres is displayed in Fig. 3.2, corresponding to different guiding mechanisms.

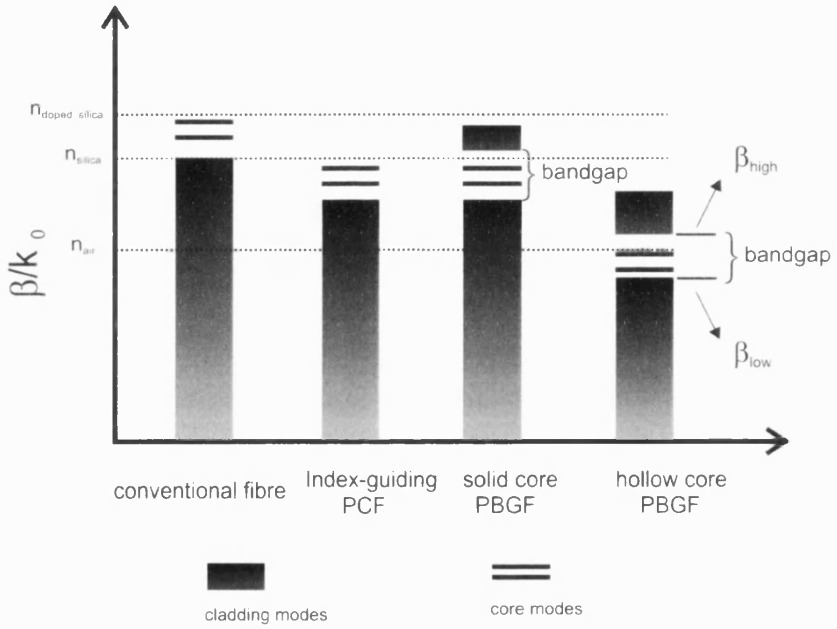

Figure 3.2: Modal refractive indices of different types of fibres. The material for these fibres are based on fused silica glass

3.2.1 Index-guiding PCFs (TIR)

In a conventional fibre, the cladding can be considered to support a continuum of modes with the maximum β-value, equal to $n_{clad}k_0$. Therefore any allowed core modes with the effective index $n_{eff} > n_{clad}$ can be confined to the core region without coupling to the cladding modes (referred to Fig. 3.2). This kind

of guiding mechanism is referred to as total internal reflection (TIR) (referring to Section 2.2), which is realized by using a material for the core with higher refractive index than that of the cladding. A solid-core PCF is formed from one kind of glass material with the core surrounded by glass-air photonic crystal cladding. In such a fibre, the effective refractive index of the cladding is decreased to realize the β-value mismatch between core modes and cladding modes. Such fibres also guide light through a form of total internal reflection (TIR) (referring to Fig. 3.2).

3.2.2 Photonic bandgap fibres (ARROW)

Light of certain frequencies can be guided in the low index defect (core) of a photonic bandgap fibre by bandgap guidance, referring to Fig. 3.2. This guiding mechanism can be understood by the model of *Anti-Resonant Reflecting Optical Waveguide* (*ARROW*) [41, 42, 43, 44]. The principle of the ARROW waveguide can be understood by consideration of Fig. 3.3(A) [42], which shows two different wavelengths propagating in the centre core of a planar waveguide formed by a low-index core surrounded by two high- and low-index cladding layers. The wavelengths corresponding to the minima of the transmission coefficient are referred to as resonant wavelengths, and the wavelengths corresponding to high transmission parts of the spectrum are called antiresonance wavelengths. This terminology is motivated by the fact that high transmission originates from the antiresonant nature of the individual cladding layers with respect to the transverse propagation constant.

Similar principle occurs in a photonic bandgap fibre, where the inclusions are rods with an elevated refractive index (see Fig. 3.1). The bands of photonic states arise from coupled resonances of individual rods. For effective indices above the matrix index these resonances are the waveguide modes of the rods, but these rod modes retain their identity below cutoff as leaky modes. The cladding bands are therefore centred on the dispersion curves of the rod modes, the fibre's high-loss wavelength ranges coinciding roughly with the rod modes' cutoffs. Between these cutoffs the cladding rods are anti-resonant, expelling light and confining it to the core with low loss. The transmission properties of such a fibre can be described as a series of high-loss and low-loss transmission windows, exhibiting an approximately periodic spectral response in frequency. This transmission property makes

a bandgap fibre a good in-line fibre filter. An application example in a Nd laser system will be introduced in Chapter 5.

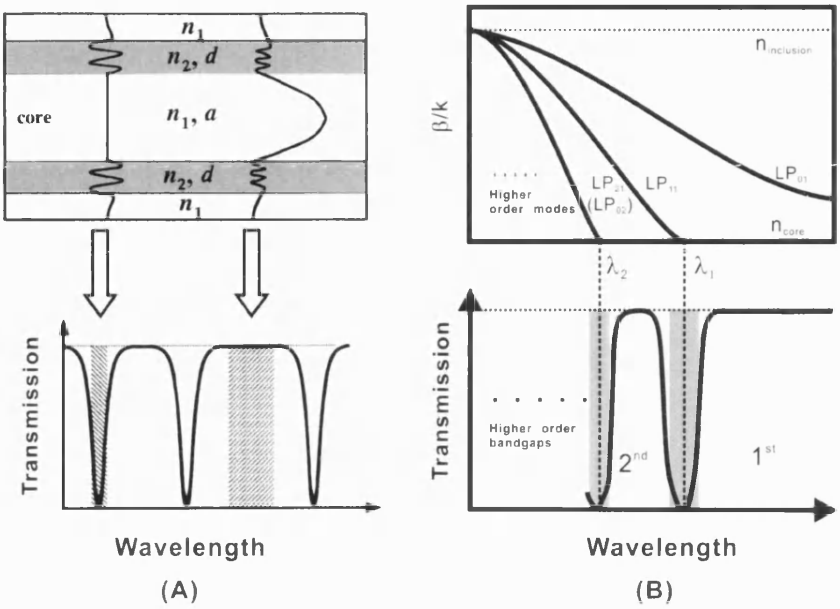

Figure 3.3: (A). Schematic of (top) the ARROW structure and (bottom) its transmission spectrum; (B). Schematic of (top) dispersion relations of the first three low-order modes of the high index cladding rods (LP_{01}, LP_{11} and LP_{02}) and (bottom) the corresponding transmission spectrum of the PBGF.

To understand the ARROW model more clearly, the first two low-order bandgaps of a PBGF are considered in Fig. 3.3(B). The effective modal indices (the first three guided modes) of a individual high index rod in the cladding as a function of wavelength is presented in the top plot in Fig. 3.3(B). The fundamental mode, LP_{01}, has no cutoff, while the cutoff wavelength for LP_{11} and LP_{02} (LP_{21}) modes are marked with λ_1 and λ_2, respectively. LP_{02} and LP_{21} have almost the same cutoff wavelength (refer to Fig. 2.2). These cutoff wavelength regions are corresponding to the high loss transmission regions shown in the bottom plot in Fig. 3.3(B). The first and second bandgaps are also provided in the bottom plot, which are dominated by the dispersion properties of the first three guided modes (LP_{01}, LP_{11} and LP_{02}/LP_{21}). Fig. 3.3(B) is very helpful when we design and fabricate an all-solid bandgap fibre with the desired bandgaps at certain wavelengths, as we will see in Chapter 5.

3.3 Characterisations & applications

The properties of conventional optical fibres have been described in Section 2.3. This section highlights some of the novel properties of PCFs, not possessed by conventional fibres, and one of their applications.

3.3.1 N-number of guided modes

In standard step-index fibres, normalized frequency (V parameter), defined by Eq.(2.2), is usually used to decide the 'mode capacity'. The cutoff properties of second order mode in an index-guiding PCF can also be qualitatively understood within this framework. The V parameter of a PCF can be expressed in a similar way to that of a step-index fibre [37]:

$$V_{eff} = \frac{2\pi\Lambda}{\lambda}\sqrt{n_{core}^2 - n_{eff}^2} \tag{3.1}$$

where the effective index of the cladding n_{eff}, the maximum modal index of the cladding, is used instead of n_{clad} and the pitch Λ substitutes the radius of the core. V_c, the V-value at which the second mode is cutoff in a PCF, can be approximately taken to be 4.1 [45], different from that of the conventional fibre.

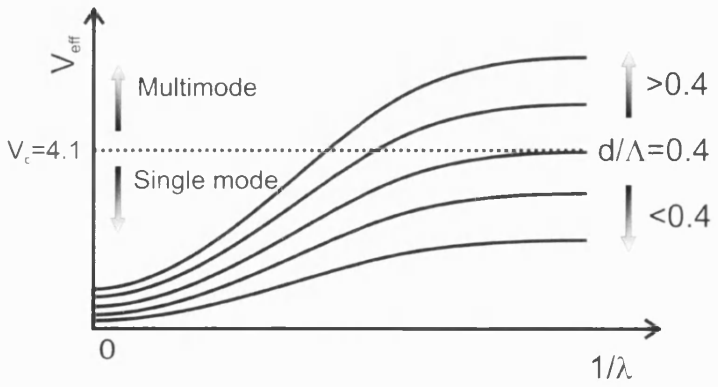

Figure 3.4: Schematic of V-value variation as a function of wavelengths for index-guiding PCFs with different d/Λ. The dashed line corresponding to V-value (V_c) for the second modal cutoff.

Fig. 3.4 schematically presents the V-value variation as a function of wavelength for different d/Λ in index-guiding PCFs. Any fibre working within the regime of

$V_c < 4.1$ can only guide the fundamental fibre mode with the higher-order modal cutoffs. Otherwise, it becomes a multimode fibre, where at least the second order mode can be guided. Note that an index-guiding PCF with the $d/\Lambda < 0.4$ can only work in the single-mode regime for all wavelengths. This kind of index-guiding PCF is called as *Endlessly Single Mode PCF*, quite useful in many application areas, such as supercontinuum generation and optical measurements.

Fundamental and higher-order modes have been observed in hollow-core [39, 46] and solid-core PBGFs [47]. In a photonic bandgap fibre, the number of spatial modes present in the core can be approximately estimated by [39]:

$$N_{PBG} = \frac{(\beta_{high}^2 - \beta_{low}^2) r_{core}^2}{4}$$
$$or = \frac{(k_0^2 n_{core}^2 - \beta_{low}^2) r_{core}^2}{4} \tag{3.2}$$

where r_{core} is the core radius of the fibre and β_{high} and β_{low} are the upper and lower edges of the photonic bandgap at fixed optical wavelength (refer to Fig. 3.2). The second expression applies if the upper bandgap edge extends beyond the maximum core wave vector, that is, if $k_0^2 n_{core}^2 < \beta_{high}$. Certainly there are two polarisation states for each spatial mode. We can see that the bandgap depth (the value of $\beta_{high} - \beta_{low}$) and core radius can decide the number of guided modes in a PBGF. The high-order modes are more possible to guide in a PBGF with larger bandgap depth and more missing unit cells at the core.

3.3.2 Control of dispersion

GVD in index-guiding PCF

For pure silica material, the zero dispersion wavelength (ZDW) is located at the wavelength of 1.27 μm. Due to the low index contrast of a conventional single-mode fibre, the waveguide dispersion normally does not play a major role in determining the total dispersion. Moreover, its waveguide dispersion D-value is usually negative in the visible and near infrared region [6], so that the ZDW is always shifted to the long wavelength side. It is impossible to obtain a conventional single mode fibre with zero dispersion wavelength shorter than 1.27 μm. However, this can be realized in the index-guiding PCF. This is useful for the soliton

research and white light supercontinuum generation which use pump sources in the wavelength region of below 1.3 μm.

Control over the waveguide dispersion in a PCF is greater than for a conventional fibre due to the abundant variation of the structure and the large core/cladding refractive index contrast achievable. Its waveguide dispersion can be positive, so that the overall fibre dispersion can be made anomalous at wavelengths where both GVD of pure silica and the conventional single mode fibre is normal. Many types of index-guiding PCFs with quite different dispersion properties can be designed and fabricated, just by adjusting the d/Λ ratio and core size. Here two extreme cases are introduced.

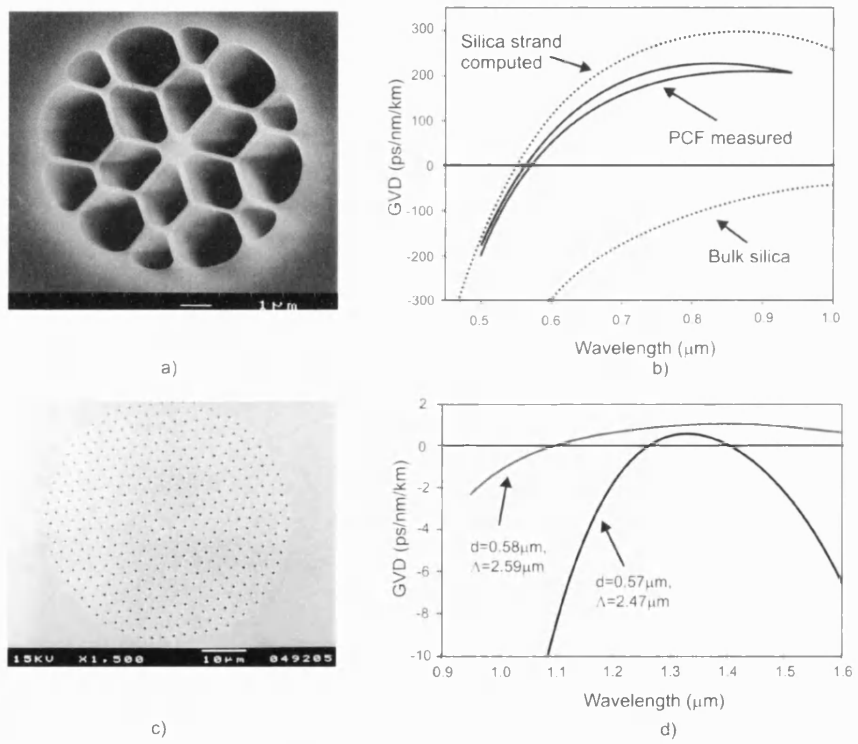

Figure 3.5: (a) Scanning electron micrograph of a photonic crystal fibre with very large air holes [48]. (b) Group velocity dispersion curves of the fibre shown in (a) (solid line), silica strand (1 μm diameter, dotted line) and bulk silica (dotted line). (c) Ultra-flattened dispersion photonic crystal fibre with small holes [49, 50]. The corresponding measured dispersion curves for the fibres with different d and d/Λ are provided in (d).

If the d/Λ approaches 1, the index-guiding PCF can be thought of as a plain silica

strand surrounded by air. A scanning electron micrograph of such an actual PCF [48] with large d/Λ is provided in Fig. 3.5(a). The diameter of the core is roughly 1 μm, and the silica bridges which support the core have thickness of about 120 nm. The dispersion curves for a silica strand and this large d/Λ ratio fibre (both with core diameters of 1 μm) are shown in Fig. 3.5(b). We can see that the zero dispersion wavelengths are pushed quite deeply to the blue, reaching 550 nm. It can be adjusted by changing the d/Λ and the core diameter. Chapter 7 will introduce an index-guiding tellurite glass PCF, where its core size is decreased to about 2.1 μm to shift the zero-dispersion wavelength from beyond 1.7 μm to about 1.4 μm.

When the d/Λ is small, the effective cladding index is closer to silica than air, and the zero dispersion wavelength of such a PCF can be around that of the silica material. In this case, the dispersion slope was reduced by finely tuning Λ and d/Λ ratio. A practical index-guiding PCF with small d/Λ is presented in Fig. 3.5(c) [49, 50]. The ultra-flattened and small dispersion curves are also shown in Fig. 3.5(d).

GVD in PBGF

The waveguide dispersion properties of PBGFs in transmission bandgaps are completely different from the conventional fibres and index-guiding PCFs. For hollow-core PBGFs where the core material is air, the material dispersion contribution for the total dispersion of the fibre is small, the main dispersion component is from waveguide dispersion.

Fig. 3.6 (a) shows the scanning electron micrograph of one hollow-core PBGF [46]. The corresponding dispersion curve of this fibre with an transmission bandgap centred at 800 nm is presented in Fig. 3.6(b). We can see that its group velocity dispersion crosses zero within the low-loss window, and is anomalous over most of the bandgap located at the long wavelength side. The blue side of the bandgap has a normal dispersion. By shifting the bandgap location, which can be realized by scaling the pitch Λ of the cladding structure, the zero GVD point can be easily adjusted to the desired wavelength. In all-solid PBGF the material dispersion cannot be neglected, as it has more of an effect on the total GVD than that of air in the hollow-core PBGF. The normal material dispersion shifts the zero GVD wavelength to the red side and decrease the D-value of the

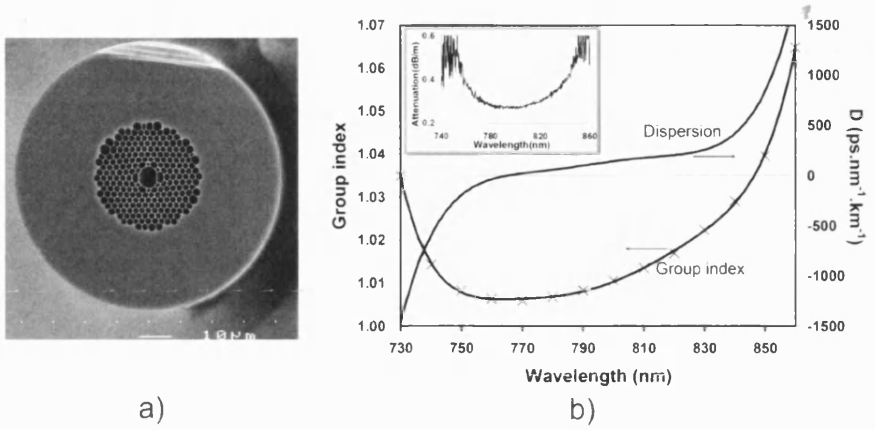

Figure 3.6: (a) Scanning electron micrograph of a hollow-core PBGF [46]. (b)Measured group index and GVD in the transmission bandgap centred at 800nm for an air-core PBGF with same structure as the fibre shown in (a). The inset shows the fibre attenuation.

fibre; the anomalous material dispersion can shift the zero GVD wavelength to the blue side and increase the D-value.

3.3.3 Compact, bright and broad continuum source

Controllable zero-dispersion wavelength and endlessly single mode operation of an endlessly single mode PCF have been exploited to dramatic effects in supercontinuum generation. Such a fibre with zero dispersion wavelengths at <1064 nm can be pumped with a passively Q-switched Nd:YAG laser at 1064 nm [31], and generate flat supercontinuum extending from 500 nm to beyond 1750 nm. This fibre has a core diameter of 5 μm, pitch of 2.97 μm and d/Λ of 0.39, displayed in Fig. 3.7. Fig. 3.7 (a) shows the experimental setup and the generated supercontinuum is presented in Fig. 3.7 (b).

Such a compact, bright, broad and flat continuum source has obvious application in spectral testing of fibre components (used extensively as a spectral testing source in our laboratory)and spectral analysis of chemical and biological samples. In fact, this setup of supercontinuum generation has been frequently used as a light source in my experiments during the course of my PhD.

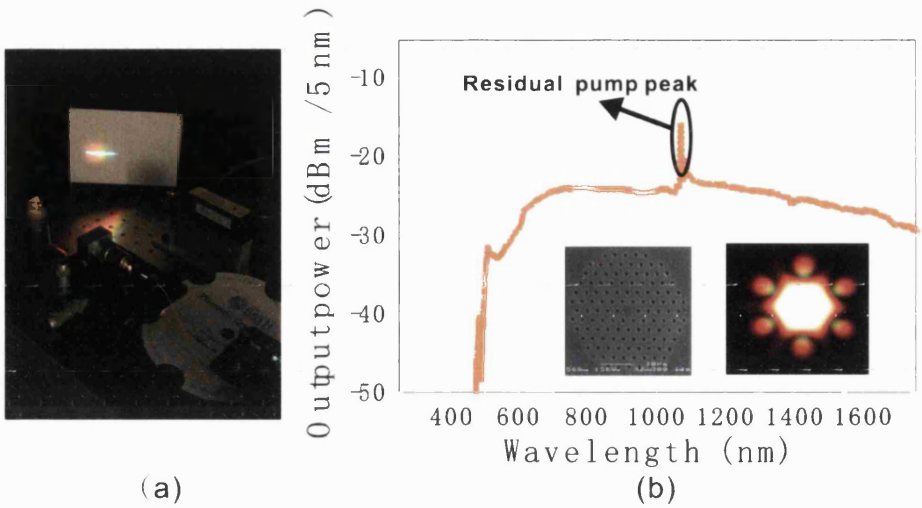

Figure 3.7: A compact, bright and broad continuum source by using the photonic crystal fibre [31]. (a): photograph of experimental setup; (b): broad supercontinuum spectrum generated from a photonic crystal fibre pumped by a passively Q-switched Nd:YAG laser. The scanning electron micrograph of the used PCF and its far field pattern are also displayed in the diagram.

3.4 Fabrication processes of PCFs

A photonic crystal fibre is made by reducing a relatively large, easily produced macro-structure, down to a micro-structure with features comparable in size to the wavelength of light. Several different fabrication methods can be used to produce structured PCF preform, such as '*Stack-and-draw*' technique [36], *Extrusion* [51, 52, 53, 54] and *Ultrasonic Drilling* [55]. Only the first two methods, related to my PhD work, will be introduced in this section.

3.4.1 Stack-and-draw

'Stack-and-draw' technique is the most commonly used technique to manufacture silica PCF preforms, schematically shown in Fig. 3.8. Capillaries and rods are stacked into a hexagonal array, and progressively reduced in diameter until the structure becomes a fibre with the required waveguiding characteristics.

First, a commercially available silica glass tube with 10-20 mm outer diameter

is elongated into around 1-mm-diameter capillaries (step 1 in Fig. 3.8). Hundreds of the capillary silica tubes are then stacked together with appropriately positioned solid glass rod(s), forming a silica-air structure of perhaps 20 mm in outer diameter and 1 meter in length (step 2 in Fig. 3.8). After inserted into a

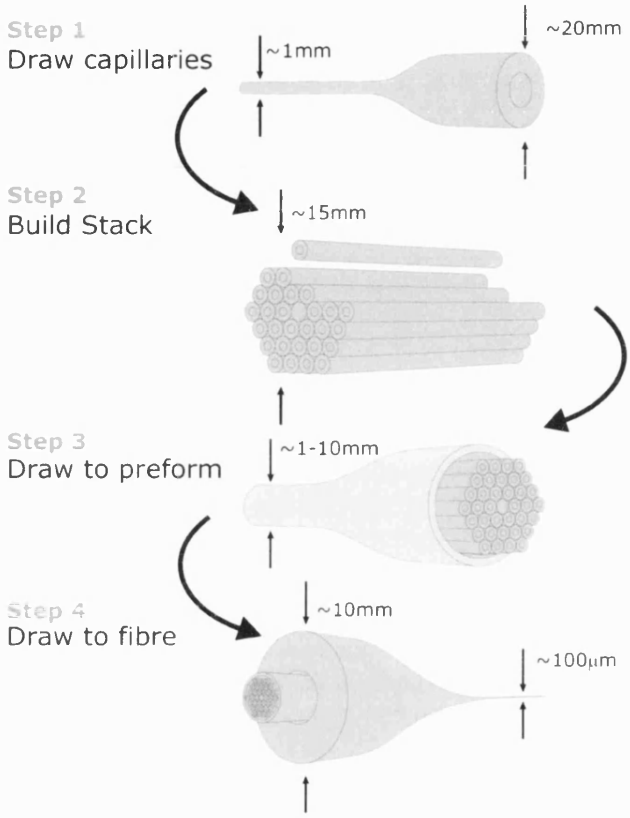

Figure 3.8: Stack-and-draw technique to fabricate PCF.

silica jacketing tube, this stack is drawn to meter-long preforms with a desired diameter, usually several millimeters (step 3 in Fig. 3.8). These are then jacketed by another silica tube and drawn into kilometer-long photonic crystal fibres with a typical diameter range from one hundred to several hundreds microns (step 4 in Fig. 3.8). All these steps can be achieved on a conventional drawing tower.

During the fabrication process, gas (usually nitrogen) pressure can be applied to the preform to keep the holes of all the capillaries open. Meanwhile, vacuum can also be applied in the region between the stack and the tube to help the silica tube to collapse around the structure. The holes between capillaries and rods, called interstitial holes, can also be collapsed by this vacuum. The draw down ratio, drawing temperature and the drawing speed need to be carefully controlled to

obtain the required structure. Even though the 'stack-and-draw' technique seems to be a bit more complicated than the conventional fibre fabrication methods, it is straightforward to make long length of uniform fibres with almost unlimited structures.

3.4.2 Extrusion

Extrusion is a well-known process in the technology of metals, plastics and glasses [56, 57] for the manufacture of rod, tube and other complex profiles. Extrusion

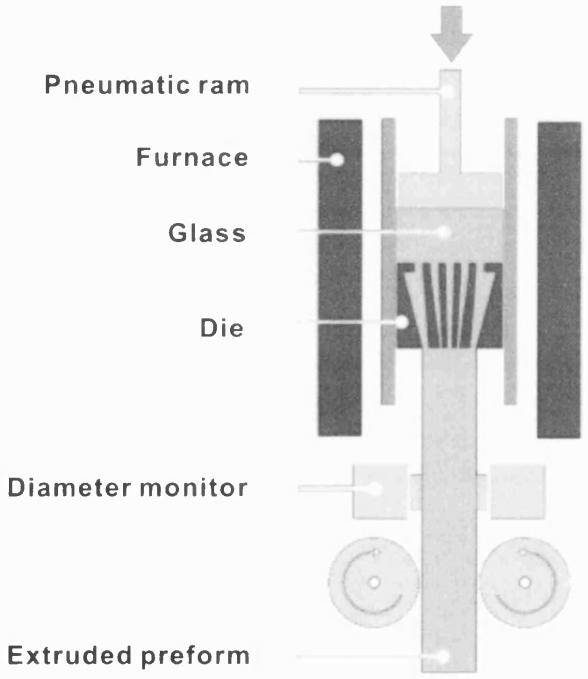

Figure 3.9: Sketch of extrusion process.

mainly enters into consideration for glasses with these properties: (1) Glasses with a steep viscosity-temperature curve, where their narrow temperature range for working is very inconvenient for shaping; (2) Glasses with a strong tendency to devitrify (change from glassy state to minutely crystalline state); (3) High melting temperature glasses (extrusion can work at comparatively lower temperature than glass drawing). Extruded PCFs have been realized at the University of Bath using

SF6 and tellurite glasses, which will be introduced in Section 3.5.

The basic concept of extrusion is as simple as squeezing toothpaste out of a tube, where the pressure applied to the closed end of the tube forces the paste to flow through the open end. The continuous shape, or profile, of the paste as it emerges reflects the shape of the opening or aperture through which it has been forced, and can be as simple or as complex as required. Fig. 3.9 schematically shows the extrusion process. A direct or forward extrusion process (where product and punch move in same direction) is used to force a heated glass billet to flow through a die designed with the desired profile. The shape of extruded preform or tube can be quite similar to that of the extrusion die, by optimizing the pressure and temperature. The low cost, small volume (large quantities of glass tubes necessary for stack-and-draw method are not required), simple operation and the extensive applicability all contribute to the advantages of the extrusion method. For these reasons extrusion dominates the fabrication process for glasses with steep viscosity-temperature behaviour. On the other hand, the metal contaminations from the extrusion die, crystallization and fluctuation in size must be considered, as these can cause high loss in fibre fabricated by this method.

3.5 Developments of PCFs

The historical developments of PCFs are introduced in this section. Index-guiding PCFs and PBGFs are presented separately.

3.5.1 Index-guiding PCFs

The developments of index-guiding PCFs along the time scale are presented in Fig. 3.10 with the cross-section images of some PCFs. Due to the abundant variations of PCF structures, only these elements of their developments which are directly related to the work in this thesis will be described.

Highly birefringent PCFs

The first PCF image presented in Fig. 3.10 is a highly birefringent PCF [58] with elliptical core formed by introducing holes with different sizes near the core in one direction. The high index contrast between the silica core and air cladding makes the form birefringence in this fibre very high, reaching 3.7×10^{-3} at a wavelength of 1.54 μm. This level of birefringence is at least 10 times larger than any shape birefringence obtained in conventional fibres. In Chapter 4, another kind of form birefringence will be introduced in a novel microstructured fibre with lamellar core.

Nonlinear PCFs

Index-guiding PCF with large d/Λ can confine light tightly in the core and, when combined with a small core size, has high nonlinearity. Such a fibre is shown in Fig. 3.5. As part of my PhD work, another kind of glass material, tellurite glass, with higher nonlinear coefficient than silica glass was fabricated and used to make highly nonlinear PCF, with nonlinear coefficient γ=596 $km^{-1}W^{-1}$ at 1550 nm (refer to Chapter 7).

Soft glass PCFs

Fig. 3.10(4) shows scanning electron micrographs of extruded silicate (SF6 glass) and tellurite glass PCF [52, 62]. By using the extrusion technique, structured PCFs can easily be fabricated from soft glasses with steep viscosity-temperature response. A extruded tellurite PCF will be introduced in Chapter 7.

In contrast to all the other index-guiding PCFs, which are composed of only one kind of glass material and air, an all-solid PCF using two types of silicate glass was demonstrated in 2003 [63]. To form a fibre, the two kinds of glasses (one with high index, H1, and the other with low index, B1) had to have good compatibility in terms of mechanical, rheological, thermodynamic and chemical properties. The final fibre is shown in Fig. 3.10(5). Our highly birefringent fibre with lamellar core was also composed of two different kinds of glass materials, which will be introduced in Chapter 4.

Using extrusion it is hard to obtain a microstructured fibre with more than several periods in the cladding structure. Increasing the number of periods can contribute to the decrease of the fibre's confinement loss. After solving the drilling and

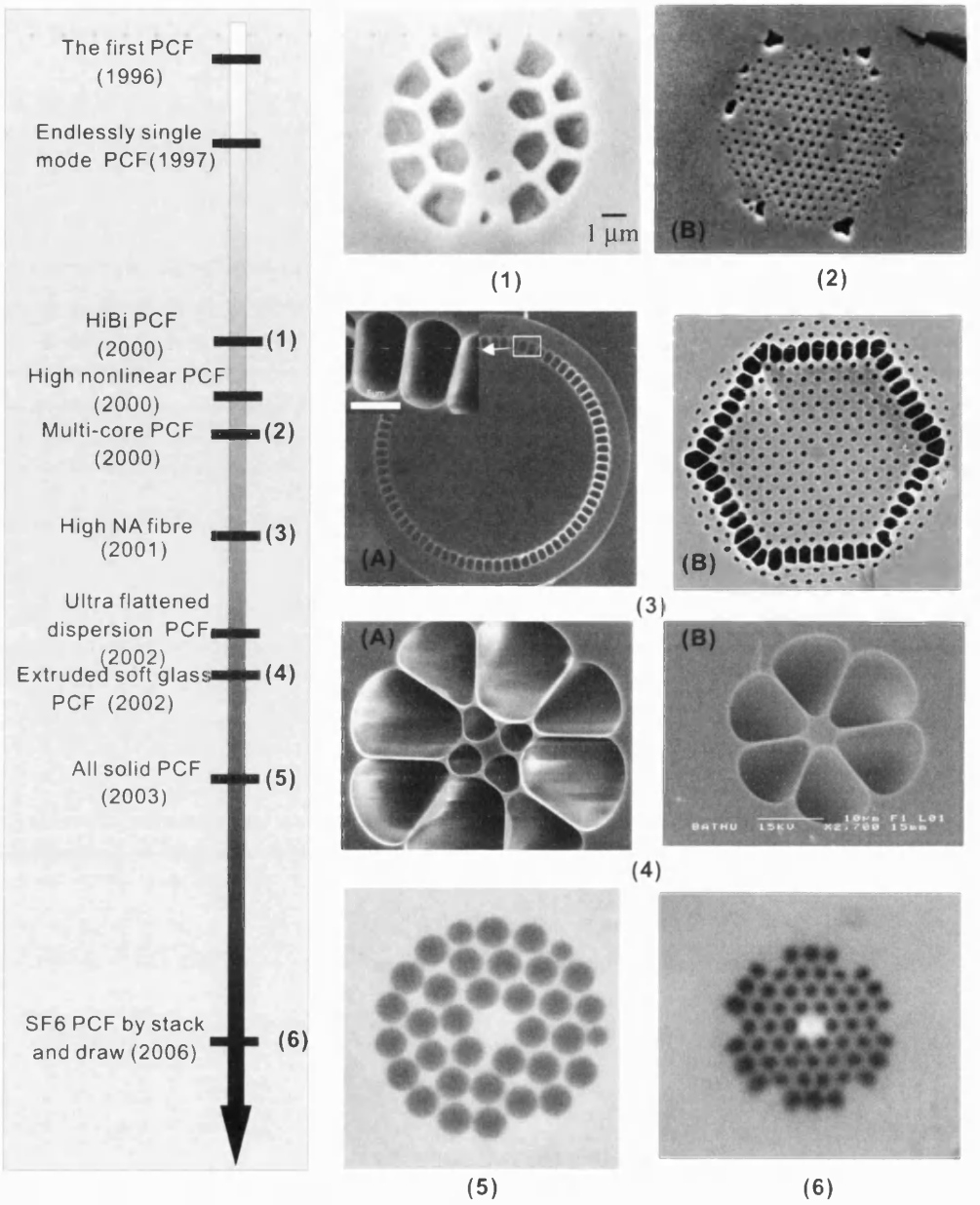

Figure 3.10: Index-guiding PCF progress along the time scale. (1) Scanning electron micrograph of the first highly birefringent PCF having a line of smaller holes across the cladding [58]. (2) Scanning electron micrograph of a four-core PCF [59]. (3) Scanning electron micrographs of double-cladding fibres: (A) inner cladding is a conventional fibre structure [60]; (B) inner cladding is a PCF structure [61]. (4) Scanning electron micrographs of extruded soft glass PCFs: (A) SF6 glass [52]; (B)tellurite glass (see Chapter 7). (5) Back-scattered electron image of an all-solid PCF with dark region as low index glass [63]. (6) Optical micrograph of a PCF fabricated using commercial SF6 glass by stack and draw method.

polishing difficulties of soft glass billets (this will be introduced in Section 4.6), a silicate glass (commercial SF6 glass) PCF by using stack-and-draw method was demonstrated in University of Bath, shown in Fig. 3.10(6).

3.5.2 Photonic bandgap fibre

Hollow-core PBGF

The bandgap guiding effect with silica-air structures, predicted in 1995, was first reported by J.C. Knight et. al. in 1998 [64]. The fibre had a honeycomb structure, shown in Fig. 3.11(1)-(A), and its low-index defect ensured that there was no possibility of waveguiding by total internal reflection. The coloured guided mode is shown in Fig. 3.11(1)-(B)(C). After the first demonstration of the PBGF, members of the University of Bath developed the fabrication technology to a level where a structure with high air-filling fraction, critical for achieving a photonic bandgap for hollow-core fibre, became possible. The first hollow-core PBGF was demonstrated in 1999 [39], consisting of a triangular array of air holes in silica with interstitial holes. The hollow core is formed by the removal of seven capillaries. Its scanning electron and optical micrograph are shown in Fig. 3.11(2). The coloured modes demonstrated the bandgap properties: guidance only exists in the low-loss transmission window generated by the cladding bandgap. In 2003, low loss (1.72 dB/km at 1565 nm) hollow core PCF was reported [65], shown in Fig. 3.11(3). This loss is only one order of magnitude higher than that of conventional state-of-the-art silica fibre (0.15 dB/km). The hollow-core nature enables the lower-loss transmission possible, and a hollow-core PBGF are also quite useful for high power laser delivery, since almost all of the laser beam power is located in the hollow region of its core giving high damage threshold.

All-solid PBGF

The all-solid PBGF was first demonstrated by using two kinds of thermally matched soft glasses in 2004 [47], as illustrated in Fig. 3.11(4). The structure was a two dimensional triangular array of high-index rods (SF6 glass with refractive index of 1.79, the bright region in the scanning electron micrograph) embedded in a low-index background (LLF1 glass with refractive index of 1.54, the dark region). The core area, which would have contained 7 unit cells, was replaced

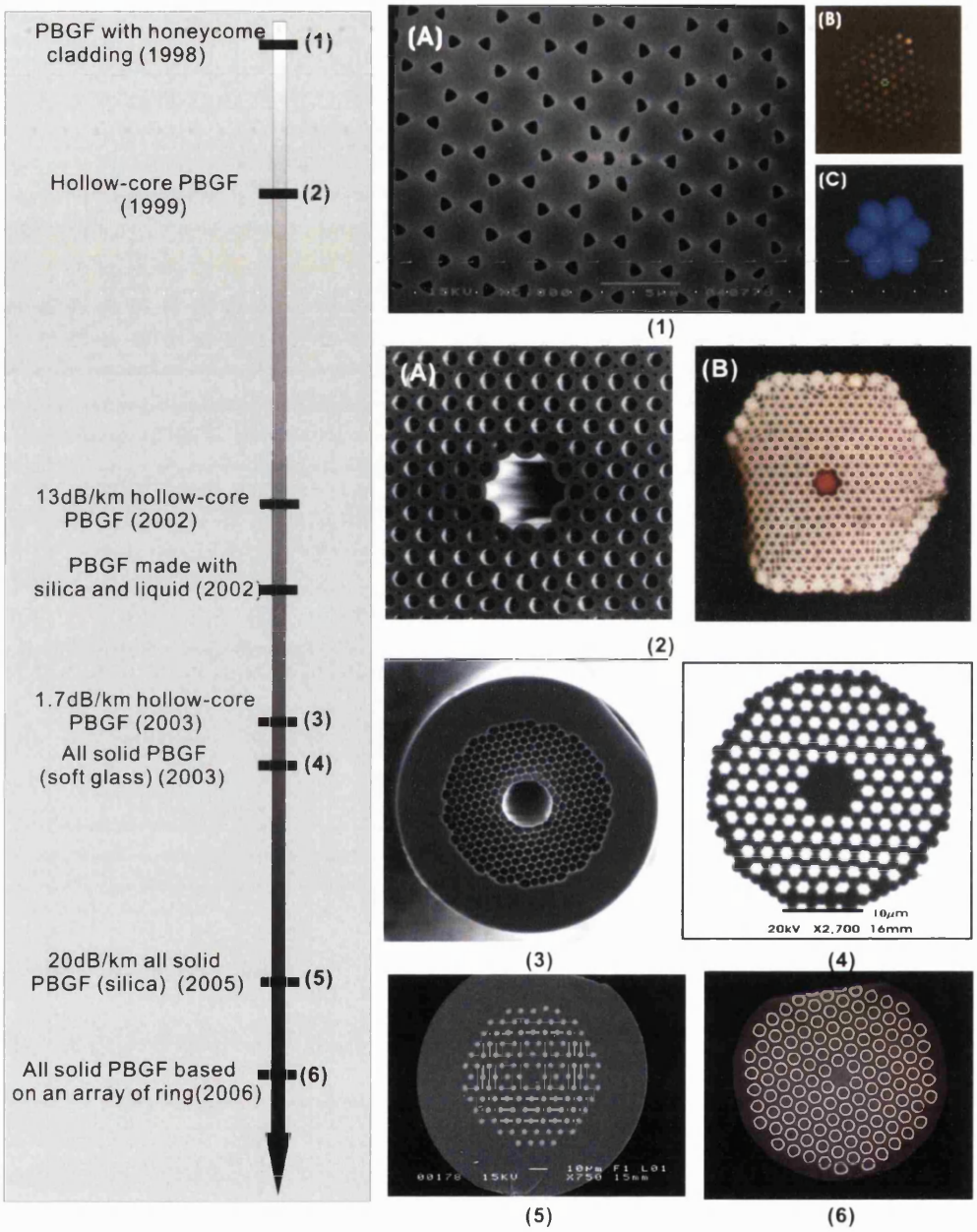

Figure 3.11: PBGF progresses along the time scale. (1)(A) Scanning electron micrograph of an honeycomb PBGF (the first PBGF); (B) Optical micrograph; (C) Far-field pattern [64]. (2) The first reported hollow-core PBGF [39]: (A) a scanning electron micrograph; (B) the nearfield pattern of the fibre. (3) A scanning electron micrograph of a 19-cell hollow-core PBGF [65]. (4) Scanning electron micrograph of the first all-solid bandgap fibre composed of two kinds of soft glasses [47]. (5) Scanning electron micrograph of an all-solid silica PBGF (see Chapter 5); (6) Optical micrograph of an all-solid PBGF based on an array of rings [69].

with low index glass. This structure represented a perfect bandgap fibre without fine strands connecting the high-index inclusions like hollow-core PBGF, and so exhibited no surface modes and guides over the full width of multiple bandgaps.

After the demonstration of the first all-solid PBGF using two kinds of high-index-contrast soft glasses, the all-solid PBGF was also realized by using low-index-contrast silica glasses. In the first silica all-solid PBGF reported in 2005 [66], the refractive index of the high index Ge doped part is only 1% higher than pure silica. This early all-solid PBGF was constructed by inserting multimode and single-mode fibres into a PCF matrix and then drawing the preform to fibre. After that, the traditional stack-and-draw method was used to produce the low-loss all-solid silica PBGF reported in 2005 [67]. This fibre was reported to have a loss as low as ~6 dB/km at 1560 nm [68]. The canes, which were stacked to form the whole structure, were drawn from a large-area Ge-doped conventional preform. An example of this type of fibre is shown in Fig. 3.11(5). Compared with a hollow-core PBGF, which suffers from tricky fabrication, surface modes and high splicing loss with conventional fibre, an all-solid PBGF has none of these disadvantages. Moreover, an all-solid PBGF makes it possible to construct a rare-earth doped fibre amplifier/laser, or work as an in-line fibre filter, which can be mode-matched to the conventional fibre. Related work carried out during the course of this thesis will be presented in Chapter 5.

Due to its abundant photonic bandgap structures, the low-index-contrast all-solid PBGF is a good candidate to study the physical nature of photonic bandgaps, especially bend losses. Related work done during this thesis will be introduced in Chapter 6. These results suggested that replacing the high index cladding rods with thin annular rings with low-index centre was a possible way to reduce the bend sensitivity in a PBGF. This idea was demonstrated in an improved all-solid PBGF based on an array of rings in 2006 [69], shown in Fig. 3.11(6). Comparing the performance of the ring fibre with that of a similar fibre made using doped rods, it can be found that the use of rings to form the cladding re-orders the cladding modes so as to broaden the photonic band gaps and reduce bend sensitivity. During my thesis period I fabricated and characterised another kind of all-solid PBGF based on oriented rectangular high index rods. This will be introduced in Chapter 6.

Chapter 4

Highly birefringent lamellar core fibre

4.1 Introduction

Polarisation-maintaining (PM) fibres are usually created by intentionally introducing a high birefringence to the guided modes. Two methods have been used to achieve the required birefringence. The shape of the refractive index profile defining the waveguide core has been made non-circular (shape or form birefringence) or the material forming the fibre itself has been made birefringent by introducing stresses (stress birefringence). Elliptical core fibres and PANDA/bow-tie fibres are typical examples of these two kinds of birefringence.

In this chapter, a novel optical fibre with a lamellar structured core is reported to have very high birefringence, reaching 6.4×10^{-3} at the wavelength of 543 nm, the highest ever reported birefringence value in a single mode optical fibre. This high birefringence is introduced by artificially structuring the core on a sub-wavelength scale. The detailed fabrication processes, properties of guided modes and birefringence modelling results of this novel PM fibre are described in this chapter.

4.2 Origin of birefringence in lamellar structure media

It is well known that the birefringent properties of crystals can be explained in terms of the anisotropic electrical properties of the molecules from which the crystals are formed. Birefringence may, however, arise from anisotropy on a scale much larger than molecular, namely when there is an ordered arrangement of similar particles of an optically isotropic material on a size scale large when compared with the dimensions of molecules, but small compared to the wavelength of light. This is one kind of form birefringence [70].

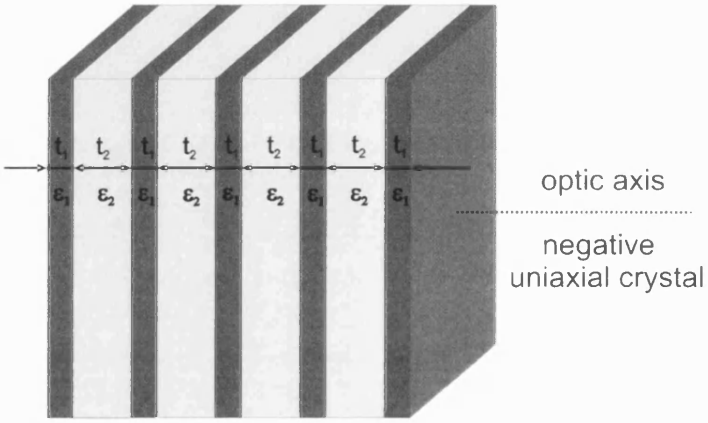

Figure 4.1: Structured medium consists of a regular assembly of parallel plates.

This kind of form birefringence can be explained by considering a medium which is a regular assembly of two kinds of thin parallel dielectric plates ϵ_1 and ϵ_2 with the thickness of t_1 and t_2 respectively, shown in Fig. 4.1. Note that the linear dimension of the faces of the plates are assumed to be infinite, but the thicknesses t_1 and t_2 are small compared to the wavelength.

Suppose that a plane monochromatic wave, which is incident on this assembly, has its electric vector perpendicular to the plates. According to the boundary condition, the normal component of the electric displacement D must be continuous across the interface of these two dielectric media. The corresponding electric

fields E_1 and E_2 in these two media, have the relation

$$E_1 = \frac{D}{\epsilon_1}, \qquad E_2 = \frac{D}{\epsilon_2} \tag{4.1}$$

so the mean field E averaged over the total volume is

$$E = \frac{t_1 \frac{D}{\epsilon_1} + t_2 \frac{D}{\epsilon_2}}{t_1 + t_2} \tag{4.2}$$

The effective dielectric constant, marked as $\epsilon_\perp$ at this case, is therefore,

$$\epsilon_\perp = \frac{D}{E} = \frac{(t_1 + t_2)\epsilon_1\epsilon_2}{t_1\epsilon_2 + t_2\epsilon_1} = \frac{\epsilon_1\epsilon_2}{f_1\epsilon_2 + f_2\epsilon_1} \tag{4.3}$$

where $f_1 = t_1/(t_1 + t_2)$, $f_2 = t_2/(t_1 + t_2)$. Suppose next that the incident field has its electric vector parallel to the plates. According to boundary condition, the tangential component of the electric vector is continuous across the interface of two media, so that the electric field will have the same value E in these two media. The electric displacements D_1 and D_2 can be written as

$$D_1 = \epsilon_1 E, \qquad D_2 = \epsilon_2 E \tag{4.4}$$

so that the mean electric displacement D is

$$D = \frac{t_1\epsilon_1 E + t_2\epsilon_2 E}{t_1 + t_2} \tag{4.5}$$

Hence the effective dielectric constant is now given by

$$\epsilon_\parallel = \frac{D}{E} = \frac{t_1\epsilon_1 + t_2\epsilon_2}{t_1 + t_2} = f_1\epsilon_1 + f_2\epsilon_2 \tag{4.6}$$

Since the effective dielectric constant is the same for all directions parallel to the plates, but different for directions normal to the plates, this medium behaves as a uniaxial crystal with its optical axis perpendicular to the plane of the plates. The difference of $\epsilon_\parallel$ and $\epsilon_\perp$ can be expressed as

$$\epsilon_\parallel - \epsilon_\perp = n_o^2 - n_e^2 = \frac{f_1 f_2(\epsilon_1 - \epsilon_2)^2}{f_1\epsilon_2 + f_2\epsilon_1} \geq 0 \tag{4.7}$$

where n_o is the refractive index of an ordinary wave, corresponding to the electric vector parallel to the plate, and n_e is the refractive index of an extraordinary wave, corresponding to the electric vector perpendicular to the plate. We also

know that this medium always behaves like a negative uniaxial crystal. Eq.(4.7) also implies that the bigger the refractive index difference of these two media is, the higher birefringence can be obtained for the whole medium.

We have formed such a structure using two commercially available glasses from Schott, chosen because of their thermal compatibility and large index difference, SF6 (refractive index 1.79 at the wavelength of 706 nm) and LLF1 (refractive index 1.54 at the wavelength of 706 nm) [47]. Simply substituting these value into Eq.(4.7), we can obtain the estimated material birefringence, $\Delta n{=}n_o - n_e$, which can reach 0.018.

4.3 Manufacturing processes

4.3.1 Glass properties

In order to identify suitable glasses for this work, we studied the data sheets of many commercially available glasses. The successful candidates required not only a large index contrast to obtain a high birefringence, but also quite similar thermal properties to enable fibre fabrication. The previous work of all-solid PCF based on two types of silicate glass [63] provided us some clues to find the suitable glasses. During the selection of suitable glasses, we first chose a pair of commercially available glass with highest index contrast, then compare their compatibility in terms of mechanical, rheological, thermo-dynamic and chemical properties. The thermal parameters of some of the glass candidates I ever considered are listed in Table 4.1. After a lot of comparisons and eliminations, LLF1 and SF6 glasses from Schott were regarded as the optimal glass materials for the highly birefringent fibre. Their high index contrast of about 0.25 for the whole visible and infrared light region (Table 4.1), is one of the largest values we can find from the commercial silicate glasses, ensuring that our final lamellar core fibre will have very high birefringence. The details about the glass selections based on thermal parameters are discussed as below.

α is the linear thermal expansion coefficient. Matching of expansion coefficients of two materials being drawn together is essential to prevent fracture caused by

Soft Glasses	refractive index @706.5nm	$\alpha_{-30-+70^oC}/\alpha_{+20-+300^oC}$ $(10^{-6}/K)$	T_g (^oC)	$T_{10^{13}}/T_{10^{7.6}}$ (^oC)
LLF1	1.54	8.10/9.20	448	426/628
N-FK5	1.48	9.2/10.0	466	469/672
N-FK9	1.51	9.6/11.0	476	476/640
N-BK7	1.50	7.1/8.3	557	557/719
SF6	1.79	8.10/9.00	423	410/538
SF66	1.89	9.0/11.5	384	385/482
SF67	1.87	6.2/7.4	539	546/663
SF57	1.81	8.3/9.2	414	391/519

Table 4.1: Thermal properties and material indices of commercial glasses SF6 and LLF1 from Schott Ltd.

heating and cooling in the fabrication process which induce stresses. Commonly, a difference in coefficients of less than about $2\times10^{-7}/K$ is optimum for two different glasses. If the difference reaches higher than $5\times10^{-7}/K$, any two different glasses are quite difficult to draw together [71]. Our selected glasses have an excellent match at this point.

Another important issue of drawing two glasses together is whether they can be drawn at the same temperature. To understand this, it is convenient to consider an important thermal parameter of glass, viscosity (η, expressed with the unit of poise P), which determines the melting conditions and the temperatures of working and annealing. Fig. 4.2 presents the variation of glass viscosity with the temperature, where different glass conditions are all marked [71]. The annealing point of a glass is defined as the temperature at which it has a viscosity of 10^{13} P. At the glass transition temperature, the viscosity is about $10^{12.3}$ P. As the temperature increases, viscosity decreases to $10^{7.6}$ P, reaching the softening point, where glasses can deform under their own weight. The working point corresponds to the viscosity of 10^4 P. Though the working temperature is not provided in the normal database of commercial glasses, we can obtain some clues from the annealing temperature (marked as $T_{10^{13}}$), glass transition temperature (marked as T_g) and softening temperature (marked as $T_{10^{7.6}}$), listed in the provided data sheets: a big overlap in the broad temperature range between them implies a similar viscosity curve of the glasses, suggesting possible drawing of different glasses together.

According to Table 4.1, even though there are other possibilities of glass pairs, which have higher index contrast than LLF1 and SF6 glasses, these two kinds of

glass always have better thermal compatibilities. Note that the $T_g/T_{10^{7.6}}/T_{10^{13}}$ of SF6 glass is slightly lower than that of LLF1 glass and SF6 glass has a steeper viscosity-temperature curve than LLF1 glass. All these suggest that during the fibre drawing process SF6 glass is softer (has lower viscosity) and more sensitive to the fluctuation of the furnace temperature than LLF1 glass.

Overall, the excellent matchings of thermal properties and high index contrast between SF6 and LLF1 glass strongly suggest that they are excellent material candidates to realize our highly birefringent lamellar core fibre.

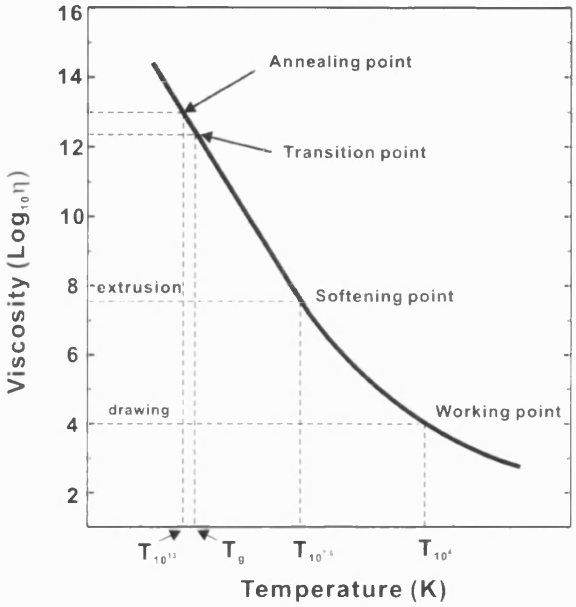

Figure 4.2: Schematic viscosity curve of silicate glass with the function of temperature (after [71]).

4.3.2 Fibre fabrication

Lamellar core material preparation

To make the lamellar core fibre, we first cut 3 mm thick Schott SF6 and LLF1 glass plates to 21 mm × 50 mm rectangular pieces and then polished both sides. 7 plates (SF6: 3 plates, LLF1: 4 plates) were then stacked together and fused by placing them in a furnace at 650 °C for 3 hours. Due to the similar thermal properties of these two glasses, they fused to form a lamellar glass block with

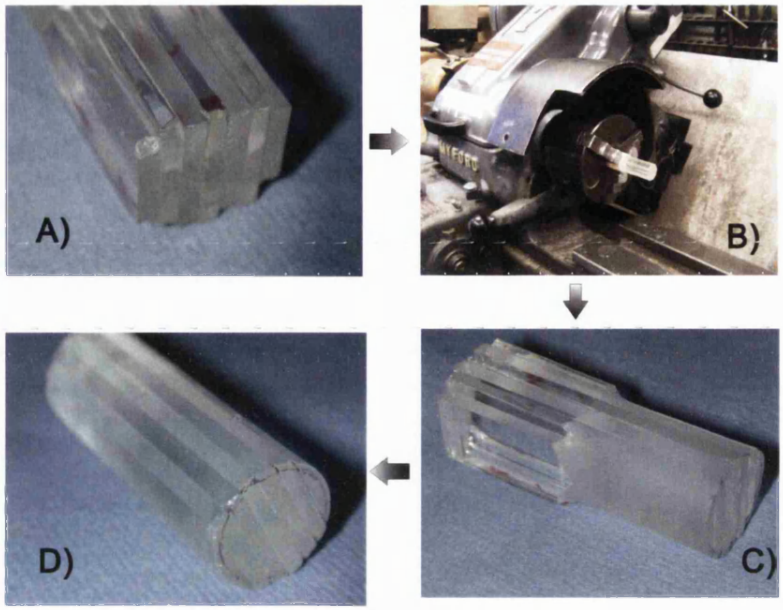

Figure 4.3: (A)Glass block formed by fusing 7 glass plates together using the furnace. (B) The lathe used to grind and polish the glass block to a cylindrical glass rod. (C) The glass block with one end ground. (D) The final glass rod.

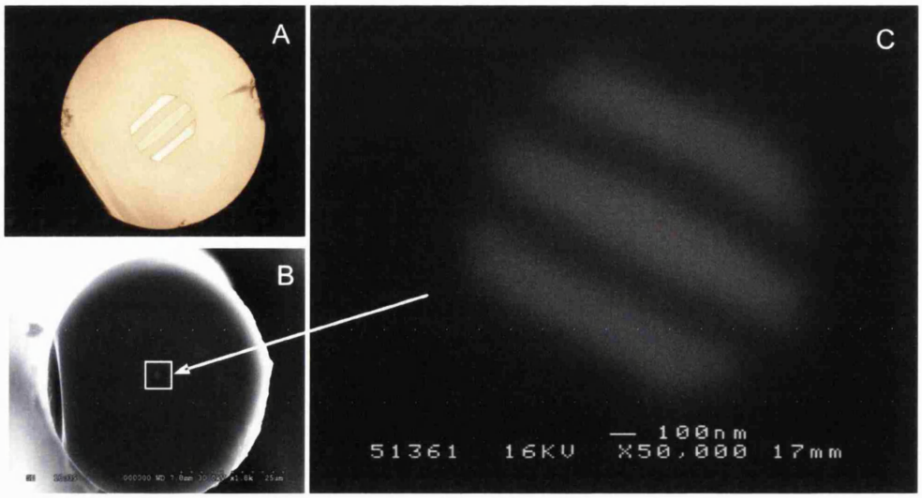

Figure 4.4: (A) Optical image of the preform with one jacketing tube. (B) Scanning electron image of the lamellar core fibre with 1.2 μm core size and 50 μm outer diameter. (C) Backscattered electron image of the core region of the fibre in (B).

the dimension of 21 mm × 21 mm × 50 mm, shown in Fig. 4.3(A). One end of this glass block was then fixed in a lathe (Fig. 4.3(B)), and rotated at a fixed speed. A diamond coated disc was then used to slowly grind the exposed part of this glass block into a cylindrical glass rod (Fig. 4.3(C)). Turning the glass block around and repeating the above step completed the lamellar cylindrical glass rod (Fig. 4.3(D)). The next step was to polish this glass rod. The better the polished surface was, the lower loss of the final fibre could be obtained, since the main loss in this fibre was caused by the interface scattering and contaminations.

Drawn lamellar core fibre

We drew the highly-polished glass rod down to a diameter of around 1 mm on a fibre-drawing tower, and then inserted it into an extruded LLF1 jacketing tube. This rod-in-tube structure was then drawn down to fibre of the required size in several steps. Fig. 4.4(A) shows an optical micrograph of the preform with one jacketing tube. This was jacketed and drawn two more times to obtain a fibre with 1.2 μm core size and 50 μm outer diameter as shown in the electron micrograph in Fig. 4.4(B). A close-up of the core region of the fibre in Fig. 4.4(B) recorded using backscattered electrons is displayed in Fig. 4.4(C).

The lamellar structure in the core is easily visible in this micrograph. The bright regions in Fig. 4.4(C) are SF6 and the dark regions are LLF1. The thickness of the layers has been decreased to less than 200 nm, smaller than the wavelength of visible light. The small overall core diameter ensures that the fibre is single-mode or few-moded (depending on the wavelength), and is not expected to be important for the birefringence obtained. All the experimental measurements and discussions in the rest of this chapter are based on this fibre.

4.3.3 Diffusion effect during drawing processes

It is well known that during fibre drawing processes diffusion can occur at the interfaces between two kinds of different glass materials [72]. During the fabrication of our lamellar fibre, several jacketing and drawing processes were used to obtain the desired fibre core size. We believe that at each drawing step, diffusion occurred, especially during the last step when we drew the perform to the final fibre.

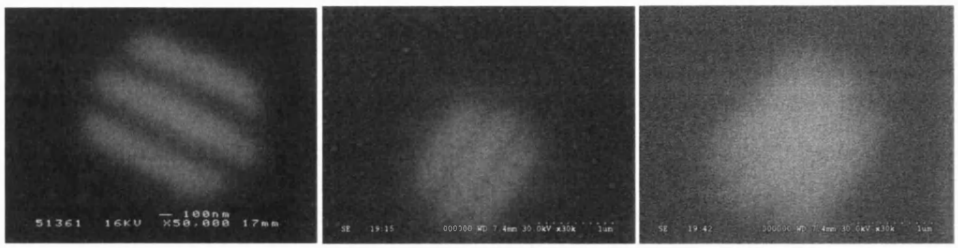

(A)
three jacketing tube

(B)
four jacketing tube

(C)
reheated in furnace

Figure 4.5: (A) Scanning electron micrograph (SEM) of lamellar core fibre with three jacketing tubes (core 1.2 μm). (B) SEM of Lamellar core fibre with four jacketing tubes (core 1.2 μm). (C) SEM of the fibre in (A) after reheated in the furnace.

Two scanning electron micrographs of lamellar core fibres with same core diameter (1.2 μm) are displayed and compared in Fig. 4.5(A) and (B). The only difference between them is that the first one was drawn by jacketing and drawing three times, and the other four times. The effect of diffusion on the structure is obvious: the LLF1 region (dark region in SEM image) in the core become much narrower in Fig. 4.5(B) than (A), coinciding with what we expected. After a piece of fibre in Fig. 4.5(A) was reheated in a furnace for a period of time, the core structure can hardly be seen, referred to Fig. 4.5(C).

To identify the diffusion effect by quantitative analyze, energy dispersive x-ray analysis (EDAX) was used to measure the concentration of lead (this element mainly exists in SF6 glass). The preform was reheated in a furnace at the temperature of 600 ^{o}C for 2 hours to simulate the diffusion that might occur during fibre fabrication, and as expected evidences of diffusion were found, shown in Fig. 4.6. The original LLF1 region was greatly narrowed, less than one third of the thickness of SF6 plate. This diffusion effect also reduced the refractive index contrast by rasing the index of the LLF1 plate and decreasing the index of the SF6 plates. Note that in Fig. 4.6 the Pb concentration of the LLF1 region between two SF6 plates is much higher than that in the cladding, which suggests the LLF1 region in the core has higher refractive index than the cladding. However, the spatial resolution of our EDAX system is insufficient to perform such measurements in the actual fibre.

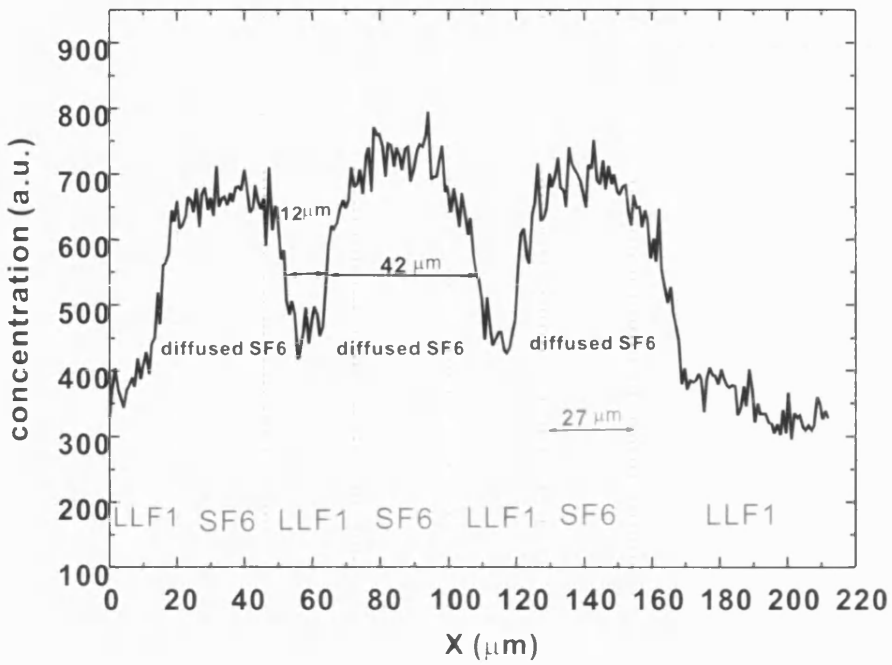

Figure 4.6: The Energy dispersive x-ray analysis (EDAX) of a reheated lamellar preform.

4.4 Linear properties

4.4.1 Waveguiding properties

The attenuation of the fibre shown in Fig. 4.4 was measured at the wavelength of 632 nm by the cutback method, yielding around 10 dB/m. The intrinsic losses of the SF6 and LLF1 glass are less than 1 dB/m in the visible and near-infrared spectral regions, and the high attenuation in the fibre is attributable to contaminations of the internal and external interfaces during the formation of the core material, which leads to increased scattering losses. Trapped air bubbles between the glass plates during the core material fusion can also contribute to the loss. The single mode cutoff wavelength is around 1.0 μm for the fibre with 1.2 μm core diameter. Diffusion is not expected to have much effect on the cutoff wavelengths for the higher order modes because the average core index remains very similar. Since the thickness of each layer is smaller than the visible light wavelength, we can consider the structured core as being formed from an anisotropic material.

4.4.2 Beat length measurement

Direct and indirect methods were used to measure the beat length of our lamellar core fibre.

Direct Observation of the beat pattern in the fibre

When light is propagating in an optical fibre and its coherence length is longer than the beat length, an accurate method of measuring birefringence is to count the number of beat lengths by viewing the light scattered through the side of the fibre caused by Rayleigh scattering [9]. Each scattering particle forms a radiation dipole excited by the light field. Radiation is maximum orthogonal to, and zero in line with, the direction of the field. Therefore, we can see the scattered pattern by observing the fibre at an angle of 90^o to the direction of polarisation of the light.

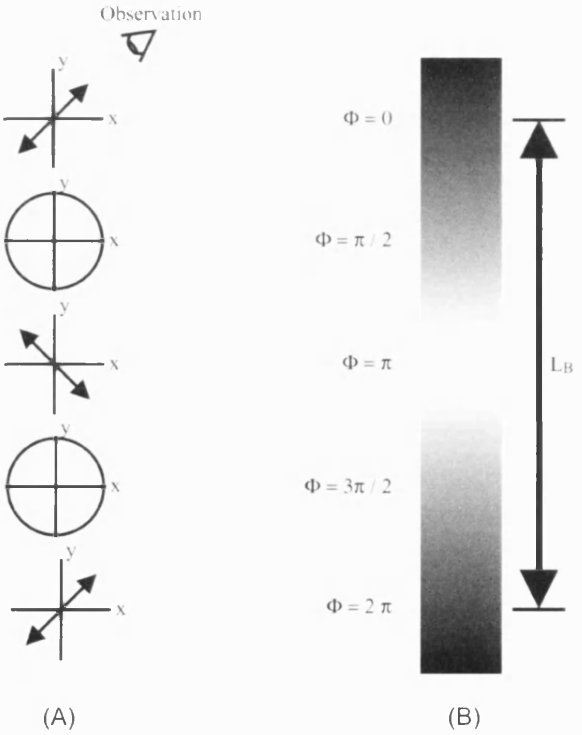

Figure 4.7: (A) Progress of the polarisation state of a linear polarisation light, which is launched into a fibre with 45^o to the birefringent axes. (B) Scattered intensity observed normal to the input light polarisation direction.

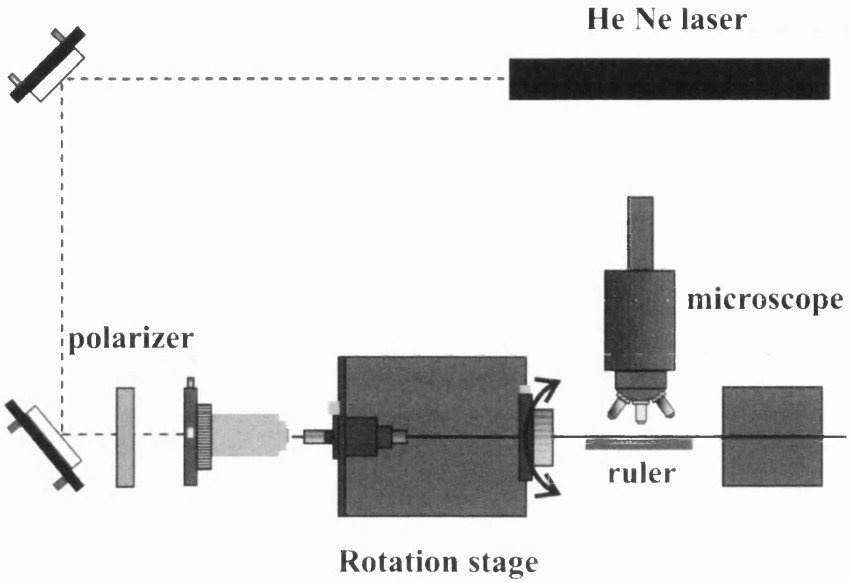

Figure 4.8: Experimental setup for the direct observation of the beat pattern.

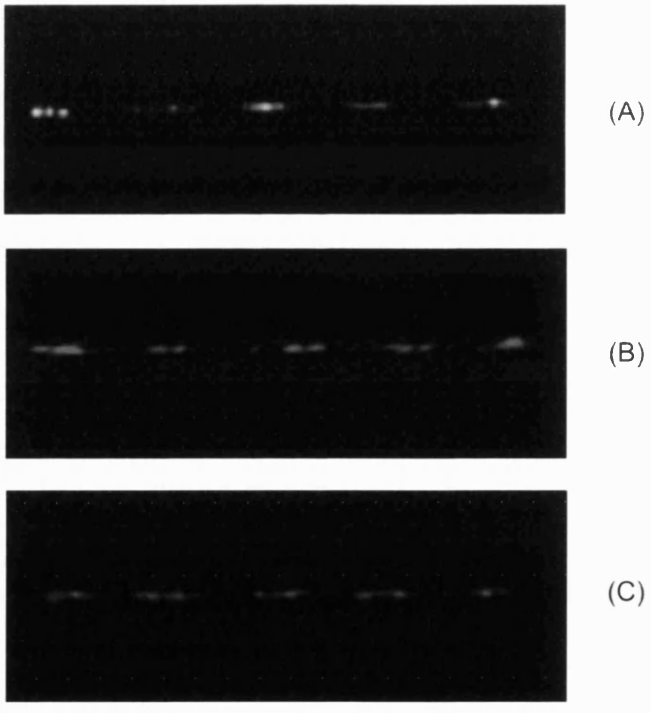

Figure 4.9: Optical micrograph of the beating in the fibre excited by three lasers with different wavelengths. (A) wavelength: 781 nm, beat length: 140 μm. (B) wavelength: 632 nm, beat length: 100 μm. (C) wavelength: 543 nm, beat length: 85 μm.

If linearly polarised light is launched into a fibre with the direction of polarisation at 45^o to the birefringent axes, the polarisation along the fibre will progress from linear to elliptical to circular to elliptical to linear, as it propagates (see Fig. 2.6). This means that, if we observe the fibre at an angle of 90^o to the input light polarisation direction, periodic light patterns can be seen and counted.

An experimental rig was set up, shown in Fig. 4.8, to measure the beat length of our fibre. The observation direction (optical microscope direction) was kept at 90^o to the direction of the polariser. The fibre was rotated to permit the linear polarisation light to be launched into the fibre at 45^o to the birefringent axes. A steel rule was used as a reference to measure the beat length.

Fig. 4.9 shows optical micrographs of the beat patterns using three different lasers, with working wavelengths of 781 nm, 632 nm and 543nm, respectively. The minimum observed beat length using a Green HeNe laser (543nm) was measured to be 85 μm, while the beat lengths at 632 nm and 781 nm are 100 μm and 140 μm, respectively. The measured errors are estimated to be within $\pm 1.5\%$. According to the measured beat length and Eq.(2.13), we obtained the phase-index birefringence of 6.4×10^{-3} at the wavelength of 543 nm, which is the highest reported birefringence in a single-mode fibre.

Indirect measurement approach

An indirect measurement method was also used to measure the beat length of the fibre. In fact, this kind of method is especially useful for PCF with structures in the cladding whose beat length cannot be measured by the direct observation method.

One method that can be used is launching light from a tunable diode laser (also with polarisation direction at 45^o to the fibre principal axes) into a fibre with length of L, and monitoring the output polarisation state as a function of wavelength [58]. This method is referred to as wavelength scanning technique. A sketch of measurement setup is shown in Fig. 4.10(A).

As the wavelength is scanned, there should be a beating pattern with respect to wavelength recorded by the computer [58]. The relation between the wavelength beat period and the beat length of fibre can be obtained by differentiating

the expression of the difference of phase between the two fundamental modes, Eq.(4.8).

$$\phi = (\beta_x - \beta_y)L = \frac{2\pi L}{L_B} \tag{4.8}$$

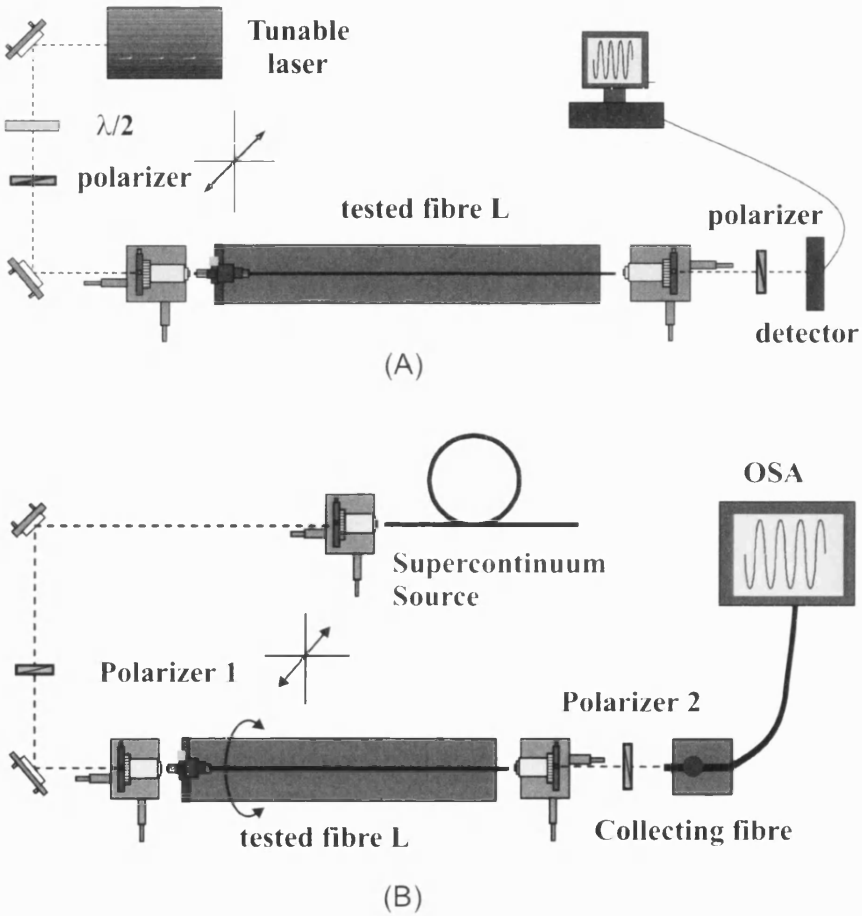

Figure 4.10: Experimental setups for indirect measurement of beat length. (A) Using tunable laser as source and scanning the light wavelength to obtain the beat pattern. (B) Using supercontinuum source and recording the beat pattern directly by OSA.

Making the total phase change equal to 2π for a beat period leads to

$$\Delta\lambda = \frac{L_B^2}{L|\frac{dL_B}{d\lambda}|} \tag{4.9}$$

If we assume $L_B \propto \lambda^k$, there is a simple closed form solution for the beat length, given by

$$L_B^{approx} = \frac{Lk\Delta\lambda}{\lambda} \tag{4.10}$$

An improved measurement method using supercontinuum light as source and optical spectrum analyzer (OSA) as recorder is shown in Fig. 4.10 (B). Polariser(1) was used to make the input supercontinuum source linearly polarised. The fibre was laid on a flat metal base to avoid bending effects. The fibre could be rotated so that the polarised light was correctly launched into the fibre at an angle of 45° to its principle axes. This was verified by checking that the intensity of the output light after polariser (2) remained unchanged when polariser (2) was rotated. This was due to the fact that the broad supercontinuum spectral output (>1000 nm) was much broader than the fibres beating period (measured to be 5.6±0.2 nm in Fig. 4.11) and thus contained many beating periods, so at this light launching condition (linearly polarised direction was at 45° to the fibre principle axes) even though light of a fixed wavelength had a specific polarisation state (linear, elliptical or circular), the total output power for the whole supercontinuum would be expected to have no polarisation dependance.

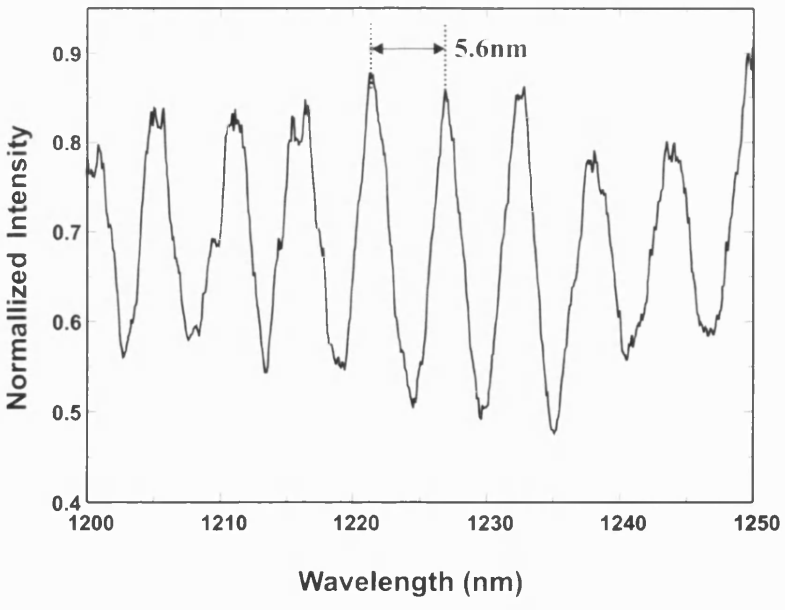

Figure 4.11: Recorded beat pattern by using experimental setup shown in Fig.4.10(B). The period is 5.6±0.2 nm, and the fibre length is 36±0.5 mm.

The results for a scan from 1200 to 1250 nm, shown in Fig. 4.11, indicated clear polarisation beating for a fibre with the length L of 36±0.5 mm. Theoretical calculations of birefringence and beat length provided the approximate k-value in Eq.(4.10), which is 1.8. Using this value in Eq.(4.10), the beat length at the wavelength of 1225 nm was about 295 μm, corresponding to the birefringence of 4.2×10^{-3}.

4.4.3 Differential group delay

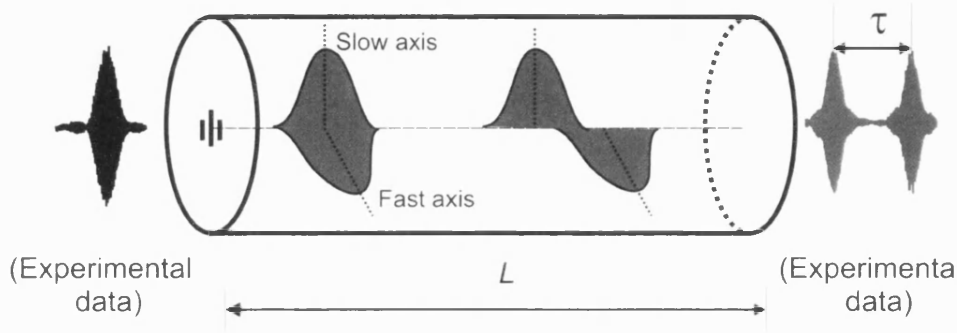

Figure 4.12: Demonstration of differential group delay during the propagation of a pulse in a lamellar core fibre.

When a pulse is launched into a birefringent fibre of length L with two fundamental polarisation modes excited, the high birefringence makes the group velocities for these two modes quite different, causing delay between them, referred to as *Differential Group Delay* (*DGD*). The pulse can be spread out or even split into two separate pulses with orthogonal polarisation states. The relation between the two polarisation modes delay τ (shown in Fig. 4.12) and group velocity v_g can be expressed as

$$\tau = \left(\frac{1}{v_g^x} - \frac{1}{v_g^y}\right) L = \frac{(n_g^x - n_g^y)L}{c} = \frac{B_g L}{c} \tag{4.11}$$

where n_g is the effective group refractive index and B_g is group birefringence of the fibre with the definition of B_g=$n_g^x - n_g^y$. According to Eq.(2.9), the relation between effective group refractive index n_g and effective modal refractive index n can be written as

$$n_g = n - \lambda\frac{dn}{d\lambda} \tag{4.12}$$

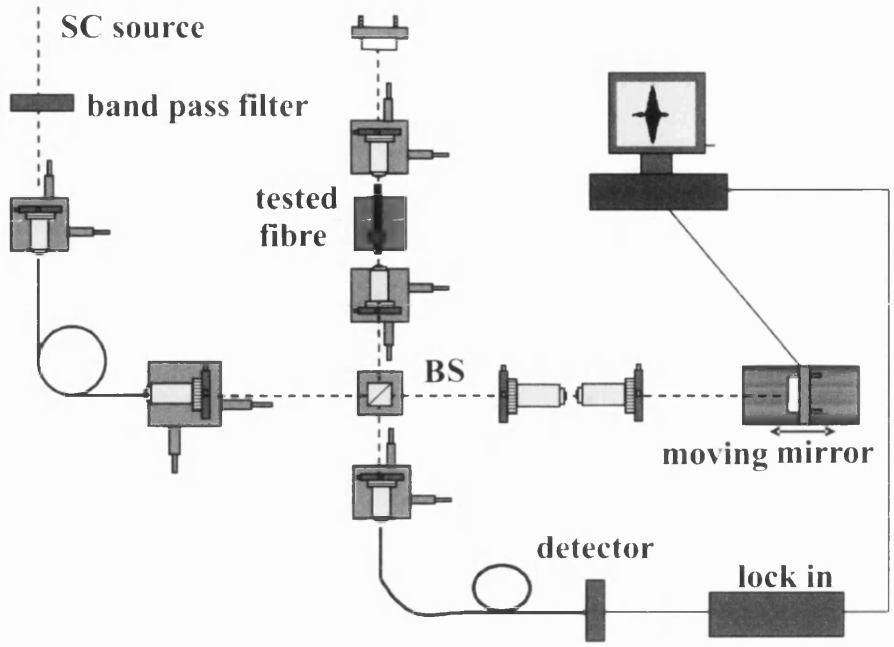

Figure 4.13: Experimental setup used to measure the differential group delay.

Substituting Eq.(2.12) and Eq.(4.12) into Eq.(4.11), the delay τ can be expressed as

$$\tau = \frac{\left(B - \lambda \frac{dB}{d\lambda}\right) L}{c} \tag{4.13}$$

In our discussion here, τ/L (equal to B_g/c) is used to identify the DGD property of our birefringent fibre.

Low coherence interferometry measurement method was used to measure the DGD of our lamellar core fibre. A Michelson interferometer was set up as shown in Fig. 4.13. The tested fibre with length of 80 mm was placed on one of the arms whilst the other arm was mounted with a travelling mirror in order to vary its length. A supercontinuum source was used as the light source and band-pass filters with a bandwidth of 10 nm were used to select the desired wavelengths. The measured wavelength ranged from 850 nm to 1600 nm. Due to the high birefringence of the lamellar core fibre, the two interference fringe peaks could be completely separated, which were recorded directly by our system. A typical observed interferogram is shown as the output pulses in Fig. 4.12. The distances between these two split pulses were recorded and used to obtain the DGD-value

for the corresponding wavelengths. The experimental errors of the final measured DGD are mainly due to the identification of the interference peaks positions and the measurement of the fibre length, estimated to be about ±1.5%.

The measured DGD is displayed in Fig. 4.14. It is about 29.3±0.8 ps/m at a wavelength of 1540 nm, deducing the group-index birefringence of about 8.8×10^{-3} at this wavelength.

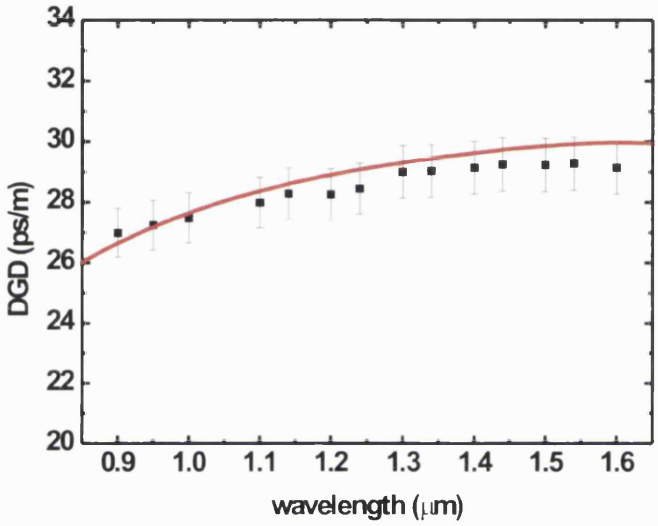

Figure 4.14: The differential group delay for the two fundamental polarisation modes. The black dotted line: experimental results (measured fibre length 80±0.5 mm); The red line: numerical modelling result taking account of the diffusion in the core (see Fig. 4.16.)

4.5 Numerical modelling

From the experiments carried out, It can be seen that all the measured birefringence is much lower than the material birefringence of 0.018, obtained by the Born & Wolf approximation in section 4.2. This can be attributed to diffusion effects, which reduce the refractive index contrast of the two glass materials in the core region. Numerical modelling results for the cases with and without diffusion

are provided in this section.

4.5.1 Modelling based on bulk material constant

A commercial beam propagation method [73, 74, 75] software package (BeamProp) was used to compute the effective indices for the two fundamental polarisation modes and the birefringences, as presented in Fig. 4.15. The core region of this modelled fibre has 7 layers of glass plates with the same thickness, of which 3 layers are SF6 glass and the others are LLF1, seen in the Fig. 4.16(A). The refractive index profile across the centre of the glass plates is provided in Fig. 4.16(C) (dotted black line), with the SF6 being assigned a refractive index value 1.79 and the LLF1 index assumed to be 1.54 (corresponding to their known values at a wavelength of 706 nm). The whole diameter of the core set to be 1.2 μm is the same with the fibre, shown in Fig.4.4. In Fig. 4.15, the polarisation directions parallel and perpendicular to the plate surfaces are marked as y and x direction, respectively. This case does not take account of the effect of diffusion.

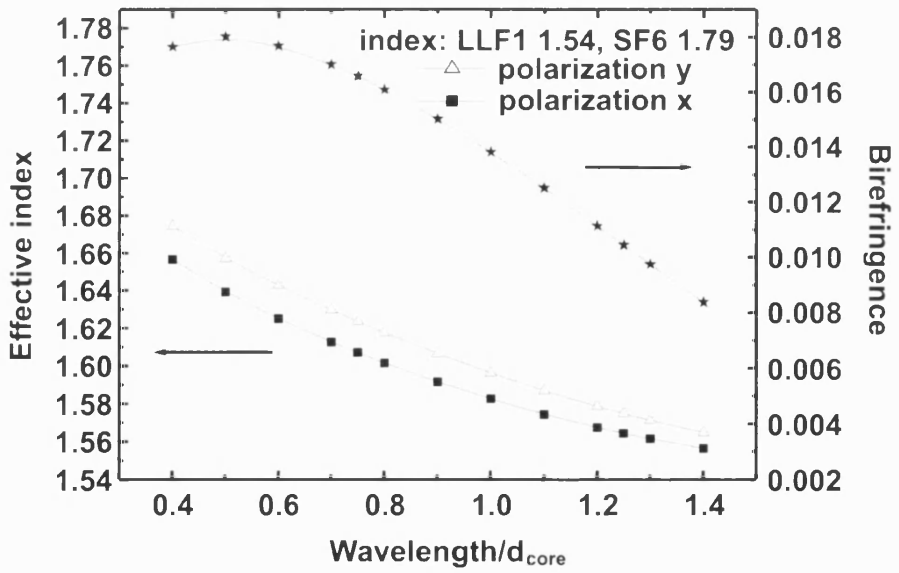

Figure 4.15: Beamprop modelling results for the effective indices of two fundamental polarisation modes and the birefringences.

We can see that, when the ratio of wavelength to core diameter is around 0.5, the birefringence reaches a peak value of 0.018. This modelling result is similar to the birefringence obtained for layers formed from infinite plates, implying that

the outside shape of the core is not the main contributor to the birefringence. This value of expected birefringence is about one order magnitude higher than the highest reported birefringence in other fibres.

Since the measured birefringence at 543 nm wavelength, about 6.4×10^{-3}, is only about one third of the expected value of 0.018, further modelling accounting for diffusion effects was carried out to explain the measured results.

4.5.2 Accounting for the effect of diffusion

In this modelling, it was assumed that the diffused region was limited to the core region, shown in Fig. 4.16(B). Since LLF1 and SF6 glass in the core region had

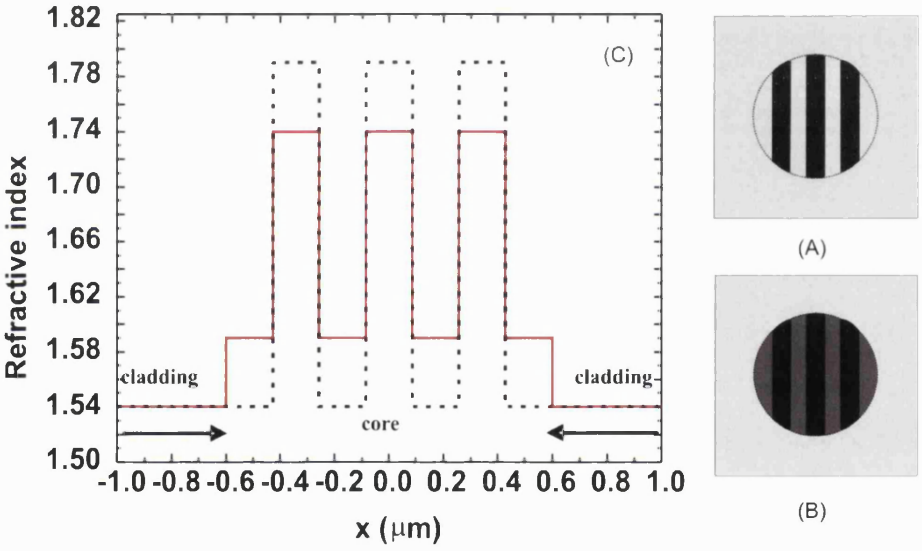

Figure 4.16: The refractive index distributions assumed in the fibre. (A) Core structure with SF6 and LLF1 glass plates without diffusion (dark region: high index, bright region: low index). (B) Assumed diffused core structure. (C). The black dotted line: bulk material index constants (as used in producing Fig.4.15). Red solid line: assumed result of diffusion during fibre drawing (as used to produce numerical results in Fig.4.14 and Fig.4.17).

almost the same volume, another assumption we made was that the decreased index of SF6 glass was the same as the increased index of LLF1 glass. We found that using the Born & Wolf approximation in Section 4.2 a relatively modest change in the refractive index contrast between the two phases (eg, 1.74:1.59

rather than 1.79:1.54) would be sufficient to explain the measured decrease in birefringence. So the refractive index contrast of 1.74:1.59 was used to compute the effective indices for the two fundamental modes in the fibre using BeamProp. The refractive index distribution assumed is presented in Fig. 4.16(C) as a red solid line.

From the output of the software (the effective indices for the two fundamental guided modes at different wavelengths) we computed the beat lengths and differential group delays, as plotted in Fig. 4.17 and Fig. 4.14 (solid red lines). The excellent agreement between the experimental and modelling results provides strong evidence supporting that significant diffusion did occur within the fibre core during the drawing process.

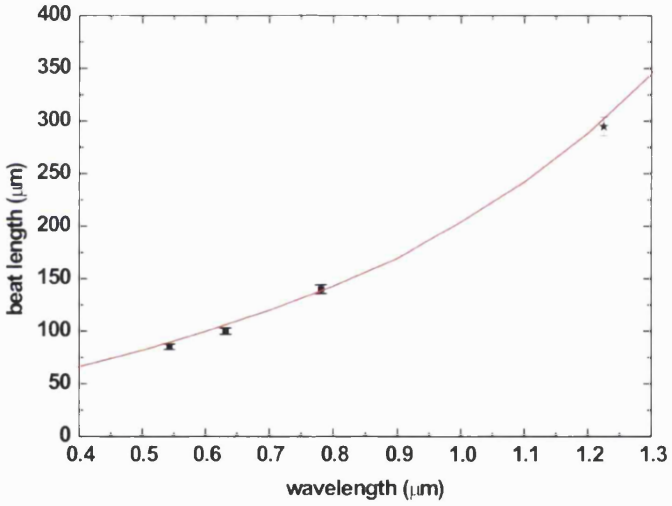

Figure 4.17: Beat lengths at different wavelengths. The black square dots: directly measured beat lengths at the wavelengths of 543 nm, 632 nm and 781 nm. The black star: indirectly measured beat length at the wavelength of 1225 nm. The red line: numerical modelling result accounting for diffusion in the fibre core (see Fig.4.16).

4.6 Conclusion & further improvements

4.6.1 Conclusion

We have described a highly birefringent lamellar core fibre. The beat length of the fibre was measured by direct observation of scattered light, and found to be 85 μm at a wavelength of 543 nm, corresponding to a birefringence of 6.4×10^{-3}. An indirect method was also used to measure the birefringence at infrared wavelengths. The differential group delay was measured using low coherence interferometry. We have computed the modal indices using a commercial beam propagation tool, and find that the measured values are not consistent with preservation of the bulk refractive indices within the multilayer stack forming the core. The decreased refractive index contrast within the fibre core can be attributed to diffusion of components within the multilayer structure. When accounting for modest diffusion, the modelling results fit well with the experimental results.

4.6.2 Further improvements by drilling glass rods

There are two main problems with our lamellar core highly birefringent fibre: one is the high loss, about 10 dB/m; the other is that the diffusion effect decreases the obtained birefringence. These two weaknesses can possibly be improved by further developing our fabrication technique with these soft glasses.

During the process of fabricating the lamellar core fibre, we jacketed and drew the original preform down at least three times using extruded LLF1 jacketing tubes to obtain the desired small core size. As discussed in section 3.5.1, it is quite difficult to prevent metal contaminations (from the metal die) and crystallization occurring on the surface of the extruded tube or preform. We believe these contribute to the high loss of the final fibre. Furthermore, the diameter of the extruded tube used is limited to about 2 mm, as larger uniform tubes are difficult to produce using our extrusion technique. As a result, a multi-drawing process had to be used. We found that the more drawing processes were used, the more heavily the diffusion phenomenon happened. This caused the serious decrease of

the obtained birefringence. If we instead produce the jacketing tube by drawing down a tube made using a better controlled drilling and polishing technique, this situation could be improved.

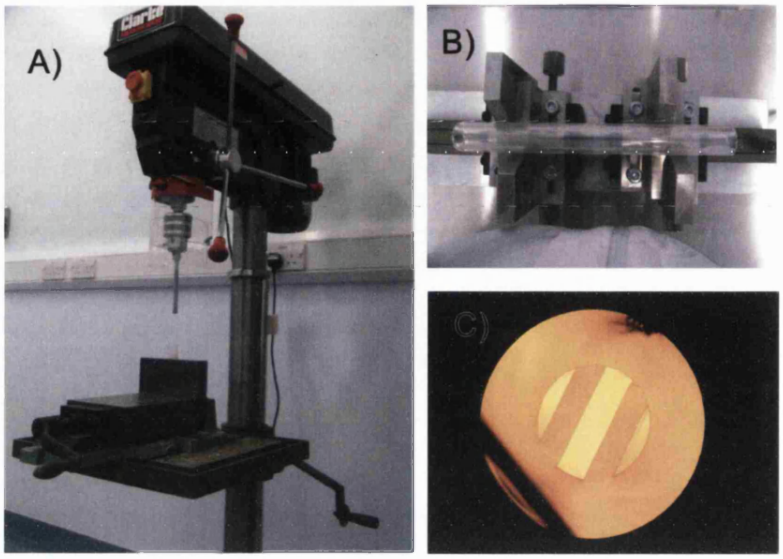

Figure 4.18: (A)Soft glass drilling apparatus. (B)Drilled and polished soft glass tube. (C)Lamellar core preform drawn directly from the drilled jacketing tube, which contains 5 layers of glass plates.

At present we can easily produce tubes by drilling of SF6 and LLF1 glass rods (length: 200 mm, outer diameter: 22 mm, drilled core diameter:10 mm to 16mm) using a common drilling machine and diamond core drilling bits, shown as Fig. 4.18(A). The polishing of the inner and outer surfaces of the drilled tube (shown in Fig. 4.18) can be operated in a lathe. Several layers of polished SF6 and LLF1 glass plates with thickness of around 2 mm and appropriate sizes can then be directly inserted into a drilled and well-polished LLF1 tube, before the whole structure is drawn into the lamellar core preforms (refer to Fig. 4.18(C)). During this drawing process a vacuum was used to eliminate air bubbles trapped at the interfaces of the adjacent glass plates. These could not be removed using the previous method. Hydrofluoric acid etching could also be used to remove the contaminations on the surface of the glass tube, introduced during the polishing. All these changes could contribute to a reduction of the high loss.

A set of jacketing tubes with different sizes could also be drawn directly from another drilled tube, and these multi-jacketing tubes could make it possible to

draw the preform to the final fibre with the desired small core size in a single step. We could also use the SF6 jacketing tube as an outer jacketing tube to decrease the diffusion effects. In fact, this kind of effect was discovered during the fabrication of all-solid PBGF, which is also composed of SF6 and LLF1 glasses: Diffusion always occurred when we used the LLF1 glass as the jacketing tube, destroying the guiding properties of the fibre; the fibre only worked properly with the SF6 glass as the jacketing tube. The reason for this can be understood by the different glass transition temperatures (T_g of LLF1 and SF6 glass, refer to Table 4.1): the drawing temperature of the bandgap fibre with LLF1 as the cladding (it means the fibre is mostly composed of LLF1 glass) must be higher than that of a bandgap fibre with SF6 cladding, so the diffusion effect was more serious for fibres with LLF1 cladding. These changes could contribute to an increase of the final birefringence.

Chapter 5

Three-level Neodymium fibre laser incorporating photonic bandgap fibre

5.1 Introduction

The strong spectral discrimination in the transmission of a photonic bandgap fibre makes it a good candidate for an in-line optical fibre filter. The concept is not dissimilar to another type of filtering fibre with resonant coupling between the core and cladding recently proposed as a means of distributed filtering along a gain medium [76]. As a filter, an all-solid PBGF is preferable to a hollow-core PBGF, because it can be spliced to conventional fibres more easily. Furthermore, the all-solid PBGF structure can also be used to realize a rare-earth doped active photonic bandgap fibre [77], which is impossible for a hollow-core PBGF.

In this chapter, I demonstrate the filter function of an all-solid PBGF by incorporating it into a Neodymium fibre laser system by simply splicing it to the Neodymium-doped fibre. Gain from the neodymium four-level transition was strongly suppressed using the bandgap fibre as an intra-cavity wavelength-relative loss element and our fibre laser ran easily and stably on the three-level transition.

5.2 Nd fibre laser introduction

5.2.1 Energy level diagram and the main transitions

Neodymium was first used as a gain medium in the first glass laser in 1961, a device that was demonstrated by Snitzer [78], not long after the first Nd^{3+} crystalline laser in the same year [79]. These were soon followed by a Nd^{3+}-doped fibre laser in 1963 [80] and an optical amplifier [81] in 1964. Afterwards, lasing in Nd-doped fibre laser systems at different wavelengths, mainly around 1.06 μm, 1.3 μm and 0.9 μm, were demonstrated [82, 83, 84, 85]. These different lasing wavelengths correspond to three different transitions of neodymium ions, which will be introduced in this section. In fact, neodymium ions have become one of the most important gain elements for crystalline, bulk glass and fibre lasers, due to the high power ability and high efficiency.

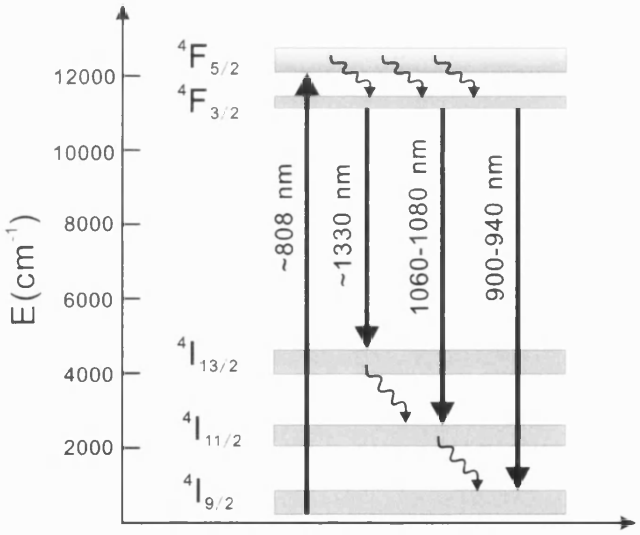

Figure 5.1: Energy levels and transitions involved in laser oscillations of Nd^{3+} ions in glass matrix.

Fig. 5.1 shows the relevant energy levels of the Nd^{3+} ions in silica [86]. The strong $^4I_{9/2} \longrightarrow {}^4F_{5/2}$ absorption transition at about 800 nm is extremely effective for exciting the $^4F_{3/2}$ metastable state, leading to very efficient Nd^{3+}-doped fibre lasers, which can be easily pumped by AlGaAs laser diodes.

The four-level $^4F_{3/2} \longrightarrow {}^4I_{11/2}$ transition gives emission around 1060 nm wave-

length [82, 83, 87]. This is probably the most thoroughly characterised of all laser transitions for both glass and crystalline hosts, due to its importance in high power and high efficiency laser applications. The 2000 cm^{-1} gap between $^4I_{11/2}$ and $^4I_{9/2}$ is small enough to provide a high nonradiative relaxation rate and prevent a buildup of population in the terminal level. The four-level scheme leads to no ground state absorption (GSA) at the laser wavelength. As a result, the internal gain for this transition is positive even for a vanishingly small pump power, as the threshold power for lasing can be very small [83].

On the other hand, the $^4F_{3/2} \longrightarrow {}^4I_{9/2}$ (900 nm) is a three-level system [84, 88, 89, 90]. Because it is limited by ground-state absorption and the strong competition with the four-level transition $^4F_{3/2} \longrightarrow {}^4I_{11/2}$ [84], it is non-trivial to realize lasing at this wavelength. My laser work in this chapter is based on this transition.

The $^4F_{3/2} \longrightarrow {}^4I_{13/2}$ transition corresponds to 1300 nm wavelength [85, 91, 92], and is also a four-level operation. The difficulty of lasing at this wavelength is that this scheme suffers from excited state absorption (ESA) ($^4F_{3/2} \longrightarrow {}^4G_{7/2}$, not given in Fig. 5.1), which considerably reduces the gain [92].

5.2.2 Three-level transition lasing

Although the 900 nm three-level transition has not been investigated as extensively as the 1060 nm four-level transition, it has attracted more and more attention recently due to applications such as water-vapor absorption characterisation, frequency doubling and spectroscopy. The first three-level transition laser in optical fibres was reported at 936 nm by L. Reekie, et.al [84], in 1987, by using dichroic mirrors with high wavelength discrimination.

The absorption spectrum of a Nd^{3+}/Al^{3+} co-doped silica fibre is provided in the upper diagram of Fig. 5.2 [93], while the lower diagram [88] shows the fluorescence spectra of a Nd^{3+}/Ge^{4+} co-doped fibre and a Nd^{3+}/Al^{3+} co-doped silica fibre pumped at 808 nm. These two fibres are all standard commercially available Nd^{3+} doped fibres.

The addition of Ge^{4+} ions does not alter the emission spectrum of Nd^{3+} doped pure silica fibre with respect to bulk Nd-SiO_2 glass. This type of fibre has at-

tracted attention because the secondary fluorescence peak near 938 nm (Fig. 5.2) overlaps a strong water vapor absorption band centred at 940 nm [94]. The highly doped fibre incorporating Al^{3+} codopant can remove clustering effects and is doped well beyond the solubility limit of Nd^{3+} ions in pure silica. The use of the Al^{3+} codopants (several mol %) can also blue-shift the emission spectrum by up to 25 nm [88, 95] (see Fig. 5.2).

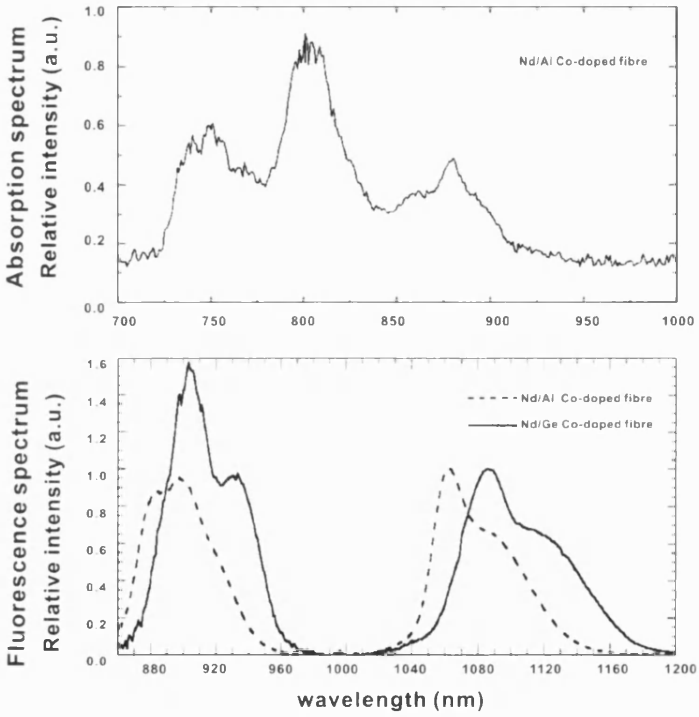

Figure 5.2: Upper: absorption spectrum of a Nd^{3+}/Al^{3+} co-doped fibre [93]; Lower: fluorescence spectra of a Nd^{3+}/Ge^{4+} co-doped and a Nd^{3+}/Al^{3+} co-doped fibre pumped at 808 nm [88].

The relative intensity of the fluorescence spectrum for the 900 nm transition is similar to that of the 1060 nm transition for an Nd^{3+}/Al^{3+} co-doped fibre and is actually much greater in the case of Nd^{3+}/Ge^{4+} co-doped fibre. This property could be exploited to make a laser emitting around 900 nm, however the strong absorption at the three-level transition bands and the competition from the 1060nm limit lasing at this wavelength.

Previous researchers have used a bent W-type index profile fibre to suppress the

longer-wavelength four-level transition of the Nd doped fibre [96]. In this chapter, we will present the use of an all-solid PBGF as a filter to suppress the gain of the 1060 nm transition, enabling a robust CW laser at the wavelength of 907 nm to be obtained. The used gain fibre is a Nd^{3+}/Ge^{4+} co-doped silica fibre. All the mirrors used have the same reflectivity for the wavelength range of 900-1100nm.

5.3 All-solid photonic bandgap fibre

5.3.1 Design of PBGF

During the design of the fibre the following criteria had to be fulfilled to realize the three level transition lasing: the fibre must suppress the 1060-1100nm transition of Nd^{3+} doped fibre, whilst allowing high transmission for the 808nm pump wavelength and the 900-940nm lasing wavelength. Photonic bandgap properties of an all-solid PBGF were designed to realize this wavelength-dependent attenuation. However, the first bandgap of an all-solid PBGF is almost semi-infinite at the long wavelength edge (refer to Fig. 3.3), which is not convenient to suppress the long wavelength signals. The following second bandgap was then considered as below.

First of all, the lowest transmission loss at the lasing wavelength was desired for an optimal bandgap fibre to be used in our Nd laser system. To realize this requirement, the three-level transition band (peaking at about 910 nm) was arranged to be located at the central frequency between the cutoff frequencies of LP_{11} and LP_{02}/LP_{21} modes, (corresponding to λ_1 and λ_2 in Fig. 3.3). The refractive index of the Ge-doped silica rod, which would be used to form the high-index inclusions in the cladding of the bandgap fibre, was known to be 2.03% higher than that of matrix material (pure silica with refractive index of 1.458). To realize the above requirement, the diameter of the high index inclusions (d-value) in the final fibre was calculated to be 3.1 μm, corresponding to the cutoff wavelengths of λ_1 and λ_2 to be 750 nm and 1195 nm, respectively. With these designed parameters, the lasing wavelength (around 910 nm) should be positioned at the centre of the bandgap with high transmission. And the pump wavelength (808 nm) was expected to be located on the blue side of this low loss transmission

window, whilst the four-level 1060-1100 nm transition band would fall into the high loss region.

The fabrication method of our bandgap fibre is shown in Fig. 5.3. Using this method, if the cladding rods had the diameter of 3.1 μm as we designed above, the core diameter of a final bandgap fibre was estimated to be about 10 μm. Meaning that it would be quite similar to that of conventional SMF28 fibre. If we used the third bandgap to satisfy the same requirement, the rod diameter had been calculated to be 4.3 μm, corresponding the core size of 14 μm. Such a big core size could make the bandgap fibre hard to splice to commercial standard fibres with low loss, so the second bandgap is the best candidate to work in our desired Nd laser system.

The outer diameter of our final PBGF was expected to be 125 μm, facilitating its splice to conventional commercial fibre. To ensure the correct fibre outer diameter (125 μm) and rod diameter (3.1 μm), a suitable jacketing tube had to be carefully chosen, for the final fibre fabrication process.

5.3.2 Fabrication

A modified stack-and-draw method was used during the manufacturing process. The stack design is shown in Fig. 5.3. A step index multimode fibre preform with a germanium-doped core and a thin pure silica cladding (index difference n=3.3×10^{-2} and core-to-cladding diameter ratio: 0.88), and a pure silica rod were drawn to canes with a diameter of 0.87 mm. The canes were then used to build the periodic structure in the cladding. The central area, which would have contained 6 pure silica rods and 1 germanium-doped silica rod, was replaced by one large pure silica rod to form the core of the fibre. The core is composed of only 1 missing unit cell in the final structure as shown in Fig. 5.4. 12 thin pure silica fibres (shown in the magnified core region in Fig. 5.3) were inserted into the gaps between the large central rod and the cladding structure to avoid any deformation of the structure near the core, and reduce the possibility of bubble formation by trapped air. Corner stacking rods were removed before the whole stacking structure was inserted into a pure silica jacketing tube. Additional 'filler' rods were used to keep the whole structure tight in the jacketing tube avoiding any deformation of the final drawn structure.

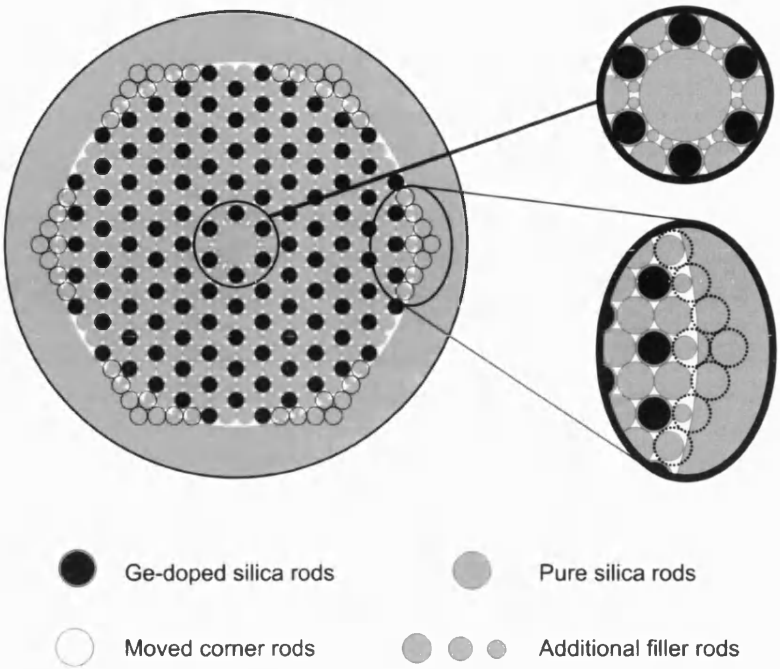

Figure 5.3: The multiple stack design of our all-solid PBGF. The diameters of the Ge-doped and pure silica rods are 0.87 mm.

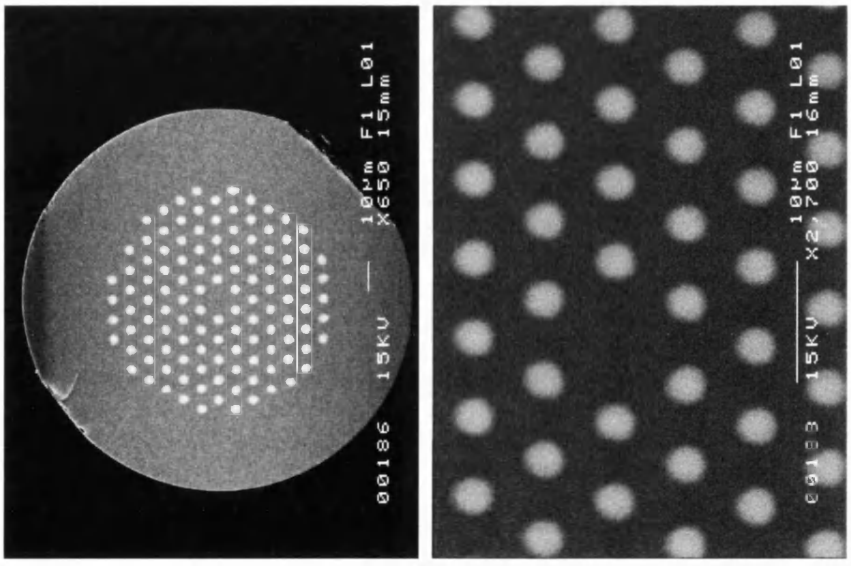

Figure 5.4: Backscattered electron images of the all-solid photonic bandgap fibre used in the experiments. The bright regions are Germanium doped, while the gray indicates pure silica.

This stack was then drawn to 2mm-outer-diameter preforms. A second jacketing tube was then carefully chosen to ensure that the final fibre with an outer diameter of 125 μm would have the correct internal cladding dimensions to suppress the 1060-1100 nm signal transmission, as was discussed in the Section 5.3.1. Scanning electron micrographs of the final fibre are shown in Fig. 5.4. The pitch in the periodic cladding and the diameter of the doped cladding rods were 6.5 μm and 3.1 μm, respectively, while the core diameter was 9.9 μm. Fibres with slightly different outer diameters were also drawn to compare the filtering effects of the slightly shifted transmission bands on our laser system.

By directly drawing the same 2 mm preforms from the original stack to a larger outer diameter, we could obtain fibres with higher order bandgaps at the visible and near-infrared wavelengths. This fibre was used to study the nature of the photonic bandgaps, especially bend loss properties. This work will be introduced in Chapter 6.

5.3.3 Modal profile

In order to assess the feasibility of splicing the PBGF to conventional fibre, the modal profiles of our bandgap fibre were studied. The near-field patterns at the fibre's output face were recorded by imaging onto a CCD camera with appropriate magnification. The supercontinuum source was spectrally filtered using a 10 nm band pass filter with central wavelength at 900 nm. This was coupled into an endless single mode PCF which was butted against a 20 cm length of PBGF.

After optimizing the alignment, the near field image of the core region was recorded, as displayed in Fig. 5.5. The mode is mainly confined in the core region but with some intensity extended into the 6 high-index inclusions surrounding the core. This 'star' shape is similar to the one predicted by N.M. Litchinitser et al. [43]. Fig. 5.5(b) represents the light intensity along the two white lines in Fig. 5.5(a). The experimental intensity profile (black curve) can be very well fitted by a Gaussian profile (red curve) in the X direction with a waist diameter (at $1/e^2$) of 8.5 μm and relatively well in the Y direction (waist diameter of 8.9 μm).

During the practical experimental process, various coupling conditions (off-axis,

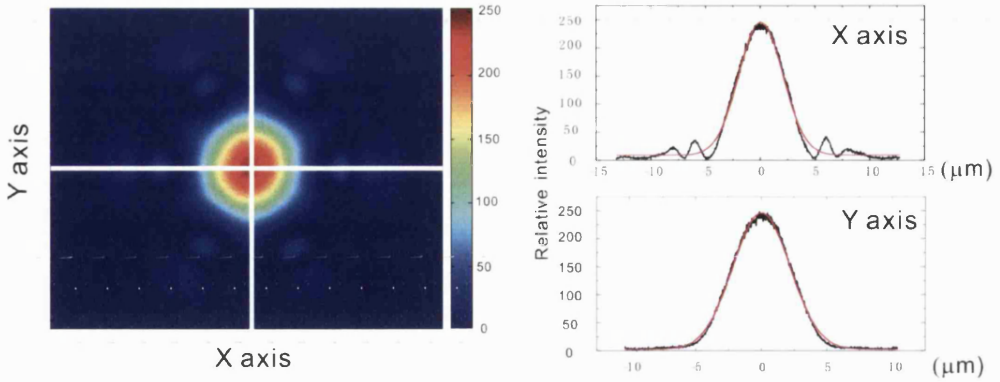

Figure 5.5: (a) Near field image of the guided mode observed at 900 nm. (b) Experimental intensity profiles (black curves) along the two axes X and Y shown on Fig.5.5(a). The red curves represent a Gaussian fit to the experimental data.

small spot, etc.) at different wavelengths were tried, but higher order modes were never observed. However, for very short fibre lengths (such as 20 mm), with the use of an optical microscope higher order modes could be observed. Due to the large difference of losses between the fundamental mode and higher order modes, our PBGF can be considered in practice as a single mode fibre, which ensures single-transverse-mode operation of the laser.

5.3.4 Insertion loss of PBGF device

To identify the filtering properties of our all-solid PBGF, a 10 cm length of the 125 μm outer diameter PBGF was spliced between two pieces of conventional single-mode fibre (1060XP from Thorlabs) using a standard arc fusion splicer, shown in Fig. 5.6. The detailed splicing parameters will be introduced in Section 5.3.5.

By using the cut-back method, the spectral insertion loss for this device was measured and is shown in Fig. 5.6. This presents the existence of 3 well-defined low-attenuation transmission bands from 500 nm to 1400 nm.

The first transmission window at the longest wavelength is a semi-infinite fundamental bandgap. The second transmission window from about 790 nm to 940 nm covers the pump wavelength (808 nm) and almost all of the three-level transition

$^4F_{3/2} \longrightarrow {}^4F_{9/2}$ (890-950 nm, corresponding the red dashed line in Fig. 5.6) of the Nd doped fibre, whilst the four-level transition $^4F_{3/2} \longrightarrow {}^4F_{11/2}$ (1060-1100 nm, corresponding the blue dashed line in the figure) falls into the high-loss spectral region between the first and second transmission windows. The attenuation at 900 nm is around 1.8 dB, which is attributed almost entirely to the splice losses.

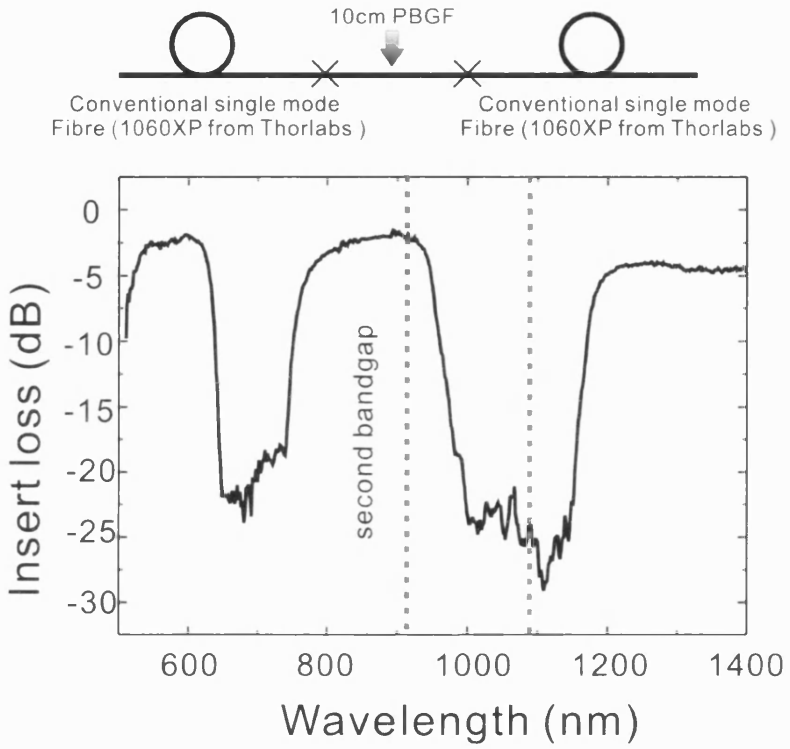

Figure 5.6: Insertion loss measurement of the spliced PBGF used in the laser experiments, recorded using the cut-back method.

5.3.5 Splicing of PBGF with other fibres

All-solid PBGFs can be spliced to conventional standard optical fibres by using a standard arc fusion splicer. For the results contained in this thesis, a Fujikura FSM-40PM ARC Fusion Splicer was used.

Since the objective is to incorporate a PBGF into the fibre laser system, the PBGF must be spliced to the Nd^{3+} doped fibre with low loss. The core diameter

of the Nd-doped fibre used is 3 μm, with an NA of 0.19 (Fibercore DF1000). The core is composed of Ge-doped silica containing 500-1000 ppm Nd^{3+} ions. Due to the significant mode mismatch between the Nd-doped fibre and the PBGF, it is impossible to obtain low splicing loss by splicing them together directly. Although a long arc exposure can diffuse the highly doped Nd fibre core to improve the mode-matching with the PBGF, it can also destroy the bandgap structure in the PBGF's cladding. The best splicing loss obtained was about 4-5 dB by this method. Finally, standard single-mode fibre (SMF, core diameter 5.5 μm, NA 0.14, 1060XP from Thorlabs) was used as an intermediary to splice the gain fibre to the PBGF, as shown in Fig. 5.7(A).

The measurement setups used to determine the best splicing parameters for the 'L' and 'R' splices are shown in Fig. 5.7. Due to the high absorption of the gain fibre at the 900 nm region, it is quite difficult to measure the splice loss between Nd fibre and SMF1060 fibre at this wavelength. However, only a small difference in splice loss at 900 nm and 1060 nm was expected, so a 1060 nm laser source was used to measure the splice loss, shown in Fig. 5.7(B). The output of the laser source was coupled to a SMF1060 fibre, the other end being coupled to a detector to record the original power value as the reference. Note that both ends of the SMF1060 fibre were coiled to avoid the emergence of high order modes. After the SMF1060 fibre was cut, a piece of Nd doped fibre was spliced in the middle and the splice loss was obtained. The same measurement process was carried out to measure the splice loss of PBGF to SMF1060 fibre, shown in Fig. 5.7(C).

To obtain an acceptable splice loss the most important splicing parameters which should be adjusted are the *arc fusion power*, *time* and *overlap* of the two spliced fibres. The overlap expresses the distance the fibres are push against each other after they come into contact.

During the splicing of the Nd fibre to SMF1060, the mode field diameter (MFD) of the Nd fibre can expand faster than that of the SMF1060. This is due to the high dopant concentration in the core of the Nd fibre. This effect is good since the MFD in Nd fibre is smaller than that of the SMF1060 fibre. Both the arc fusion power and time have a direct effect on the MFD expansion: by increasing the fusion time and/or power, a greater MFD expansion can be obtained. During the splicing process, monitoring the power detector can give an indication of any necessary change needed to these parameters: a monotonic increase of the optical

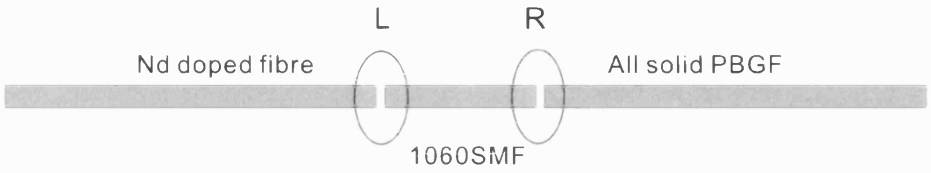

(A) Splicing design

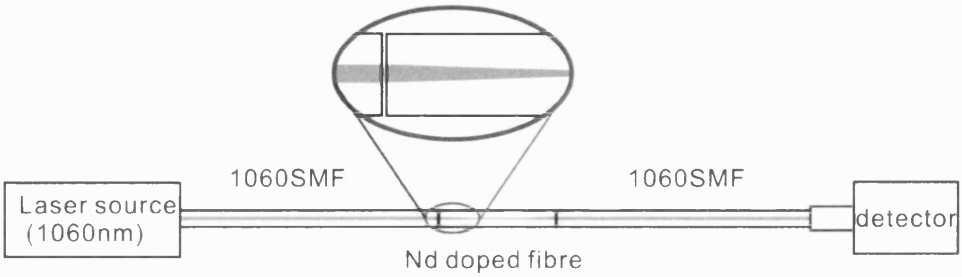

(B) Splicing at 'L' point, long arc exposure time

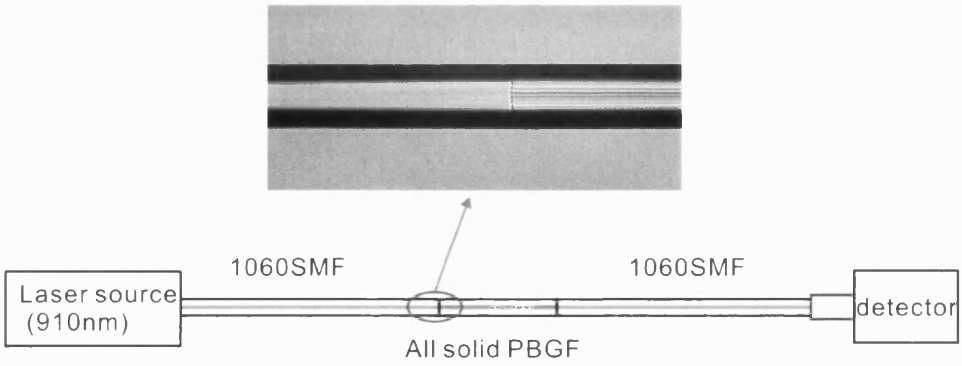

(C) Splicing at 'R' point, quick splice

Figure 5.7: Splicing of all-solid PBGFs to Nd doped fibres. Due to the big mismatch between the mode diameters of these two fibres, an intermediate conventional single mode fibre (1060XP from thorlab) was used to connect them, shown in (A). Experimental setups to measure the splicing losses between SMF1060 fibres and Nd doped fibres/all-solid PBGFs are provided in (B)/(C).

	Nd fibre to SMF	PBGF to SMF	SMF to SMF
XY Align	cladding	cladding	core
Arc1: Power (bit)	20	20	20
Arc1: Time (ms)	2000	1000	2000
Arc2: Power (bit)	20	20	20
Arc2: Time (ms)	10000	off	off
Overlap (μm)	15	5	15
splice loss (dB)	0.2	0.9	<0.1

Table 5.1: Splicing parameters of Fujikura FSM-40PM ARC Fusion Splicer for different kinds of fibres.

power means that the arc fusion time and/or power needs to be increased; first an increase in optical power followed by a decrease indicates excessive fusion time and/or power. After investigating the effects of arc time and power on several splices, the optimum parameters were found and are shown in Table 5.1. With these parameters a splice loss as low as 0.2 dB was obtained.

Considering the splice of PBGF to SMF1060 fibre, we should use a quick splice and less overlap to avoid the destruction of the bandgap cladding structure of the PBGF. The best splicing parameters are referred to in Tab. 5.1 and the splice loss obtained was 0.9 dB. By following this process, the total splice loss from Nd doped fibre to our PBGF with an intermediary can reach 1.1 dB, much lower than the value obtained by direct splicing.

5.4 Three-level Nd fibre laser incorporating PBGF

5.4.1 Configuration

Three different configurations were tried in order to achieve lasing in the Nd fibre. These are illustrated in Fig. 5.8.

A CW Ti:Sapphire laser tuned to 808 nm wavelength was used as the pump source for core pumping. The pump can pass through the dichroic mirror M1 with a

transmission coefficient of 80% at 808 nm, which was also used to reflect the signal with high reflectivity of 99% at 900-1100 nm. In configurations (A) and (B), the output laser had the same direction as the pump laser, while configuration (C) presents the reverse direction between pump and output lasers.

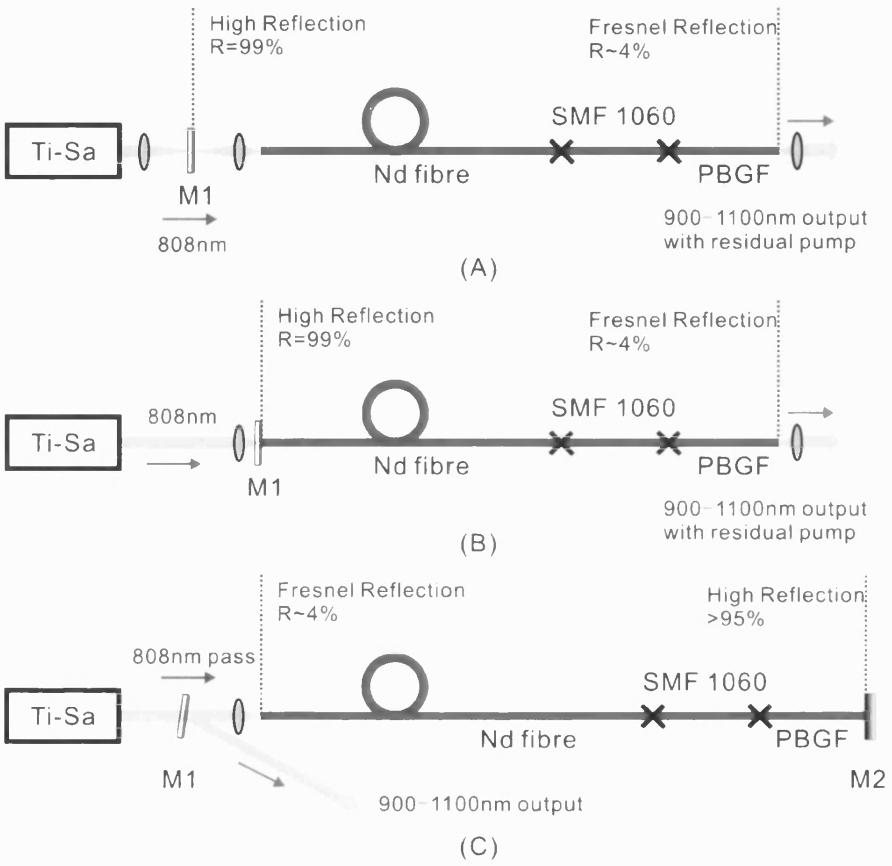

Figure 5.8: Three laser configurations designed for the three-level Nd-doped fibre laser. M1: Dichroic mirror with high transmission (80%) at 808 nm and 99% reflectivity from 900 to 1100 nm. M2: Metallic mirror with high reflectivity ($> 95\%$) from 800 to 1100 nm.

In configuration (A), the laser cavity was formed between the dichroic mirror M1 and the output cleaved end of PBGF with Fresnel reflectivity of 4%. The main problem in using this configuration is the difficulty of aligning the mirror M1. Another similar way was to directly butt the input end of Nd fibre against the mirror M1, which worked as one end of the laser cavity, shown in Fig. 5.8(B). However, the disadvantage with this method is that the pump coupling efficiency is decreased, thus the output power of the fibre laser is decreased.

Finally we obtained the best laser performance using configuration (C). The pump laser being positioned after the dichroic mirror M1 (transmission coefficient of 80%) was launched into the Nd-doped fibre with a coupling efficiency of 70%. The maximum pump power at 808 nm was 1.5 W and the overall pump launch efficiency was about 56%. The end of the PBGF was butted to a highly reflective metallic mirror M2, which has high reflectivity (>95%) at wavelengths 900-1100 nm, with the use of index-matching oil to form one end of the cavity. The other end of the cavity was the 4% Fresnel reflection of the Nd-doped fibre input end face. The laser was coupled out by mirror M1. A 10 cm length of PBGF (as demonstrated in Fig. 5.6) was found to be enough to suppress lasing on the four-level transition around 1080 nm.

Note that all the mirrors used in our experiment have the same reflectivity for the wavelengths from 900-1100nm, which means the effect of suppressing the four-level 1080nm transition was solely due to our PBGF.

5.4.2 Laser properties

For the three-level laser system, the Nd-doped fibre has an optimum length that is a balance between signal reabsorption and pump utilization. By cutting back from a fibre length of 5 m and characterising the maximal slope efficiency for each step, the optimal length of gain fibre was found to be around 2.5 m.

The measured output power of the fibre laser at the lasing wavelength of 907 nm versus Nd fibre length is displayed in Fig. 5.9. The pump power of the Ti:Sapphire laser was kept at 1.5 W.

Fig. 5.10 shows the laser spectrum obtained using a 2.5 m Nd-doped fibre and a 10 cm length of bandgap fibre. The spectrum shows that the desired signal at around 907 nm is 55 dB higher than that at 1080 nm, which means the four-level transition is strongly suppressed by the PBGF.

Data demonstrating the slope efficiency of this laser is presented in Fig. 5.11. The lasing threshold is about 70 mw launched pump power and the slope efficiency is about 32%, similar to the results reported in [84]. The highest slope efficiency reported using other method of wavelength selection is around 58%, obtained

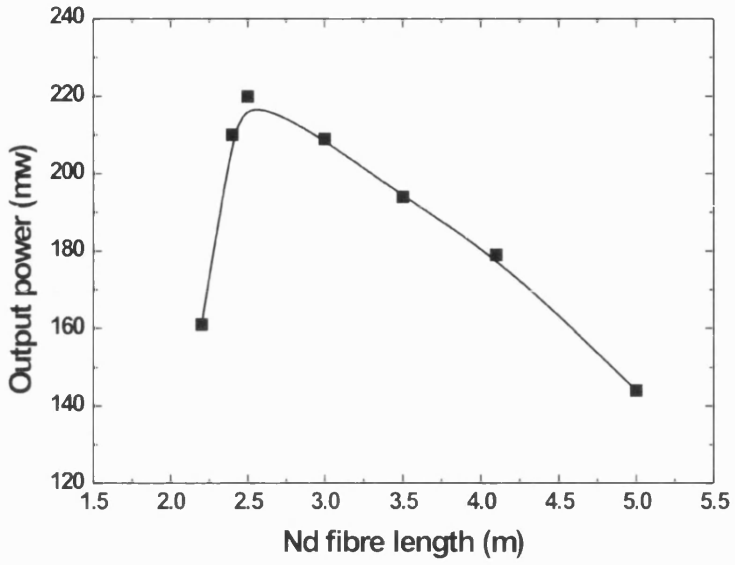

Figure 5.9: Three-level laser output power versus the Nd fibre length.

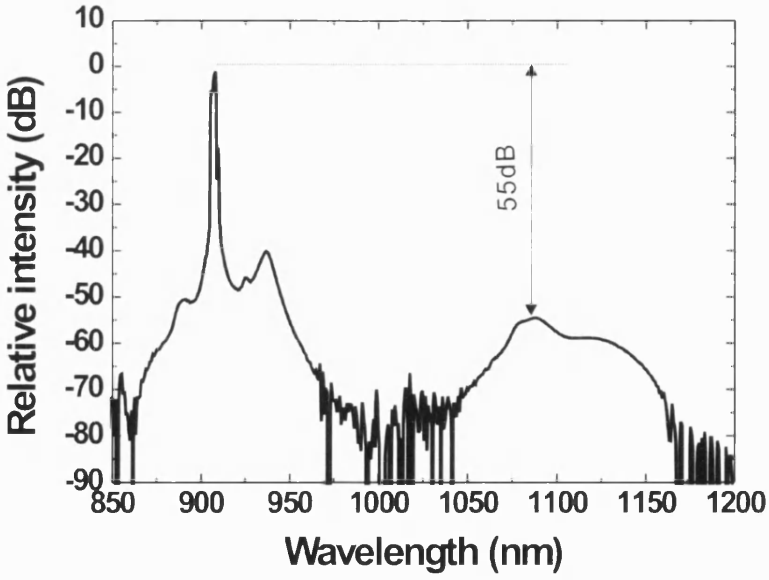

Figure 5.10: Optical spectrum of the Nd doped fibre laser incorporating a 10 cm length of all-solid PBGF (pitch 6.5 μm).

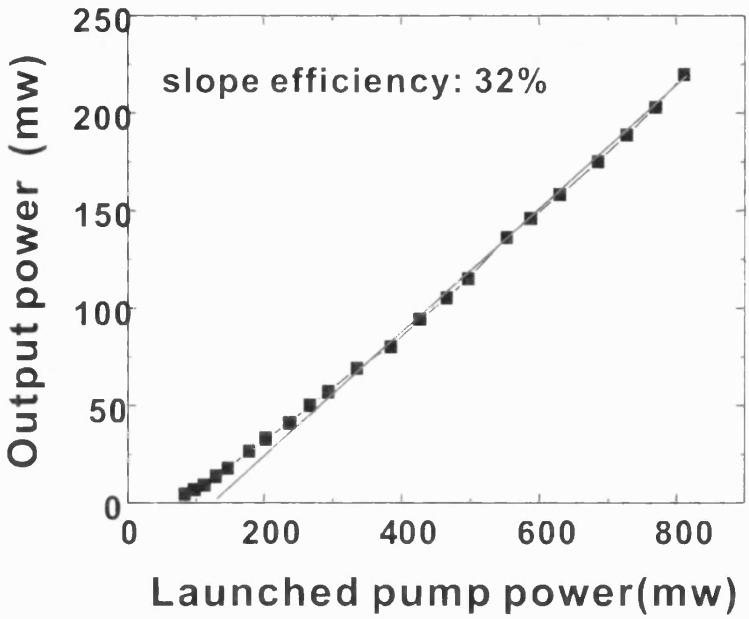

Figure 5.11: Measured slope efficiency of the Nd doped fibre laser incorporating a 10 cm length of PBGF (pitch 6.5 μm).

with a more highly doped fibre [93].

5.4.3 Effect of the splicing loss to laser output power

To evaluate the effect of the splice loss (between our all-solid PBGF and Nd gain fibre) on the laser performance, we used Rigrod analysis [97], which is an analysis of the power output based on a homogeneous laser with arbitrarily large round-trip gain and output coupling. The cavity is assumed to have its losses concentrated near the mirrors without distributed losses, which is a suitable comparison to low loss optical fibre. Despite the relative complexity of our system, this simple calculation provides a valuable insight into the relation between laser output power and splice loss.

Our laser resonator can be schematically presented in Fig. 5.12. Cavity end '**1**' is one cleaved end of Nd doped fibre with the reflectivity (r_1) of 4% and transmission ($t_1 = 1 - r_1$, where the loss is neglected) of 96%. The spliced SMF1060 fibre and bandgap fibre with a high-reflectivity metal mirror worked as an effective wavelength-relative loss mirror in this laser configuration, constructing another

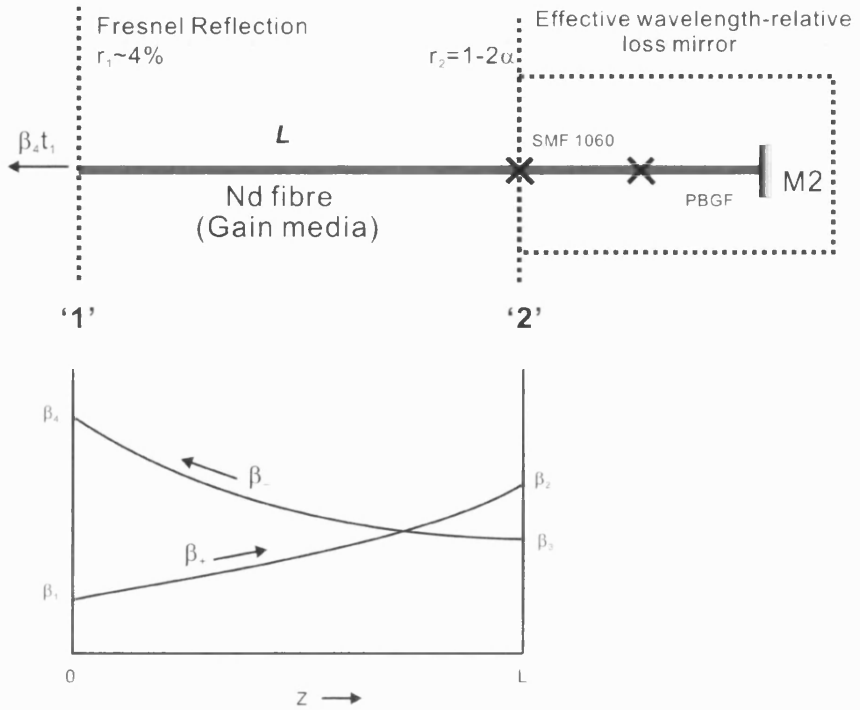

Figure 5.12: Schematic diagram showing normalized levels of flux intensity in both directions in our laser oscillator.

cavity end '**2**'. Only considering the splice loss (α) between the bandgap fibre and Nd fibre and approximately assuming the reflectivity of the metal mirror to be 100%, the effective reflectivity at the cavity end '**2**' r_2 is obtained by

$$r_2 = 1 - 2\alpha \tag{5.1}$$

where 2α means the light passed through the splice points twice at the end '**2**'. The gain media length, L, is the gain fibre length. We denote the normalized radiation intensities in the $+z$ and $-z$ directions of a laser oscillator by $\beta_+ = I_+/I_0$ and $\beta_- = I_-/I_0$, respectively, where I_0 is the saturation parameter.

The saturated gain coefficient $g(z)$ is assumed to be related to the unsaturated gain coefficient g_0 by [98]

$$g(z) = \frac{g_0}{1 + \beta_+ + \beta_-} \tag{5.2}$$

As the gain coefficient is isotropic, we have

$$g(z) = \frac{1}{\beta_+}\frac{d\beta_+}{dz} = -\frac{1}{\beta_-}\frac{d\beta_-}{dz} \tag{5.3}$$

from which we can see that

$$\beta_+\beta_- = \text{constant} = \text{C} \tag{5.4}$$

When oscillations stabilize, according to the boundary conditions, we have the relation:

$$\frac{\beta_2 r_2}{\beta_3} = \frac{\beta_4 r_1}{\beta_1} = 1 \tag{5.5}$$

where β_i $(i = 1, 2, 3, 4)$ is denoted in Fig. 5.12. Integrating the Eq.(5.2) for power flow

$$\pm\frac{1}{\beta_\pm}\frac{d\beta_\pm}{dz} = \frac{g_0}{1 + \beta_\pm + C/\beta\pm} \tag{5.6}$$

we obtain

$$g_0 L = ln(\beta_2/\beta_1) + (\beta_2 - \beta_1) - C(1/\beta_2 - 1/\beta_1) \tag{5.7}$$

and

$$g_0 L = ln(\beta_4/\beta_3) + (\beta_4 - \beta_3) - C(1/\beta_4 - 1/\beta_3) \tag{5.8}$$

Making use of Eq.(5.5),(5.4), (5.7) and (5.8), we obtain

$$\beta_4 = \frac{\sqrt{r_2}}{(\sqrt{r_1} + \sqrt{r_2})(1 - \sqrt{r_1 r_2})}[g_0 L + ln\sqrt{r_1 r_2}] \tag{5.9}$$

Because the output cavity end is end '**1**,' the normalized output laser power β_{out} can be expressed as

$$\beta_{out} = \beta_4 t_1 = \frac{t_1\sqrt{1-2\alpha}}{(\sqrt{r_1} + \sqrt{1-2\alpha})(1 - \sqrt{r_1(1-2\alpha)})}\left[g_0 L - \ln\left(\frac{1}{\sqrt{\mathrm{r_1}(1-2\alpha)}}\right)\right] \tag{5.10}$$

Because the unsaturated gain coefficient $g_0 L$ increases linearly with the pumping power and saturation parameter I_0 is most often independent of pump power, we can see that when $g_0 L$ becomes higher than cavity loss (the threshold condition), the output power of the laser will rise more or less linearly with the pump power.

In our laser configuration, the whole cavity loss was about 16.2 dB, composed of the output loss at cavity end '**1**' (14 dB, corresponding to 96% output) and double the splice loss (2.2 dB) at cavity end '**2**'. According to Fig. 5.11, at

the threshold condition with coupled pump power of about 70 mw, the whole gain of the cavity, G_0 ($G_0 = e^{2g_0L}$), is equal to the whole cavity loss, 16.2 dB, corresponding to g_0L of 1.8. Because g_0L is proportional to the coupled pump power, when the pump power reaches 800 mw (the upper limit in our pump system), g_0L increases to about 21, corresponding to the small signal gain of the cavity of 90 dB. Substituting $r_1 = 4\%$ and $g_0L = 21$ into Eq.(5.10), we obtain the relation between relative output power and splice loss, shown in Fig. 5.13. Two dashed lines correspond to the splice losses of 1.1 dB (our actual splice loss) and 0.5 dB, respectively.

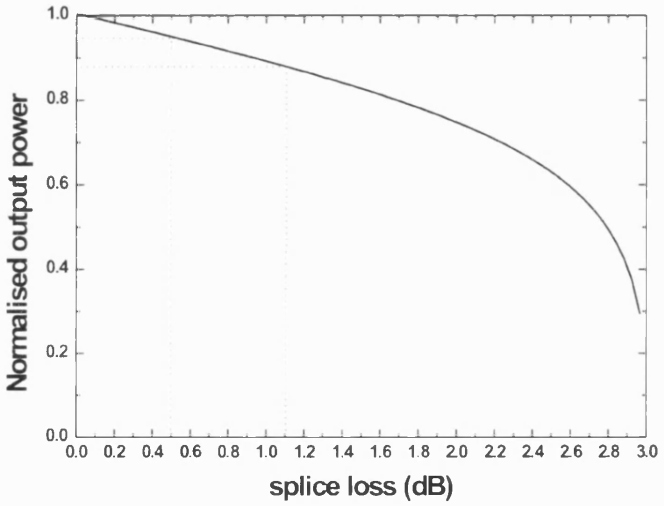

Figure 5.13: Modelled normalised power output versus the splice loss of the bandgap fibre to the Nd doped fibre.

The results show that in our laser configuration a slight output improvement can be obtained if we can reduce the splice loss from 1.1 dB (several percent increase if the splice loss can be reduced to 0.5 dB). In fact, by slightly bending the PBGF, an extra loss can be introduced in the cavity end '**2**' to reduce its reflectivity, which did not cause sensitive output power changes in the practical experimental process. All this indicates that for the low loss cavity end '**2**' (compared to cavity end '**1**') further improvements in reflectivity will not make much improvement to the output power and slope efficiency, so the result of our splice loss is good enough for our laser system.

5.5 Further demonstrating the filter function

5.5.1 PBGF with slightly different sizes

Replacing the PBGF with similar fibres drawn to slightly different sizes enabled us to observe the filtering effects of different PBGFs on our fibre laser. The

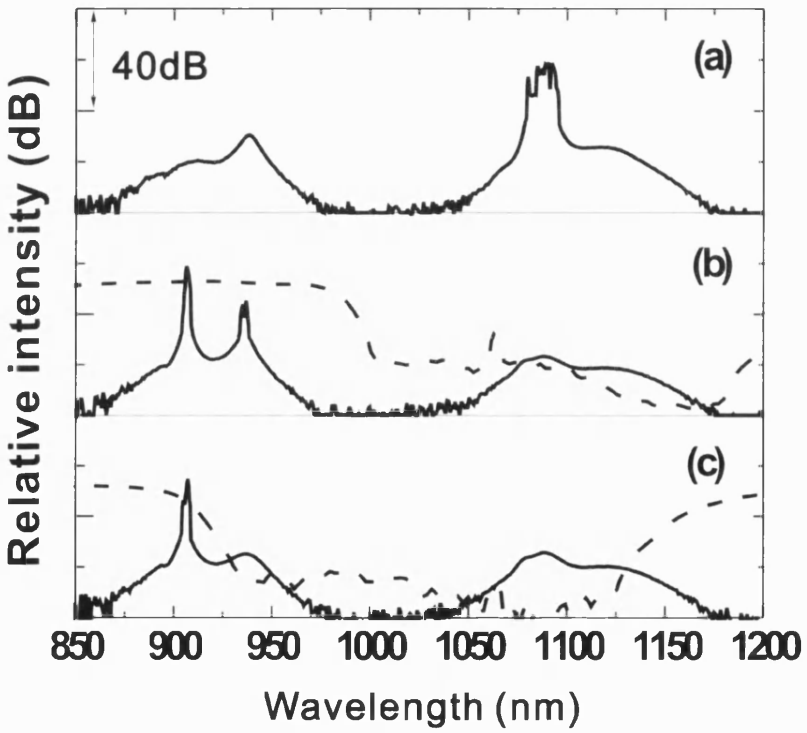

Figure 5.14: (a) Lasing optical spectrum near 1088 nm without PBGFs in the Nd fibre laser cavity. (b) Dual wavelength lasing optical spectrum (solid line) near 907 nm and 936 nm with 50 cm length of spliced 6.8 μm pitch PBGF in the cavity. (c) Changing the PBGF used in (b) for a 50 cm length of 6.3 μm pitch PBGF in the cavity results in the single wavelength lasing near 907 nm shown as the solid line. The transmission spectra of the used PBGFs are presented as the dash lines in (b) and (c), respectively.

Nd fibre length used in these experiments was 3.5 m. Fig. 5.14(a) shows that

without a PBGF in the cavity, lasing occurred around 1088 nm, as expected. By incorporating a fibre with a pitch of 6.8 μm (and 50 cm length) into the laser cavity as shown in Fig. 5.8(C), we found dual-wavelength lasing at 907 nm and 936nm occurred.

This is possible because this PBGF has a transmission window covering the whole three-level transition band of the Nd fibre, as shown in Fig. 5.14(b). By simply exchanging this fibre with the same length of PBGF with a 6.3 μm pitch (which has the second high-transmission band blue-shifted by about 70 nm) we obtained lasing only around 907 nm, as shown in Fig. 5.14(c).

In fact, slightly bending the PBGF with the pitch of 6.8 μm can also achieve a similar function. Slightly bending can introduce extra loss at the bandgap edges (such as 936 nm at the red edge) with less effect at the central region of the bandgap (such as 905 nm), so that the round trip loss of the cavity at 936 nm becomes higher than the gain, without lasing being produced.

For the laser system with a shorter length of Nd^{3+}-doped fibre (such as with the 2.5 m gain fibre as used in Fig. 5.8(C)) we could not obtain lasing at the wavelength of 936 nm whichever PBGF was used. This is due to the stronger competition from 907 nm (the absorption drops quickly beyond 920 nm) and lower overall gain at 936 nm due to the shortened fibre length.

5.5.2 Potential applications for other wavelengths

As well as being useful as a filter to suppress the long wavelength signal, a PBGF can also be used to construct distributed losses at short wavelengths and obtain long wavelength gain. This cannot be realized by the 'W-profile' fibre [96], which relies on a mode being cutoff for longer wavelengths. This function can be demonstrated in the similar laser system as was used for three-level transition oscillation. The scaled transmission spectrum of our PBGF with the pitch of 6 μm is presented in Fig. 5.15. We can see that the three-level 900 nm and four-level 1060 nm transitions (gray region) are all falling into the high-loss transmission bands, while the pump wavelength (808 nm, red line) and $^4F_{3/2} \longrightarrow {}^4F_{13/2}$ 1300 nm transition (blue region) are located in the centres of the low-loss first and second transmission bandgaps, respectively.

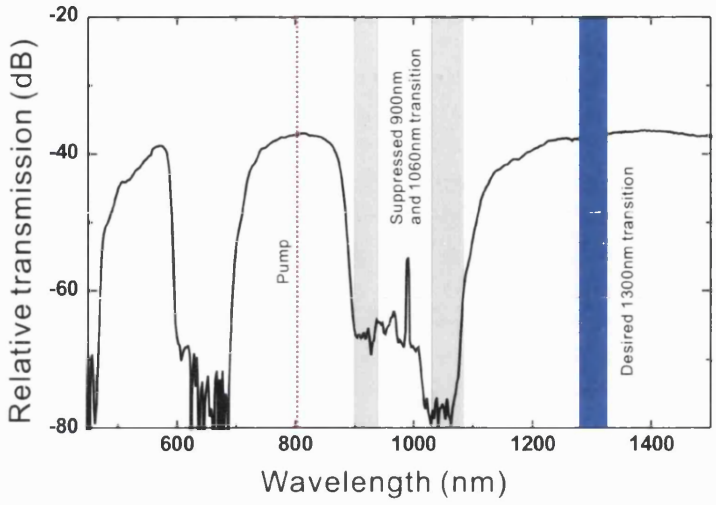

Figure 5.15: Scaled transmission spectrum of our PBGF shows the possibility to suppress the 900 nm and 1060 nm transition and realize Nd fibre laser by 1300 nm transition.

By changing the output mirror M1 to one with high reflectivity at 1300 nm in our laser configuration, the 1300 nm lasing could potentially be obtained. As discussed in Section 5.2.1, excited state absorption (ESA) ($^4F_{3/2} \longrightarrow {}^4G_{7/2}$) can strongly limit the laser transition at 1300 nm, especially in host formed of pure or Ge^{4+}-doped silica glass [92, 99]. Unfortunately, the Nd^{3+} doped fibre we used has a Ge^{4+}-doped core, making the 1300 nm transition impossible. We believe that with a fibre having an Al^{3+} doped silica core material, which has a better balance between gain and ESA at 1300 nm, lasing at 1300 nm incorporating our PBGF with 6 μm pitch would be easily obtained. Notice that during the experiments, slight bending of the PBGF can be used to broaden the high-loss transmission windows if necessary. The desired high transmission wavelengths, all located at the centre of the bandgaps, will not be affected by the bending.

Applications of our PBGF are not only restricted to Nd doped fibre, but can be extended to many frequency selecting optical fibre systems. For example, for the Er doped fibre, the PBGF can be used to modify its gain spectrum to obtain the S-band/L-band or gain flattened Er fibre amplifiers (or lasers).

5.6 Conclusion & future work

5.6.1 Conclusion

In conclusion, we have demonstrated a robust and efficient Neodymium fibre laser configuration incorporating an all-solid bandgap fibre, which was used to suppress the four-level transition and obtain efficient lasing at 907 nm. The laser shows a maximum slope efficiency of 32% and threshold pump power of 70 mw. Further slight improvements are anticipated, which can be realized by improving the splice losses through redesign of the PBGF, and ultimately by incorporating a high gain medium directly into the PBGF. Compared to use of a W-index fibre, the PBGF has a high wavelength discrimination (see Fig. 5.6), and in principle could also be used to suppress gain at shorter wavelengths (for example, to shift lasing to the long-wavelength end of a gain band), which is not possible with the W-type fibre.

5.6.2 Future work

The further work planned is to incorporate the Nd-doped core into an all-solid PBGF directly. The desired gain profile of the Nd-doped core can be artificially modified by designing the bandgap structure of the cladding, quite useful for fibre amplifier design. For a fibre laser, the selection of lasing wavelength can be easily realized just by changing the fibre diameter to shift the bandgap locations to the desired wavelengths. Other rare earth dopants could also be incorporated into the bandgap fibre, such as Yb [100] or Er ions, to realize interesting related applications.

As well as the wavelength discrimination, another novel property of all-solid PBGF is the anomalous GVD, especially at wavelengths below 1.3 μm, which is not possessed by conventional optical fibres. It could be used to provide chromatic dispersion compensation for mode-locked Nd or Yb fibre laser systems working at the wavelength range from 0.9-1.0 μm. The dispersion compensators commonly used in these fibre laser systems are bulky devices, such as grating pairs, suffering from many disadvantages. For example, they can limit the ap-

plicability of fibre lasers and contravene the all-fibre nature. Substituting these bulk devices with all-solid PBGFs can facilitate the alignment operation and decrease the laser volume. In fact, the function of dispersion compensation has been demonstrated in a mode locked Yb fs fibre laser at the wavelength around 1.0 μm [100]. We propose a similar mode-locked laser using a Nd doped fibre working around the wavelength of 0.9 μm. Both the filter and dispersion compensation functions of our all-solid PBGF could be utilised in this fibre laser.

Chapter 6

Bend losses of an all-solid photonic bandgap fibre based on an array of oriented rectangular high-index rods

6.1 Introduction

As well as the technological applications demonstrated in Chapter 5, all-solid PBGFs also present opportunities for further understanding the nature of photonic bandgaps (especially bend loss) in optical fibres. I have designed and fabricated all-solid bandgap fibres with low index contrasts (1% and 2%) , suitable to study their bend losses, and have observed the different bend losses between the even- and odd-numbered bandgaps, contributing to the understanding of bend loss mechanism. This work will be introduced in Section 6.2. It also forms the background to understand the directional bend losses in an all-solid bandgap fibre based on an array of oriented rectangular (line-like) high index inclusions, comprising the rest of this chapter.

Previous research only concentrated on fibres in which the raised-index cladding elements were circular, either rods [47, 66, 67] or rings [69]. As a part of my thesis work, I have fabricated and characterised a new kind of all-solid PBGF with a

different symmetry of high index cladding rods. Near-field patterns of cladding modes clearly identify the cutoff rod modes at the bandgap edges, demonstrating the generality of ARROW (anti-resonant reflecting optical waveguide) guidance in PBGFs [41, 42, 43, 44]. The bend losses in this fibre depend on the bend directions, and can be understood by the directional coupling properties of the different rod modes and the modelled density of cladding states.

6.2 Bend loss mechanism in all-solid PBGF—understanding photonic bandgaps

As discussed in Section 3.1, if a hollow-core PBGF has a structure like Fig. 3.1 with air matrix, it would not be self-supporting, so fine strands of glass are used to form the actual fibre and hold it together. These fine strands quickly destroy the bandgaps by greatly increasing the coupling within the cladding. Furthermore, the high index contrast between air and glass materials of a hollow-core PBGF leads to difficulties in observing bend loss [101], making hollow-core PBGFs unsuitable for studying the bend loss of PBGFs.

However, an all-solid PBGF, whose periodic cladding structure has no strands connecting the high index inclusions, has full bandgaps and rich properties. In particular, the low-index-contrast (1% to 2%) bandgap fibres are ideal for studies of bend loss. The bandgap fibre studied in this work was drawn from the same preform as the fibre presented in Chapter 5, so the detailed bandgap cladding and core structure can be referred to in Fig. 5.4. The pitch Λ of the final fibre has been changed to Λ =15.2 μm.

6.2.1 Bend loss experimental results

By using a fibre-based supercontinuum source, the spectral transmission through 2 m of an all-solid PBGF with Λ =15.2 μm was measured, when held straight or bent in a single turn with a radius of curvature of 15 or 7.5 cm. The resulting transmission spectra, are shown in Fig. 6.1, normalised to the output spectrum of our supercontinuum source.

Five transmission windows are observed for the straight fibre (black curve), corresponding to bandgaps 3 to 7. Using the known parameters of the fibre (referring to Section 5.3.2), they can be readily identified with the photonic bandgaps of the cladding as expected from the ARROW model. From the transmission spectra of our fibre under the bent conditions (red and blue curve), we can see that the odd-numbered bandgaps are relatively resistant to bend loss, whereas the even-numbered bandgaps are much more sensitive, especially on the short-wavelength edge of the bandgap. Note that the 3rd bandgap is least sensitive to bend loss among the measured bandgaps.

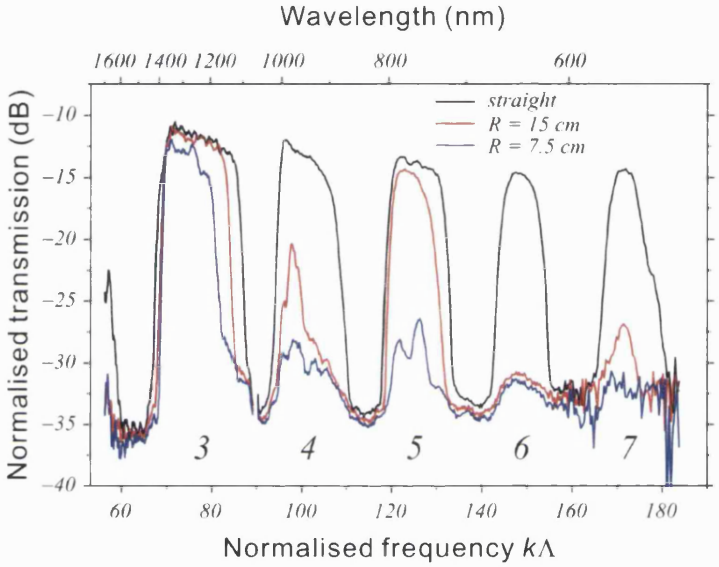

Figure 6.1: Transmission spectra verus the normalised frequency of 2 m of the all-solid PBGF shown in Fig.5.4 with the pitch of 15.2 μm. The black line is the observed transmission in bandgaps 3 to 7 (labelled in this figure) for the straight fibre, while the red and blue lines are the transmission spectra corresponding to the bend radii of 15 cm and 7.5 cm, respectively.

6.2.2 Numerical modelling of band structure

In order to understand the experimental results, numerical modelling was carried out by Dr. G.J. Pearce. The fully-vectorial fixed-frequency plane-wave method described in [102] was used to calculate the photonic density of states (DOS) of an infinitely-periodic triangular lattice of isolated graded-index rods in a low-index

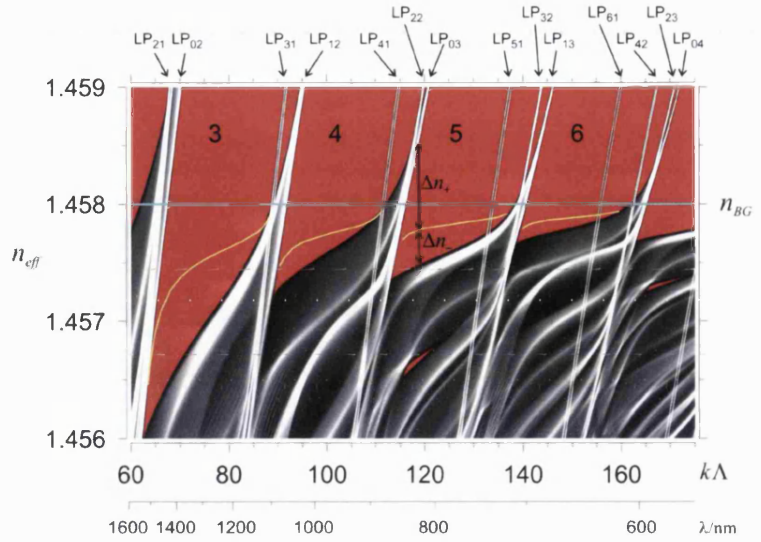

Figure 6.2: Photonic density of states for a triangular array of high-index rods (Δn =2%) of diameter d=0.44Λ in a low-index background of n=1.458. The designations of the scalar rod modes from which the bands evolve are labelled in the form LP_{lm}. Also defined are the downward and upward effective index mismatches Δn_- and Δn_+ between the core line and the bands. Across each bandgap, Δn_- is smaller than Δn_+ except near the long-wavelength edge.

background. In addition, an 8×8 supercell method was used to determine the core line: the dispersion curve of the fundamental bandgap-guided mode in a core defect introduced by the absence of a single rod. The index profiles were chosen to match the experimental fibre described in Section 5.3.2 as closely as possible. The background refractive index n_{BG} was taken to be 1.458, representing undoped fused silica.

The resulting photonic band structure is shown in Fig. 6.2 with normalised frequency $k\Lambda = \omega\Lambda/c$ and effective index $n_{eff} = \beta/k$. Red regions represent bandgaps (zero DOS) and are numbered in order of increasing $k\Lambda$. The grey-scale shading of non-zero DOS (low DOS in black, high DOS in white) highlights the continuity of features within and across bands [103].

The core line (yellow curve) is also shown in the bandgaps, lying close to but below the cutoff line $n_{eff} = n_{BG}$ marking the boundary between states that are propagating and evanescent in the background material. The low-loss windows of the fibre are therefore approximately the frequency ranges between where the

cutoff line crosses the bandgaps. Loss is high between the bandgaps because light in the core can leak through the cladding. The calculated and low-loss windows are coincident with the experimental results shown in Fig. 6.1.

6.2.3 Understanding bend loss

In a straight step-index fibre the guided fundamental core mode has effective index n_{fm}, higher than the refractive index of the cladding, n_{cl}. Bending the fibre effectively skews the index profile so that it rises towards the outside of the bend (see Fig. 6.3) [5, 104]. A radiation caustic therefore appears in the cladding on the outside of the bend, where the index is raised enough to match the difference between n_{fm} and n_{cl}, Δn.

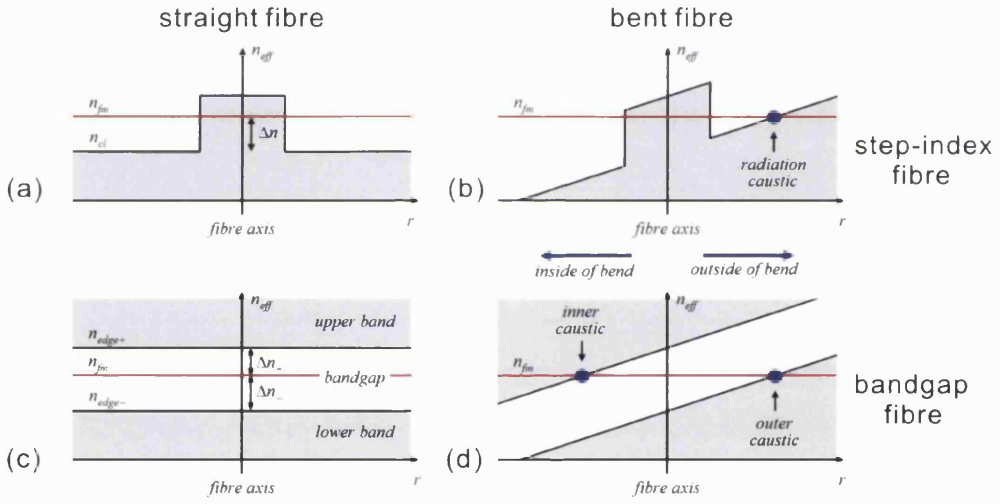

Figure 6.3: Schematic plots of effective index n_{eff} against displacement r from the fibre axis along the radius of curvature. The index n_{fm} of the fundamental core mode is marked in red. Top: a step-index fibre when (a) straight and (b) bent; Bottom: the cladding bands of a bandgap fibre when (c) straight and (d) bent.

The process is similar in bandgap fibres, except that cladding states exist in bands of higher as well as lower index than n_{fm}. Hence there is also a radiation caustic on the inside of the bend (where the upper band's index is lowered enough to match n_{fm}) [105]. Susceptibility to bend loss is still inversely related to the

index mismatch between the core mode and the nearest band; ie the smaller of the downward and upward mismatches Δn_- and Δn_+ as marked on Fig. 6.2. From Fig. 6.2 it is clear that the core line is closer to the band below than the band above over most of each bandgap, so Δn increases monotonously from the blue edge of a low-loss window until very close to the red edge, which is a general property of bandgap fibres. As seen in Fig. 6.1 the transmission window narrows mainly from the blue edge as the fibre is bent [105]. It is also clear that Δn is smaller in even-numbered bandgaps (eg, gaps 4 and 6) compared to odd-numbered bandgaps (eg, gap 3 and 5), because the floor of the bandgap is higher in those windows. Hence the shallower even-numbered windows are more susceptible to bend loss, as found in the experiments described in Section 6.2.1.

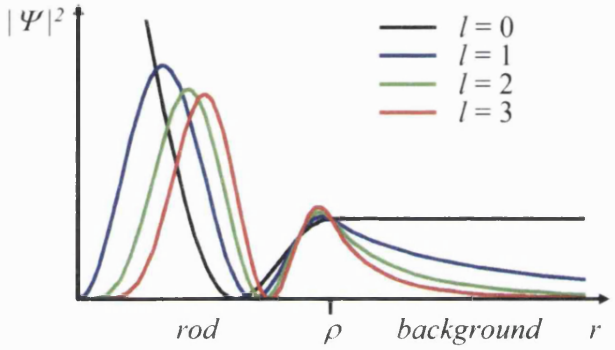

Figure 6.4: Calculated unnormalised intensity distributions $|\Psi|^2$ at cutoff for the first four LP_{l2} modes of a step-index rod with radius ρ, showing the different rates of decay $|\Psi|^2 \sim 1/r^{2l}$ into the background. (The m =2 modes were chosen for this illustration because of their prominence in Fig. 6.2, and also because the LP_{01} mode has no cutoff.

To understand the enhanced susceptibility of the even-order bandgaps to bend loss, the formation of bands by the coupling of cladding rod modes needs to be considered [106]. In fact, the band width is determined by the strength of the overlap between the modes of neighbouring rods, which occurs when the rod modes pass through cutoff and become leaky. The scalar 'weak guidance' approximation [5] can be used for our case due to the low refractive index contrast in our fibres, and the LP_{lm} modes of conventional fibres can express the rod modes with modal fields described by a single scalar function Ψ. The integers l and m respectively describe the azimuthal and radial variations of the field in the rod.

The field distribution above cutoff can be described by the modified Bessel function K_l, which at cutoff becomes $\Psi \sim 1/r^l$. In fact, this decay rate of an isolated step index rod mode determines how strongly the rod modes couple together, which is provided in Fig. 6.4. When l=0, Ψ does not decay at all into the background material, so that these modes quickly couple together strongly to form a broad band of supermodes. When l=1, Ψ does decay into the background material, so the coupling between the rod modes is weaker and the band of supermodes is narrower. This trend continues below cutoff for leaky modes [5]. Thus the floor of a bandgap will be higher if it is determined by coupled l=0 rod modes rather than l=1 rod modes. Since the cutoffs of l=0 and l=1 modes alternate with increasing frequency, bend loss in odd- and even-numbered bandgaps is determined by l=1 and l=0 bands respectively. Hence even-numbered bandgaps are more susceptible to bend loss than odd-numbered bandgaps. The coupled rod modes with l>1 can be neglected, because their fields decay into the cladding so strongly that they have non-zero power in the core even at cutoff [5], making them particularly weakly coupled [106]. They can retain their identity and form straight narrow bands in Fig. 6.2 that persist well below cutoff.

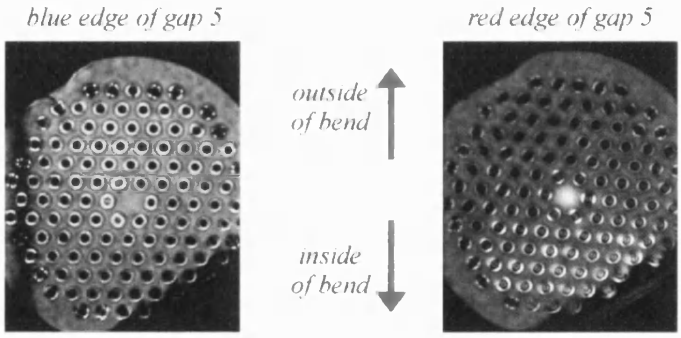

Figure 6.5: Light patterns across the fibre after bending, for wavelengths near the blue (left) and red (right) edges of gap 5. The top of each image is towards the outside of the bend. Near the red edge of the bandgap, bend loss is towards the inside of the bend.

As discussed above, we have predicted that the overall distribution of light coupled to the cladding by bending shifts from the outside of the bend at the blue edge of a bandgap to the inside of the bend at the red edge. This is demonstrated by our experimental result, shown in Fig. 6.5. The figure shows the overall distribution of power within the cladding following bend loss. The images were recorded at wavelengths at both edges of bandgap 5 centred at 770 nm. The bend radius was 20 cm and the images were acquired immediately after the bend.

We have shown how the azimuthal order of a rod mode influences the depth of the bandgap whose blue edge it defines, and hence the effective index mismatch Δn between the core mode and the nearest cladding state. The losses are especially high when the bandgaps are defined on their high-frequency edge by an LP_{lm} mode with low azimuthal order l. This new understanding of bandgaps directly led to an improved design of such fibres, in which the low-l modes were intended to be suppressed to reduce their bend sensitivity. This work has been demonstrated in our group [69] by using a 2-d array of tubular high-index regions (which appear as rings in the fibre cross-section) rather than rods in the cladding.

Different from these all-solid PBGFs focused on circular raised-index inclusions (rod or ring) in the bandgap cladding, a new kind of all-solid rectangular-rod bandgap fibre has been fabricated. A fibre with such different symmetry is expected to have directional bend loss and is introduced in the following section.

6.3 All-solid PBGF based on an array of oriented rectangular high-index rods

6.3.1 Fabrication

The cladding of our all-silica fibre comprises an arrangement of isolated high index aligned rectangular rods in a lower-index background. To fabricate this kind of fibre, firstly a Ge-doped step-index silica rod (comprising a central doped region surrounded by an undoped cladding; the index difference was 2.03% and the core-to-cladding diameter ratio was 0.88) and a pure silica rod were drawn to canes with an outer diameter of 0.83 mm. They were then stacked together (see Fig.6.6). Three layers of Ge-doped canes were located in the middle of this stack, which was otherwise formed from pure silica canes. The whole structure was then drawn to canes of 0.98 mm outer diameter, containing one rectangular inclusion, illustrated in Fig. 6.7(a). The aspect ratio for the raised-index rectangle was designed to be 7:1.

In forming the stack for the final fibre from the canes we paid special attention to the orientation of each cladding rod, to ensure that they were all approximately

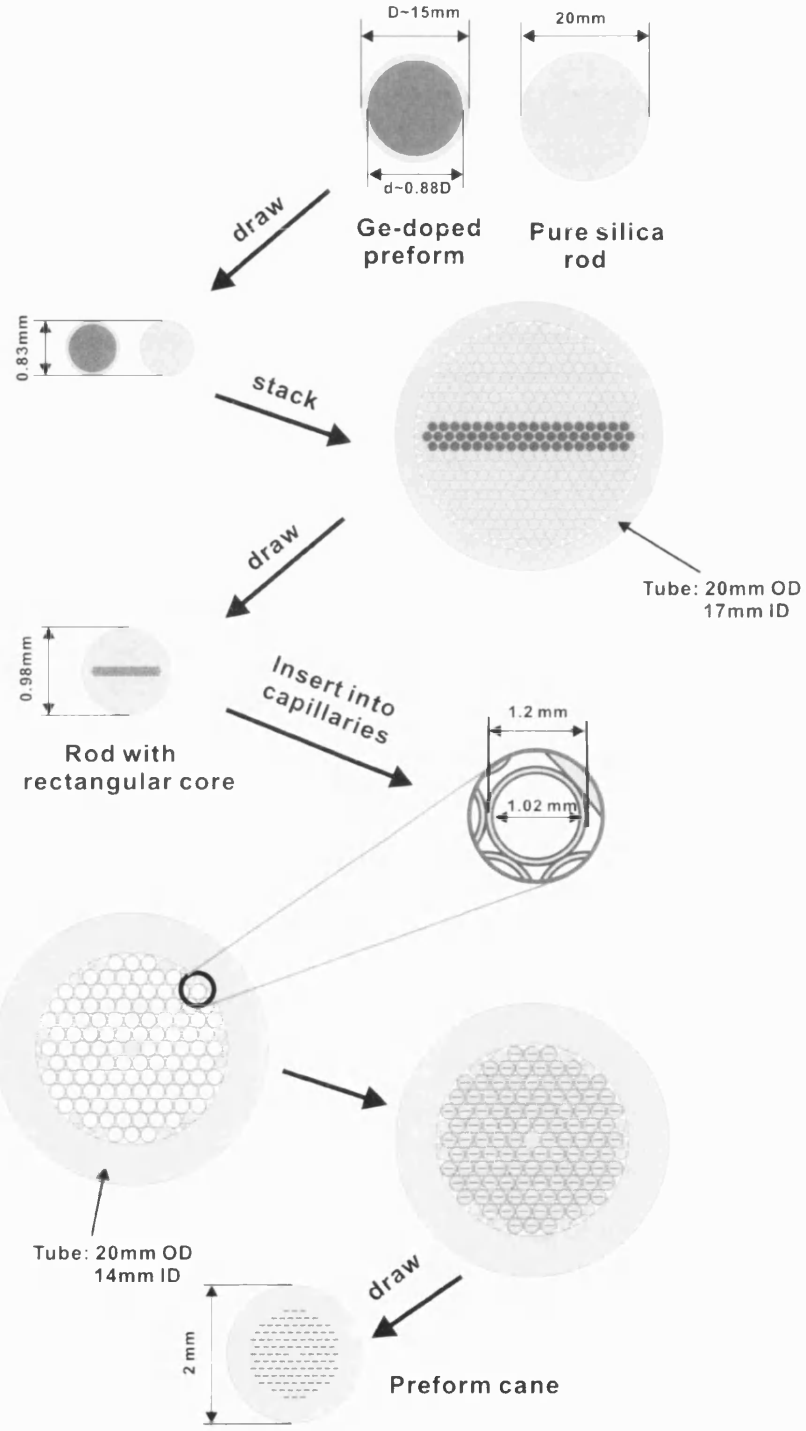

Figure 6.6: Fabrication process for an all-solid PBGF based on an array of orientated rectangular high index rods.

parallel in the final fibre. We first stacked thin-wall capillaries (inner-to-outer diameter ratio: 0.85) with 1.02 mm inner diameter (just slightly larger than the canes with rectangular cores) in the desired array. We then inserted a rectangular cored cane into each capillary, rotating the cane to obtain the correct core orientation. By drawing the stack down with an additional jacketing tube we obtained final preforms with 2 mm outer diameter, which were then drawn to fibres with several different diameters. The whole fabrication process is schematically presented in Fig. 6.6.

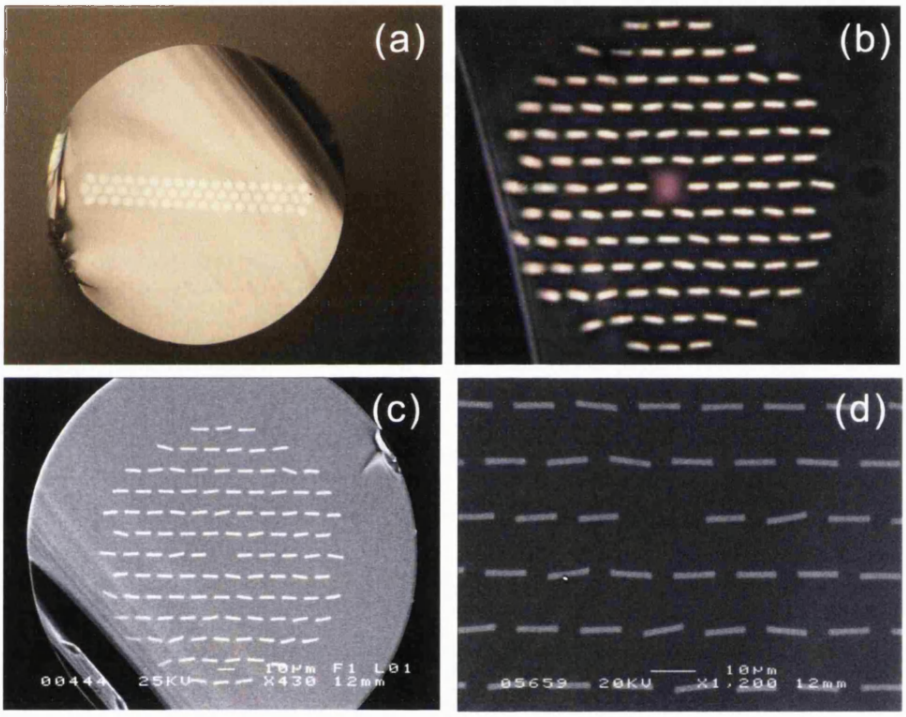

Figure 6.7: (a) Optical micrograph of a cane with a rectangular inclusion made from an array of raised-index rods; (b) Optical micrograph of a fibre with pitch of 8.5 μm; (c) scanning electron micrograph of the final fibre with pitch of 13.8 μm; (d) close-up of the core region in (c), rod pitch: 13.8 μm, length (D)/width (W): 7/1, D/Λ =0.67.

Note that during the preform pulling process, we found that the canes were twisted: the orientation of rectangular rods in one end had an obvious angle with that at the other end (over a meter-long preform). Such twisting cannot be easily identified when drawing other fibres with circular-symmetric geometry. Carefully alignment of cane puller was carried out to obtain the negligible twist

in the fabrication process and for the final fibre.

Fig. 6.7(a) shows a cane with a rectangular inclusion composed of an array of raised-index rods, which was used in the stack of the final fibre. An optical micrograph of a final fibre with a pitch of approximately 8.5 μm is displayed in Fig. 6.7(b). According to the electron microscope images (c) and (d) (the close-up of the core region in (c)), the final ratio of the length of each rectangle to the pitch, D/Λ, was measured to be 0.67. Fibre with a pitch of 13.8 μm (illustrated in Fig. 6.7(c) and (d)) was measured to have an outer diameter of 245 μm.

6.3.2 Numerical modelling of band structure

The photonic density of states (DOS) of a perfectly periodic triangular lattice of isolated parallel high-index rectangular inclusions (n_H=1.47288) in a low-index pure silica background (n_L=1.457) was calculated by Dr. G.J. Pearce and is displayed in Fig. 6.8. The refractive indices and dimensions chosen for the modelling matched those of the experimental fibre in Fig. 6.7 as closely as possible. The resulting photonic band structure was mapped as a function of frequency ω and propagation constant β, represented in Fig. 6.8 by normalized frequency $k\Lambda = \omega\Lambda/c$ and $(\beta - nk)\Lambda$. The first 6 bandgaps are displayed in Fig. 6.8.

The bands arise from the waveguide modes of the high-index rods. These are designated E_{mn}, where m and n are the numbers of intensity peaks along and across the rods respectively [107, 108]. The rod modes E_{11}, E_{21}...E_{71} and E_{12} are labelled in Fig. 6.8, and define the edges of the first 6 bandgaps.

We see that the E_{12} mode is shifted towards higher frequencies and lies close to the E_{71} mode. This is due to the high ratio of the rod's length to its width. Compared with the other rod modes, the E_{12} mode has a flattened dispersion curve and passes through almost all the bandgaps defined by the modes from E_{11} to E_{71}. This in turn affects the vertical depth of each bandgap. Overall, the higher order bandgaps are affected more profoundly by the E_{12} mode and are shallower: the cutoff E_{12} mode has no overlap with E_{11} mode, while the depth of the 6th bandgap is completely determined by the E_{12} mode.

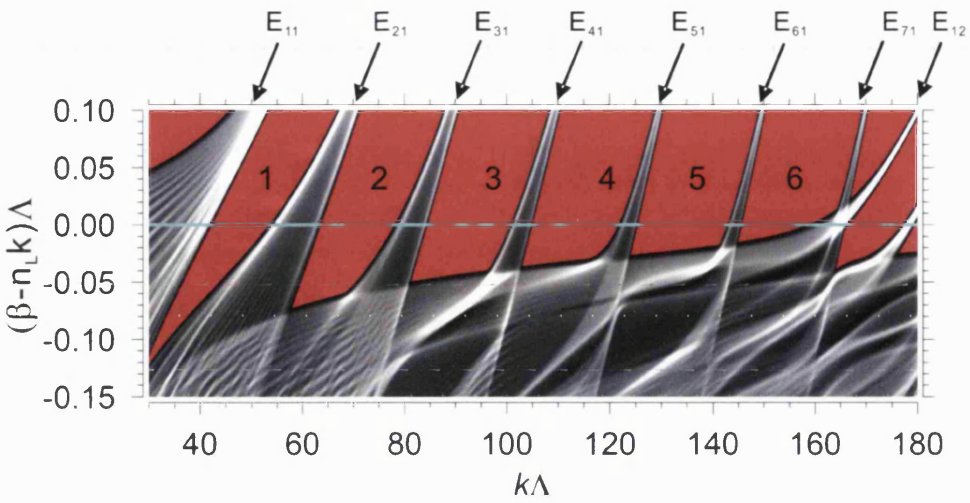

Figure 6.8: Calculated DOS for a triangular lattice of step-index rectangular rods in a low-index background as described in Section 6.3.1. The geometry of the rectangular rods and lattices were chosen to be as close as the fibre displayed in Fig.6.7.

6.3.3 Linear properties

Transmission spectrum

We measured the spectral transmission through a length of about 25 cm of fibres with pitches of 14.1 μm and 11.3 μm, presented in Fig. 6.9 as red and black curves. The transmission spectra for these two fibres with different pitches can display the whole first 6 bandgaps together in the visible and near-infrared wavelength region. The spectral transmission of the bandgap fibre was measured by butt coupling an endlessly single-mode PCF at each end (see Fig. 6.9(a)). A fibre-based supercontinuum source was then coupled into our bandgap fibre from one PCF, and the transmitted spectrum was recorded from the other PCF by using an optical spectrum analyzer (OSA). The alignment of these three fibres was adjusted to maximize the power in the core, as monitored by the OSA. The fibre was kept straight during the measurement.

We see in Fig. 6.9 that there are a series of low-loss transmission windows corresponding to light being guided in the core. This was confirmed by imaging the near field pattern at the bandgap fibre's output end and using bandpass filters.

By measuring these two fibres with slightly different values of pitch, we observed the first 6 low-loss transmission bands from 450nm to 1750nm, which were in good agreement with the modelling results for the cladding bandgaps shown in Fig. 6.8.

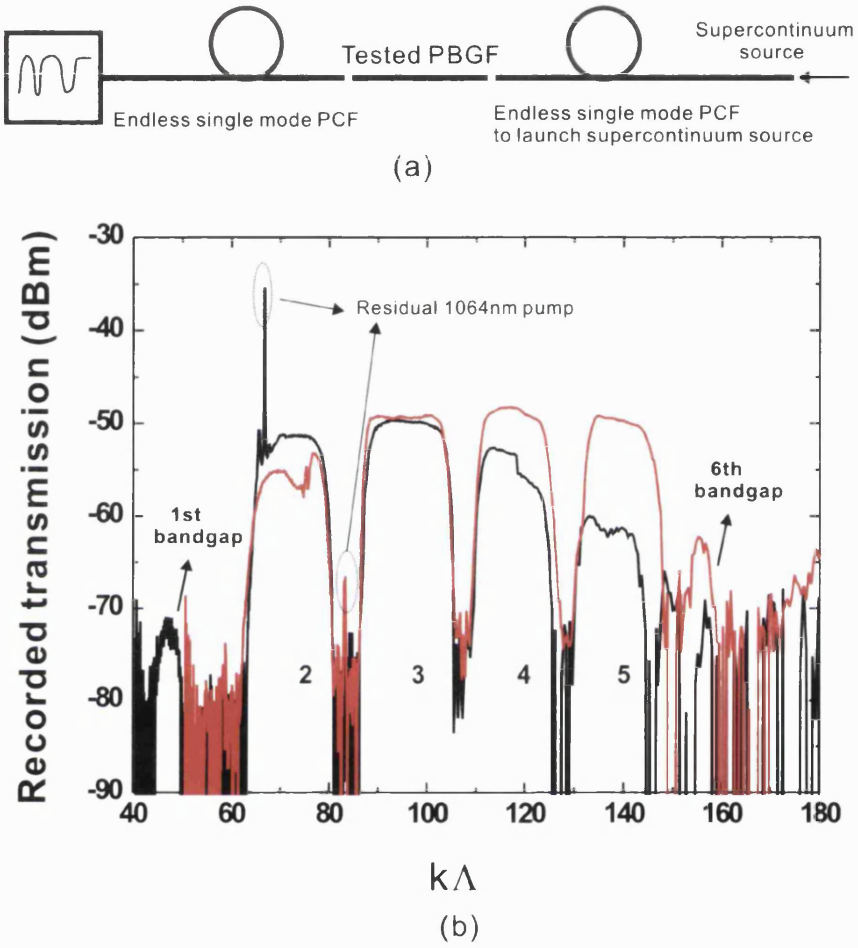

Figure 6.9: (a) Setup to measure the transmission spectrum of our PBGF. (b) Recorded transmission spectra by OSA through the setup in (a). The red and black lines correspond to the fibres with the pitches of 14.1 μm and 11.3 μm, respectively. The peaks in the transmission spectra are the residual microchip 1064 nm pump laser for the supercontinumm generation.

The first bandgap (which is comparatively narrow) and sixth bandgap (which is shallow) have higher loss than the middle four. The intrinsic transmission loss of the bandgap fibre with the pitch of 13.8 μm was measured to be 0.2 dB/m at the wavelength of 1220 nm (centre of the second bandgap) by the cut-back method.

The order of the observed bandgaps from 1 to 6 are marked in Fig. 6.9(b). This fibre is not expected to have large birefringence, because of its large core size and small refractive index contrast.

Near field patterns

The near-field patterns at the fibre's output face were measured by imaging onto a CCD camera with appropriate magnification, shown in Fig. 6.10. A scanning monochromator with a 3 nm pass-band was located between the supercontinuum source and the input PCF. The end of the input PCF was then butted up against the bandgap fibre. After optimizing the alignment to couple the spectrally filtered light into the bandgap fibre core, a series of near-field images were recorded, as displayed in Fig. 6.11.

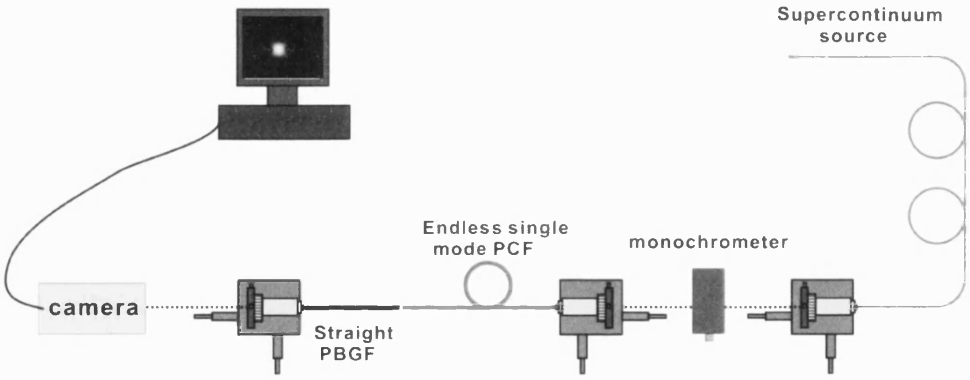

Figure 6.10: Experimental setup to measure the near field patterns of bandgap fibres.

As the dotted arrows show, the top four near-field images from A to D correspond to the middle positions of four low-loss transmission ranges (ie, bandgaps) from 3 to 6, while the bottom four (images A' to D') correspond to the high-loss band edges. In these band edge images, the light patterns in the cladding rods clearly show the rod modes E_{41}, E_{51}, E_{61} and E_{12} respectively at their cutoff wavelengths. By similarly observing the near-field patterns in the lower bands (from 1 to 3) through a 125 μm outer diameter fibre (7 μm pitch), E_{11}, E_{21} and E_{31} mode patterns were also identified clearly at the corresponding band edges. Due to the large 7:1 aspect ratio of the rectangular rod, the E_{12} mode is strongly shifted in frequency, having a higher cut-off frequency than the E_{61} mode. This means the wavelengths of the first 5 bandgaps at the low-index line are completely

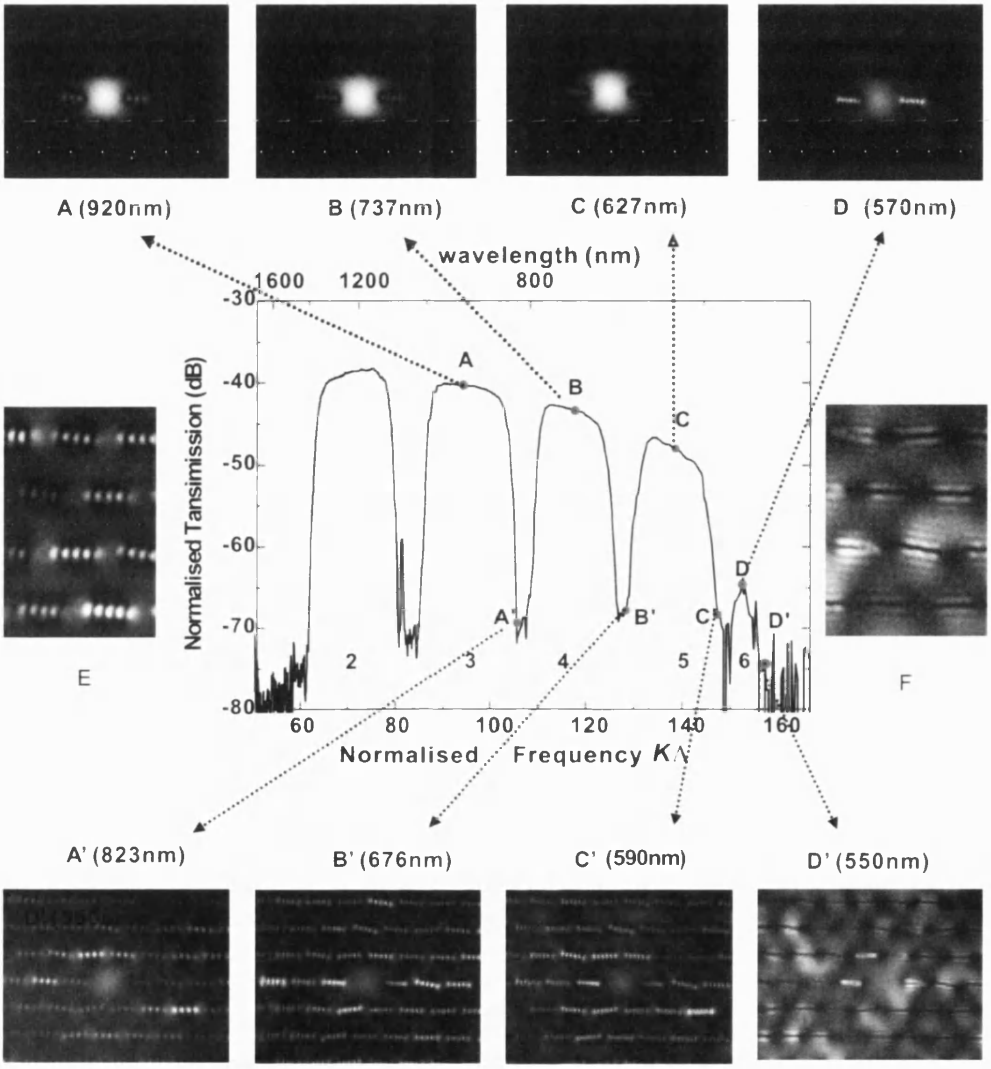

Figure 6.11: Transmission spectrum of the bandgap fibre with the pitch of 13.8 μm as a function of normalized frequency (kΛ) and wavelength in central diagram. The top 4 pictures A, B, C and D show the near field patterns in the middle of bandgaps 3 to 6, respectively. The bottom four A', B', C', and D' present the near field patterns at the corresponding bandgap edges. Images E and F are enlarged images of the cladding region in images B' and D' respectively.

determined by the modes E_{11} to E_{61} in order.

From the near field image E (a close-up of image B'), we can see that the coupling of the neighbouring cladding rods (E_{51} mode in image E and B') is stronger between rods in the same layer than it is between rods in adjacent layers. The rod layer is defined according to the 'horizontal' direction in Fig. 6.7 and Fig. 6.11. This coupling property is also found for modes E_{21}, E_{31}, E_{41} and E_{61}, by observing their corresponding near field images.

By scanning the wavelength from the centre of each of the bandgaps 2-5 (corresponding to the cutoffs of E_{21} to E_{61}) to the edge, we observed that the light in the core tends to leak in the 'horizontal' direction much more quickly than in the 'vertical' direction.

To check this observation, the near field patterns at wavelengths of 795 nm, 800 nm, 802 nm and 805 nm located on the red edge of the 4th bandgap were recorded (see the left column of Fig. 6.12). The cladding rod mode E_{41} can be clearly seen in these images. The pixels values in each row were summed along the x direction to give a value of the summed intensity. This was carried out for each value of y. Likewise the pixel values in each column were summed to give a value for the summed intensity in the x direction. (red curve: x axis of the near field image with summation of intensity in the y direction. Black curve: y axis of the near field image with summation of intensity in the x direction.)

We can clearly see that along the vertical direction (black curve) there is always an obvious intensity distribution with the maximum located in the central layer of rods, but along the horizontal direction (red curve) the intensity distribution becomes flattened. Some kind of confinement in the cladding rod layers along the vertical direction suggests weak coupling of the rod modes between different layers, and the flattened intensity distribution along the horizontal direction demonstrates strong coupling between neighbouring rod modes in the same layer. Certainly, the further the wavelength is from the bandgap centre, the flatter the intensity distribution for both directions (both red and black lines), referred to Fig. 6.12.

Note that near field image D' (displaying E_{12} mode) is obviously different from the other three band edge images: coupling of the adjacent rod modes does not

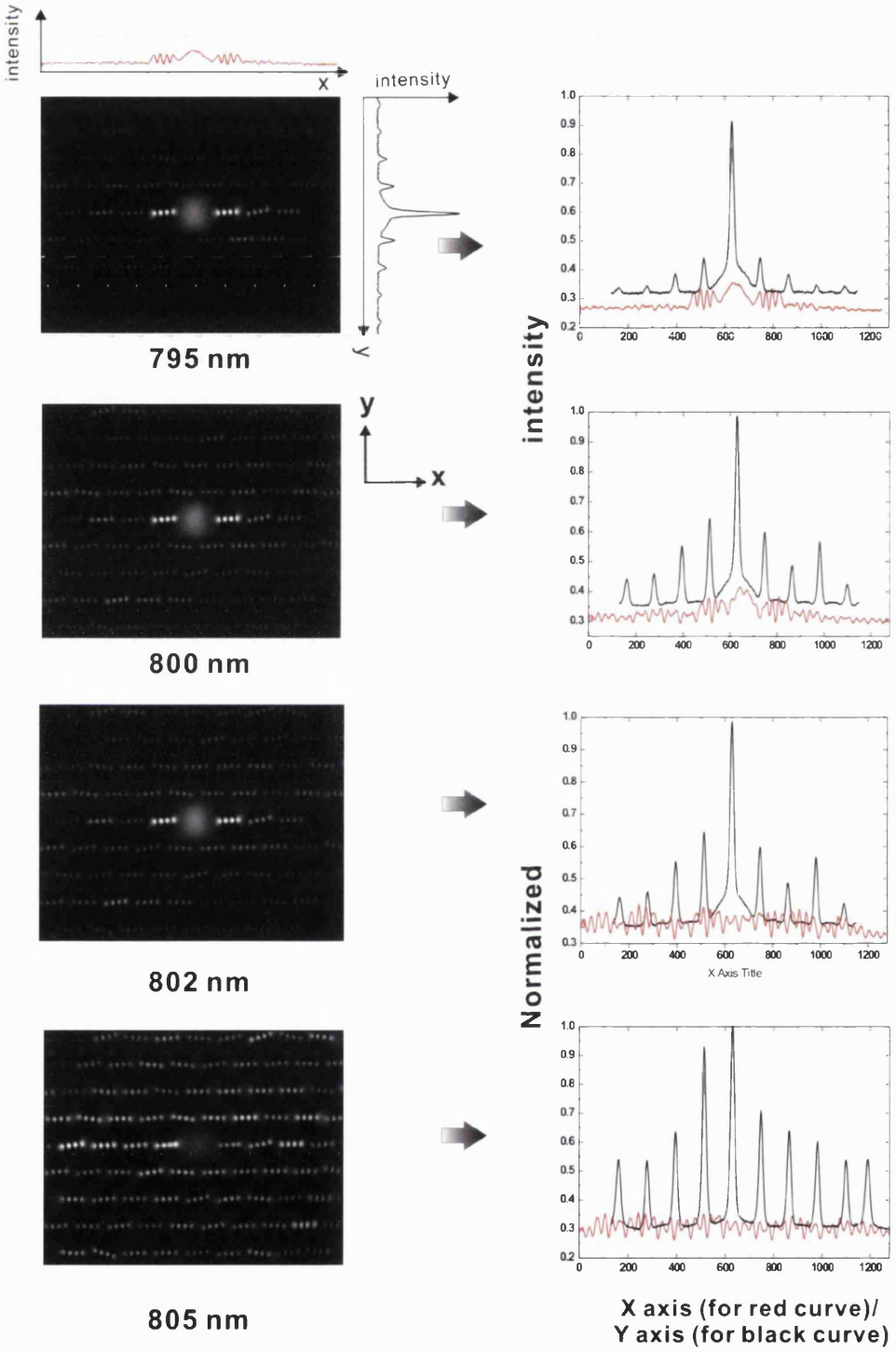

Figure 6.12: (left) Near field patterns at the wavelengths of 795 nm, 800 nm, 802 nm and 805 nm located on the blue edge of the 4th bandgaps; (right) the intensity distributions in the corresponding near field images along horizontal direction (x axis, red line) and vertical direction (y axis, black line).

occur in the same layer but between the neighbouring layers; the regions located between the neighbouring rods in the same layer become dark, instead of being bright in images A', B' and C'. This is particularly clear in image F, the close-up of image D'.

6.3.4 Directional bend loss measurement

The directional dependence of bend loss in this fibre was measured by bending the fibre in two planes, one in the plane of the rectangular rods in the cladding and the other perpendicular to this plane. The experimental setup is presented in Fig. 6.13.

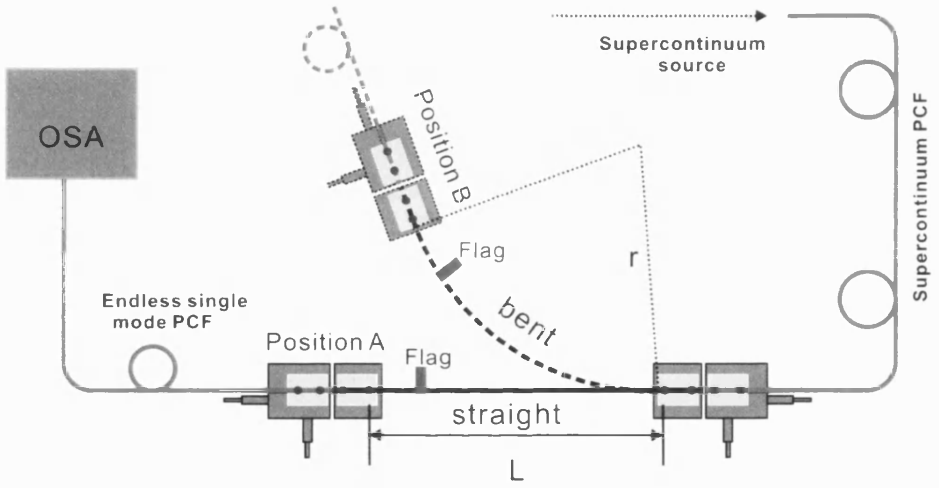

Figure 6.13: Experimental setup to measure the directional bend losses of our bandgap fibre. A flag was attached to the fibre to indicate the rod orientation during the experiments.

The bend radius r used was 8 cm and the bent length was 8 cm, the remainder of the fibre being held straight. One end of the fibre was butted against an endlessly single mode PCF coupled to the supercontinuum source. By checking the near field image at the output end, we rotated the fibre to an angle at which the cladding rods were horizontal and a horizontal flag attached as a reference of the rod orientation. Another piece of endlessly single mode fibre was then butted up against the output end with the alignment adjusted to maximize the power in the core. An OSA was then used to record the spectrum when the fibre was

straight and bent. The bend loss measurement for the vertical orientation was carried out in a similar way. The bent length and bend radius were kept identical for the two measurements.

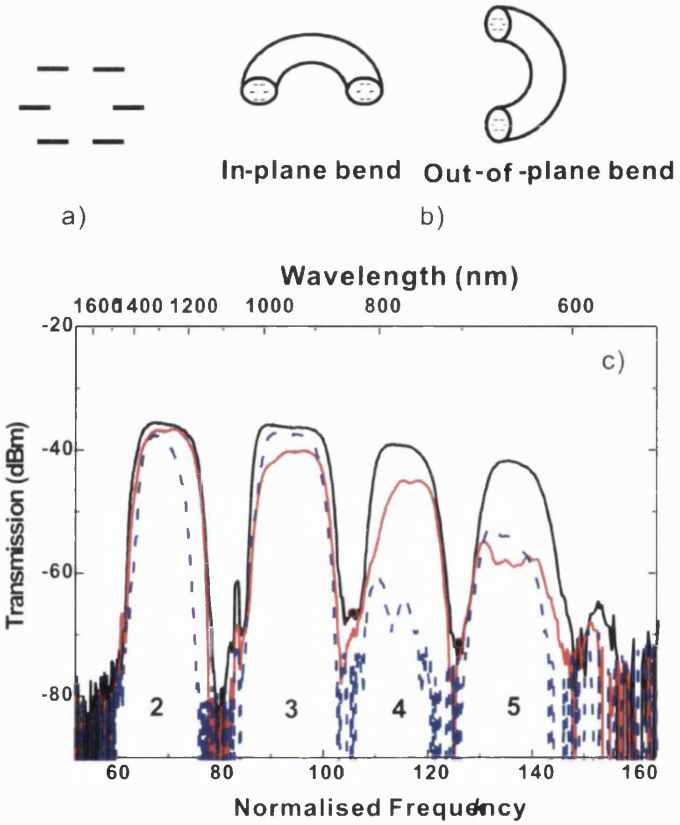

Figure 6.14: Directional bend losses. a) the orientation of the cladding rods; b) the fibre bent in-plane and out-of-plane; c) transmission spectra through 30 cm of fibre for different bend directions. The length of bent region in this fibre was about 8 cm with the bend radius of 8 cm. The fibre was straight (black solid line), bent out-of-plane (red solid line) and bent in-plane (blue dashed line).

Fig. 6.14 shows that the susceptibility of the fibre to bend loss varies across bandgaps 2-5, and is also dependent on the direction of bending. The difference in bend loss in the two bending directions is especially great for bandgaps 2 and 4, with in-plane (rods orientated in the same plane as the bend) bending giving the greatest loss. Conversely, in bandgaps 3 and 5 there is a smaller difference between the two bending directions, and out-of-plane (rods orientated perpendicular to the bend) bending gives the greater loss. These differences become more obvious for bandgaps 2 and 3, when we bend the fiber with smaller diameter than that

shown in Fig. 6.14.

In Section 6.2, it was shown that the bend loss of a bandgap-guiding PCF structure can be understood in terms of the cladding band structure by considering the 'depth' of bandgaps, i.e. the offset between the fundamental guided mode and the nearest band edge. If the offset is small, the fibre is more susceptible to bend loss than when it is large. The different behaviour of the bandgaps in the fibre described here can also be understood by reference to the DOS plot in Fig. 6.8.

Fig. 6.14 shows that bandgap 2 is the most resilient to bend loss, and that bend loss susceptibility increases with frequency (and hence bandgap number). This can be explained by the shape of the DOS plot in Fig. 6.8: the depth of each bandgap decreases as frequency increases, largely as a result of the dispersion of the E_{12} mode, and it is therefore expected that the susceptibility to bend loss also increases with frequency. In order to understand the directional dependence of bend loss, it is necessary to consider the different bandgaps in detail.

Consider first bandgaps 3 and 5. The E_{41} and E_{61} modes define the high-frequency edges of these bandgaps, but these modes broaden relatively slowly below cutoff. As a result, the floors of the bandgaps are defined over much of their width by the E_{12} mode. As shown in Section 6.3.3, the E_{12} mode is most strongly coupled between adjacent rods in the out-of-plane direction, and therefore we can expect these bandgaps to be more sensitive to out-of-plane bending than to in-plane bending.

Bandgaps 2 and 4 are defined at their high-frequency edges by the E_{31} and E_{51} modes. These modes broaden more quickly below cutoff than the E_{41} and E_{61} modes. The floor of bandgap 2 is consequently defined by the E_{31} mode over much of the bandgap width at the cutoff line; the E_{12} and E_{51} modes are all found to appear close to the floor of bandgap 4 at the low-frequency part, while the high-frequency part of the bandgap 4 is completely determined by the E_{51} mode. Because E_{31} and E_{51} are both strongly coupled between adjacent rods in the in-plane direction, we expect bandgaps 2 and 4 to be particularly susceptible to in-plane bending, and especially so at their high-frequency edges. The increased susceptibility of the high-frequency edges of bandgaps 2 and 4 to in-plane bending is particularly evident in Fig.6.14.

6.4 Conclusion & future work

6.4.1 Conclusion

The general explanation of the bend loss mechanism of bandgap fibres helps us to understand the bandgap properties of any bandgap fibres, including hollow-core PBGFs, and guided us to improve the design of such fibres. It has directly resulted in an all-solid PBGF based on an array of raised-index ring rods to improve resistance to bend loss [69]. In this ring fibre low-l modes, which dominate the high bend loss bandgaps, were eliminated by replacing high-index rods with thin high-index rings.

In this chapter, another new kind of all-solid photonic bandgap fibre based on an array of oriented rectangular rods was introduced and a series of low-loss transmission bands were measured. From the near-field patterns of modes at the band edges, the rod modes defining their corresponding bandgaps were easily identified, coinciding with the numerical modelling of cladding band structures. Directional dependence of bend losses in this fibre, relative to the orientation of the rectangular rods, was measured. The detailed directional bend loss properties for each bandgap were explained according to the density of states of the cladding and the directional coupling properties of different cladding rod modes.

6.4.2 Future work - Photonic bandgap engineering

Bandgap engineering has been demonstrated in an all-solid PBGF based on a 2-d array of raised-index cladding rings by re-ordering the cladding modes in such a way as to broaden the photonic band gaps and reduce bend sensitivity. Further engineering of the bandgaps can be obtained through breaking the ring structure into periodic high-index blobs. Corresponding to the numbers of the blobs, some specific bandgaps can be further broadened, whilst some other bandgaps can be narrowed forming broad high loss transmission bands. Broad bandgaps have potential applications in light transmission systems and the broad high loss bands could be used to suppress the undesirable noise components in high-power optical amplifiers or delivery systems, where the amplified noises waste pump power and

can potentially overwhelm the desired signals. They could also provide greater freedom for PBGF design, when using a PBGF as an in-line fibre filter (like the work in Chapter 5) or incorporating a rare earth doped core into the PBGF to adjust the gain profile.

Some preliminary results of photonic density of states (DOS) of PBGFs based on arrays of rods with 6 high-index blobs have been calculated and are displayed in Fig. 6.15 with normalised frequency $k\Lambda = \omega\Lambda/c$ and effective index $n_{eff} = \beta/k$. For these calculations we assume an infinitely-periodic triangular lattice of high-index inclusions ($n_H = 1.48614$) in a background matrix of lower refractive index ($n_L = 1.457$), where the chosen refractive indices and structure dimensions match the glass materials we have and the possible cladding structures which can be fabricated using the stack and draw method, respectively. The pitch (Λ), diameter of the circle passing through the centres of six blobs (d), and the diameter of each blob (D) are all defined in Fig. 6.15. For these DOS figures, the ratio of d/Λ is fixed at 0.534, and D/Λ varies with discrete values of 0.19, 0.17, 0.15 and 0.13.

When we change the ring structure in the cladding to 6 blobs whose diameter is the same as the ring thickness, as described in Fig. 6.15, the cladding rod modes LP_{lm} (based on the whole unit cell) with $l \neq 3$ can be swept away to higher frequencies. The LP_{3m} mode will be affected much less. As shown in Fig. 6.15(a), the first three bandgaps formed in an PBGF with ring rods [69] in the cladding become narrower due to the blue-shifted LP_{01}, LP_{11}, LP_{21} modes and the bandgap whose blue edge is defined by LP_{31} is broadened. In fact, these four modes can be considered as the LP_{01} family of the structure supermodes. From this point of view, the first broad bandgap is defined by the LP_{01} and LP_{11} family of supermodes, and the second broad bandgap will be defined by LP_{11} and LP_{21}/LP_{02} family of supermodes. These supermodes form the broad bands in this PBGF, corresponding to the broad high loss transmission windows. As the diameter of the blobs decreases from Fig. 6.15(a)-(d), the first bandgap defined by LP_{01} and LP_{11} family of supermodes becomes broader, and the band corresponding to LP_{11} family of supermode becomes narrower. This is because the coupling between these six blobs becomes weaker due to their decreased diameter. Based on these modelling results, the fabrication of such a fibre is proposed to be carried out in the near future.

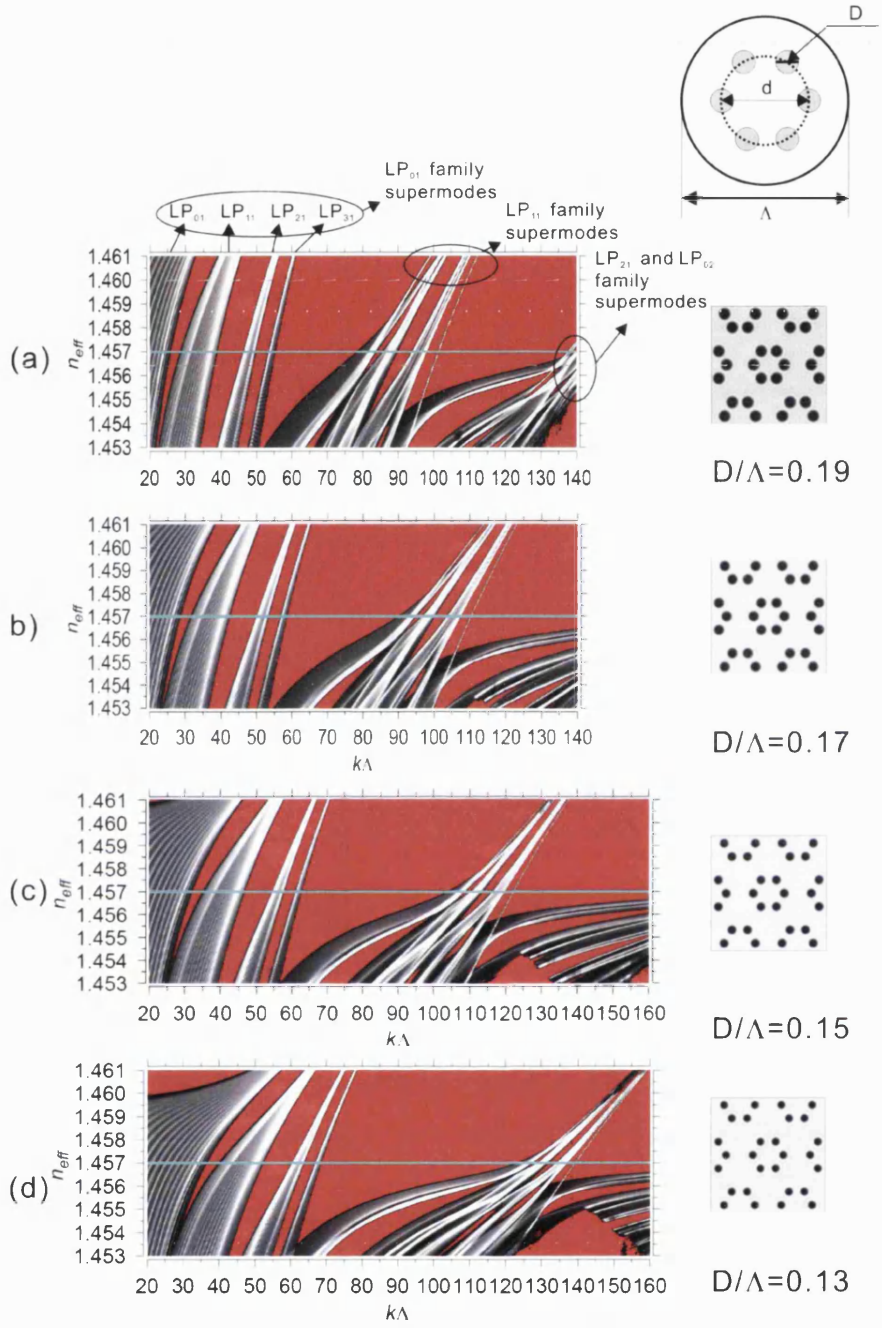

Figure 6.15: Photonic DOS for a triangular lattice of high-index inclusions (n = 2%) in a low index background (n = 1.457, representing undoped silica). Each high-index inclusion is composed of six high-index blobs shown in this figure. Specific guided modes occurring above the blue line are identified at the top of (a). The vertical axis is effective index $n_{eff} = \beta/k$; the horizontal axis is normalized frequency $k\Lambda = \omega\Lambda/c$. The ratio of d/Λ is fixed at 0.534, and D/Λ varies with discrete values of 0.19, 0.17, 0.15 and 0.13, corresponding to the DOS figures from (a)-(d).

Chapter 7

Extruded highly nonlinear PCF formed from tellurite glass for mid-infrared supercontinuum generation

7.1 Introduction

Since the first PCF was demonstrated in 1996, most PCF preforms have been made by the stack and draw process using commercially available silica tubes and rods. An alternative fabrication technology for forming PCF preforms is extrusion [51, 52, 53, 54]. During the course of this thesis, a simple forward extrusion process has been developed for soft glasses by myself and others. Tellurite glasses are good candidates for applications in areas of optoelectronics, laser technology and fibre optics, due to their excellent optical properties (introduced in Section 7.2.1). Conventional tellurite fibres have already been produced and have been used in a number of interesting device demonstrations including broadband amplification from 1535 to 1610 nm in an Er-doped fibre amplifier [109], and from 1490 to 1650 nm in a fibre Raman amplifier [110]. These results highlight the usefulness and practicality of the tellurite glass system.

Supercontinuum generation in silica glass is limited in the mid-infrared region

(beyond 2.1 μm) due to its intrinsic absorption. The useful properties of tellurite glasses not possessed by silica (such as high nonlinearity and good infrared transmittance) make tellurite-glass-based fibres good candidates for mid-infrared supercontinuum generation. To realize this application, a small-core tellurite PCF with tailored confinement and dispersion properties can be used. The light can be tightly confined in the small core, increasing the nonlinear coefficient and enabling efficient broadband supercontinuum generation. The dispersion profile of tellurite PCF can be modified by controlling the core size to generate continuum by pumping with a femtosecond mode-locked Er-doped fibre laser (around 1550 nm). This continuum can be expected to extend into the mid-infrared region (beyond 3 μm). All the work in this chapter is based on this idea.

A tellurite glass was first fabricated and characterised. The fabricated glass was then extruded into preforms and tubes, which were used to fabricate a highly nonlinear solid-core tellurite PCF with zero dispersion wavelength of 1.4 μm. As a suitable Er fibre laser was not available in our laboratories, similar femtosecond pulses from an optical parametric amplifier (OPA) were used as the pump to generate mid-infrared supercontinuum, which extended to 2.8 μm at the long wavelength edge.

7.2 Tellurite based glass materials

7.2.1 Comparison of tellurite glass to other glasses

Supercontinuum generation at mid-IR wavelengths requires the use of a highly nonlinear optical medium with high mid-IR transparency. Extending current PCF technology developed from silica based work at visible and near-IR wavelength to mid-IR wavelengths ($> 2\mu$m) necessitates understanding of the relationship between the glass composition and the optical properties, such as the position of the multiphonon absorption edge and nonlinear refractive index, etc, in order to select a suitable glass for the fibers [111]. The absorption of a solid in the long wavelength limit is known as the multiphonon or IR absorption edge and arises from inner molecule or lattice vibrations. A simple Hookes law mass on spring model predicts that the multiphonon absorption edge will shift towards

Properties	**Tellurite**	**Silica**	**Fluoride** (ZBLAN)	**Chaleogenide** (AsS)
Refractive index (n)	1.8-2.3	1.46	1.5	2.44
Nonlinear refractive index n_2 (m^2/W)	25×10^{-20}	10^{-20}	3.3×10^{-20}	200×10^{-20}
Transmission range (μm)	0.4-5.0	0.2-2.5	0.2-7.0	0.8-16
Highest phonon energy (cm^{-1})	800	1000	500	300
glass transition (T_g, °C)	300	1000	300	300
Thermal expansion (10^{-7}/K)	120-170	5	150	140
Density (g/cm^3)	5.5	2.2	5.0	4.5
Solubility in water	$< 10^{-2}$	$< 10^{-3}$	soluble	$< 10^{-4}$

Table 7.1: A comparison of selected properties for tellurite, silica, fluoride and chalcogenide glasses (modified from [112]).

longer wavelengths if heavier atoms are introduced into the glass network or if chemical bonds are weakened. Introducing heavy atoms (i.e. heavy metal compounds) or ions with a large ionic radius (i.e. using chalcogen elements S, Se and Te to replace oxygen) can also increases the nonlinear index n_2. It can be seen that heavy metal oxide and chalcogenide based glasses are promising candidates for developing mid-IR nonlinear optical fibres. The chalcogenide glasses possess advantages over the heavy metal oxide glass systems in terms of higher n_2 and longer wavelength multiphonon absorption edges. However, the toxicity, chemical durability and thermal stability of the heavy metal oxide based glasses are typically superior to those of the chalcogenide based glasses. As a brief conclusion for the glass selection, we believe that heavy-metal oxide glasses have adequate properties for achieving mid-IR continuum between 2-5 μm, and are technologically the best developed candidates for immediate experiments.

As a heavy-metal oxide glass material, tellurite glass combines the attributes of [112] (i) a reasonably wide transmission region (0.35-5 μm) versus only 0.2-3 μm for silicate glasses, (ii) good glass stability and corrosion resistance, which present difficulties in fluoride glasses, (iii) a relatively low phonon energy among oxide glass formers, (iv) higher solubilities for rare earths than silica glass, and (v) high refractive index and high nonlinear refractive index, which are generally low in both fluoride and silicate glasses. A comparison of selected optical properties among tellurite, silica, fluoride and chalcogenide glasses is shown in Table 7.1 [112]. It is believed that tellurite glasses could have better glass stability and

chemical durability than halide glasses, better glass stability than chalcogenides, and better compatibility with other oxide glasses than the non-oxide glasses.

Tellurite glass has a nonlinear refractive index (n_2) which is ten times higher than that of pure silica glass. This makes it suitable for highly nonlinear optical fibres. Tellurite glasses have also exhibited Raman gain coefficient about 30 times larger than silica [113]. This high Raman gain coefficient can efficiently increase the effect of soliton self frequency shift occurring in the anomalous dispersion regime of a tellurite fibre. This increased SSFS effect helps broaden the supercontinuum generation into the mid-infrared region, where the tellurite glass has good transmission properties. As a laser its lower phonon energy results in a lower non-radiative transition rate between adjacent rare earth energy levels, leading to fluorescence and laser emission from additional energy levels that are not possible for silicate glasses. The longest fluorescent wavelengths that can be observed are about 2.8 μm, 2.2 μm, 4.4 μm, and 7.4 μm for tellurite, silica, fluoride and chalcogenide glasses, respectively. This is due to the differences in the highest phonon energy for different glass hosts, implying that new fibre lasers and amplifiers at long wavelength are possibly realized using oxide glasses. It was also predicted that new types of photonic bandgaps can be formed in PBGFs based on high-refractive-index glass materials [114, 115], such as tellurite glass.

7.2.2 Fabrication

Selection of tellurite glass composition

The first solid-core tellurite PCF was formed from tellurite glass with composition **5Na_2O-20ZnO-75TeO_2** mol% (called as **Tellurite A** in this chapter) by the University of Bath optoelectronics group in 2003 [62]. Extrusion and fibre fabrication based on **tellurite A** glass were found to be very sensitive to the furnace temperature, making fabrication difficult. As we discussed in Section 3.4.2, the dependance of glass viscosity on temperature determines the degree of difficulty associated in controlling both the extrusion and drawing processes. A steep viscosity curve corresponds to a narrow temperature working range for the fabrication processes. Usually, two thermal parameters of glass are used to identify the working temperature range. These are the glass transition temperature (T_g) and crystallization temperature (T_c). Glass transition temperature (T_g) is

defined as the temperature region in which the behaviour of the material changes from solid-like to liquid-like, corresponding to a viscosity of 10^{12}-10^{13} (see Section 4.3.1). The crystallization temperature indicates the region in which the glass viscosity is sufficiently low to permit rapid crystal growth. It can be defined as the extrapolated onset of the first crystallization exotherm. To achieve a large working range during operations, it is desirable to have $(T_g - T_c)$ as large as possible. Compared to silica glass with a working range around 600 °C, tellurite glasses typically have very steep viscosity curves with a working window range of around 100-200 °C. So temperature working range is one important factor which has to be considered when choosing glass composition. In Patent [116], $(T_g - T_c)$ of **tellurite A** glass was measured to be 112 °C (T_g = 296°C, T_c = 408°C). To obtain a broader working range, we fabricated another composition **75TeO_2-12ZnO-5PbO-3PbF_2-5 Nb_2O_5** (mol%, referred to here as **Tellurite B** in this chapter). According to Patent [116], $(T_g - T_c)$ of a tellurite glass with similar composition to **tellurite B** glass was greater than 200 °C (T_g = 301°C, T_c = 510°C), much broader than **tellurite A** glass. The practical fabrication operations using **tellurite B** glass provided positive validation of this point.

Tellurite PCFs formed from **tellurite B** glass were also found to be much stronger than that from **tellurite A** glass, facilitating the experimental operation with these fibres. Furthermore, **tellurite B** glass is also less susceptible to crystallization against the die walls during the extrusion process. It also has better transmission property in the infrared region.

Manufacturing process

The 'melt and quench' technique was used to produce the tellurite glass. The quality of the glass produced by this process is dependent on the purity of the chemicals used and the method employed in processing these chemicals to glass. The following is our manufacturing procedure for tellurite glasses. (The same procedure was used for the two different glass compositions.)

1). Batching. The chemical materials were merged into the correct molar proportions according to the composition.

2). After batching the crucible containing the glass components was placed in the furnace (Carbolite HTF 14/8 electric furnace, shown in Fig. 7.1(a)) set at a

temperature of 700 °C for 1 hour. This stopped the rapid formation of the liquid melt, which could entrap air that occupies the space between particles.

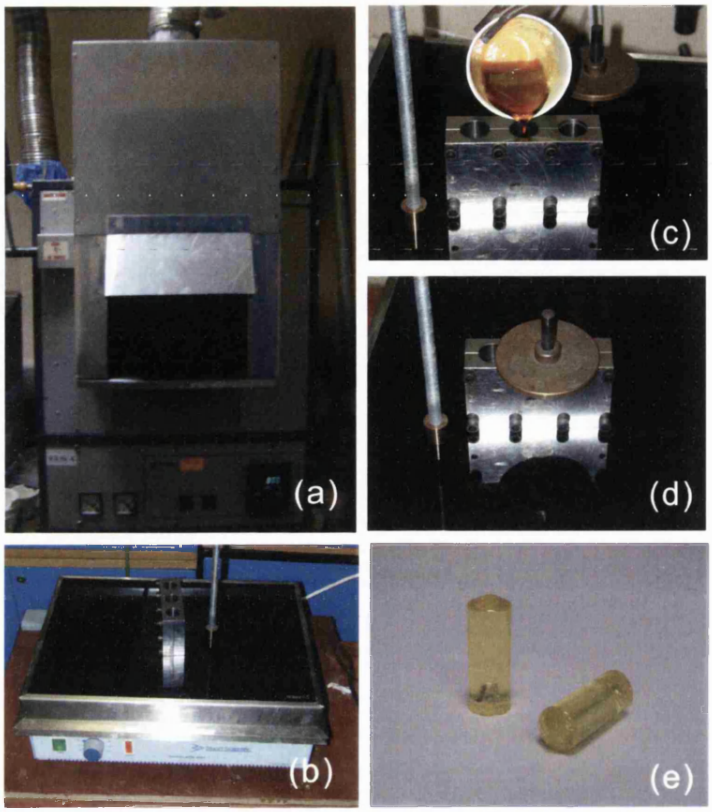

Figure 7.1: Tellurite glass fabrication process. (a) Carbolite HTF 14/8 electric furnace used to heat the glass chemicals. (b) Mild steel mould preheated on a hotplate. (c) Pouring the melt into a glass billet mould. (d) A brass cover was placed on the top of the mould and the hotplate was switched off to allow the mould and glass to cool to room temperature. (e) The final completed tellurite glass billets with diameter of 20 mm and length of 50 mm.

3). The furnace temperature was then increased to 850 °C and held at this temperature for 30 minutes. This allowed complete homogenisation and removal of residual crystallinity of the network to take place without the chance of volatilisation becoming a problem.

4). The furnace temperature was then reduced to 700 °C and held at this temperature for 1 hour. Quenching from too high a temperature could cause the formation of a polycrystalline material rather than glass or cracking of the glass.

5). The melt was poured and quenched in a split mild steel mould, that had been preheated for 20 minutes on a hotplate (Stuart Scientific ceramic hotplate type SH4, shown in Fig. 7.1(b)) to reach a temperature of 300 ^{o}C (around the glass transition temperature) but without allowing oxidisation of the mould surface to take place. After the melt was poured a brass cover which had also been preheated to 300 ^{o}C was placed on top of the mould to stop excessive cooling. Then the hotplate was switched off and the mould was allowed to cool to room temperature. This reduced the risk of the glass billet cracking from excessive internal stresses, or the glass sticking to the mould making it hard to remove.

6). The glass produced was then removed from the mould (shown in Fig. 7.1(e)) and placed in a clean crucible which was placed in the furnace preheated to 300 ^{o}C for 24 hours so that full annealing could take place. The furnace was then switched off and allowed to cool to room temperature.

Problems

During the fabrication procedure, the following problems could be encountered:

1). The glass may contain many small bubbles, which formed in three different ways: a). Rapid formation of a liquid melt could entrap a portion of the air, which initially occupies the space between the particles; b). A component of the glass releasing gas during the melt process; c). Turbulence in the liquid melt entrapping air when poured into the mould;

2). The glass was slightly cloudy, thought to be particles of undissolved materials where complete fusion had not taken place. Possibilities were that materials from the furnace walls fell into the crucible or that aluminium oxide Al_2O_3 from the alumina crucible had been dissolved during fusion.

3). The glass stuck to the mould in several places and was covered in a metal oxide layer in others. This meant that the mould had been at too high a temperature and for too long; if the temperature was low the glass would readily crack.

Though many problems in the manufacturing process existed, tellurite glasses with an acceptable quality have been produced.

7.2.3 Glass properties

The transmission and material dispersion properties of our tellurite glass were measured. To generate mid-infrared supercontinuum, this fibre material needed to maintain a high transmission coefficient into the mid-infrared region. The material dispersion is also a crucial parameter, which needs to be compensated for by the waveguide dispersion of our tellurite PCF. This will allow the zero dispersion wavelength to be shifted to the vicinity of the pump wavelength (1.55 μm for Er fibre laser).

Transmission

A **tellurite B** glass billet was cut into slices, and polished on both sides to form measured samples with thickness of 3 mm. Fig. 7.2 is the transmission spectrum of the sample measured by Fourier Transform Infrared (FTIR) system (Dr. Cristiano Cordeiro, a visitor from the Optics and Photonics Research Centre, UNICAMP, Campinal, Brazil, undertook these measurements). It is seen that our tellurite glass has quite a high and flat transmission window from 1 μm to 2.75 μm, better than silica glass in the mid-infrared region.

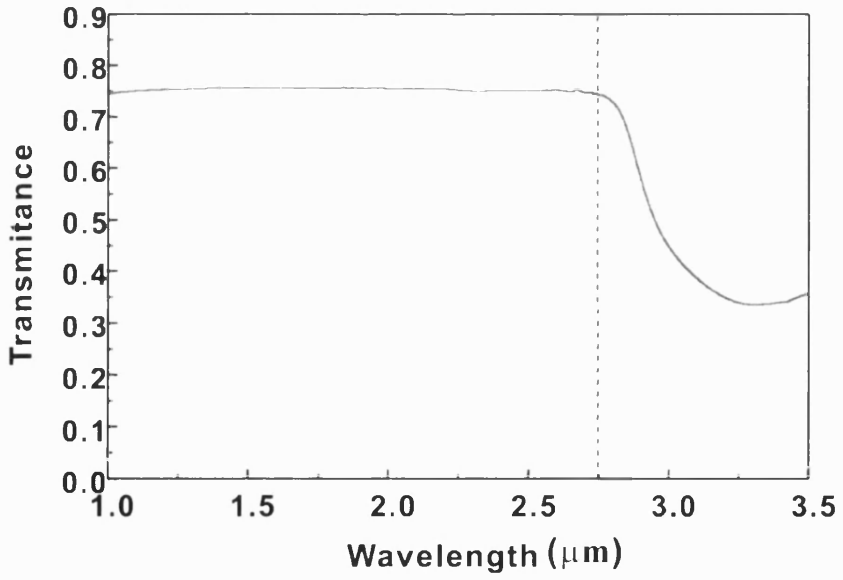

Figure 7.2: Transmission Spectrum of Tellurite Glass B

Dispersion Curve

The group velocity dispersion (GVD) curve of the bulk **tellurite B** glass slice (previously used to measure the transmission spectrum) was measured by low-coherence interferometry and the result is shown in Fig. 7.3. The zero dispersion wavelength is beyond 1.7 μm, which is the limit of the measurement system used.

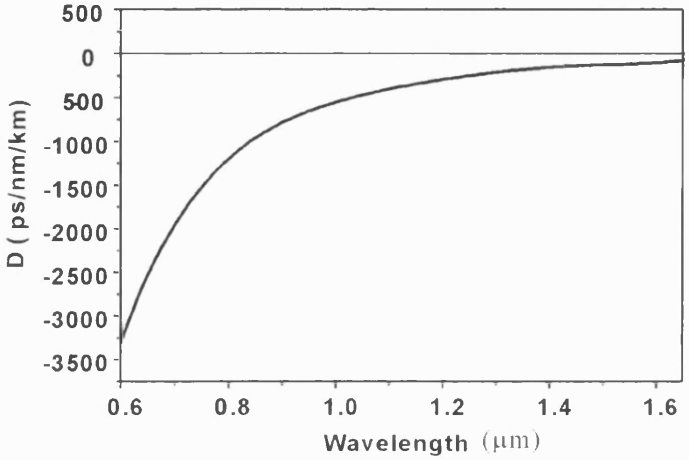

Figure 7.3: Group velocity dispersion curve of bulk tellurite glass B.

7.3 Fabrication of highly nonlinear tellurite PCF

7.3.1 Introduction

The first tellurite PCF based on **tellurite A** glass [62] had a core diameter of 7 μm, with calculated effective area A_{eff} = 21.2 μm and nonlinear coefficient γ = 47.8 km^{-1}W^{-1}. To obtain higher nonlinearity in a tellurite PCF, the core size needs to be decreased. This small core could also shift the zero dispersion wavelength of the fibre to shorter wavelength. Our target was to fabricate a small-core highly nonlinear tellurite PCF with zero dispersion wavelength a little below 1.55 μm. A mode-locked Er fibre ring laser (around 1.55 μm) could then be used as the pump to generate broad supercontinuum into the mid-infrared region.

Many problems were encountered when trying to obtain uniform small-core tellurite PCF with **tellurite A** glass. Its fragility and sensitive viscosity response with temperature made the fibre drawing process quite unstable, especially when we tried to reduce the core size. The following parts of this section will detail the fabrication process of a small-core highly nonlinear tellurite PCF based on **tellurite B** glass.

7.3.2 Extrusion

A direct or forward extrusion process was adapted (see Section 3.4.2) to produce both preforms and jacketing tubes. The extrusion rig, shown in Fig. 7.4(a), was mounted vertically on an existing fibre-drawing tower, and the drawing furnace was used as the heat source. We used a pneumatic actuator attached to the punch to force billets through the dies, shown in Fig. 7.4(b). The extruded glass was then drawn directly from the die to create preforms of 0.8 mm outer diameter, shown in Fig. 7.4(c). The similarity between the shape of the extrusion die and that of the extruded preform demonstrated that the temperature and pressure used were close to optimal. We also extruded jacketing tubes of 1.2 mm internal diameter and 2.5 mm outer diameter in a similar fashion.

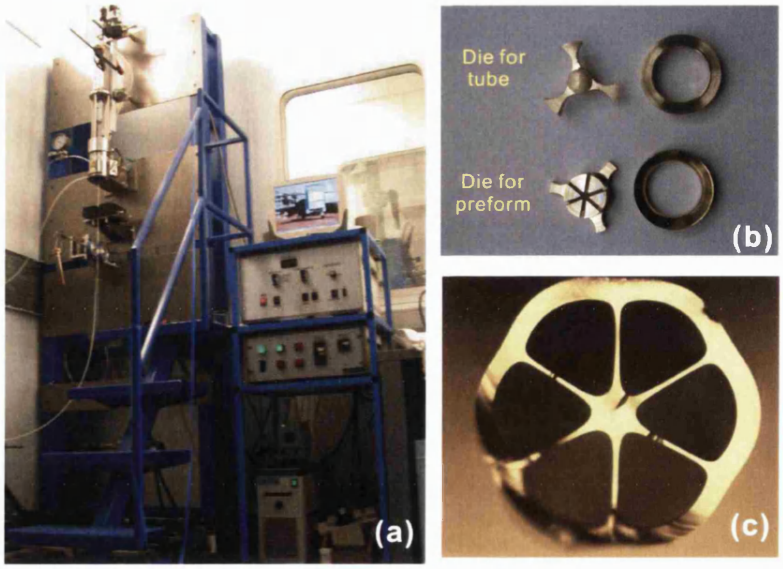

Figure 7.4: (a) Extrusion rig and fibre tower used; (b) Dies designed to extrude tellurite preforms and tubes; (c) Optical micrograph of extruded tellurite preform.

7.3.3 Fibre drawing with two jacketing tubes

The extruded preform was then jacketed using an extruded tube, and drawn to form fibres of tens of meter in length without difficulties. By varying the drawing conditions we were able to obtain fibres with core diameters in the range of 4-7 μm. Apart from decreasing the fibre outer diameter, gas pressure (nitrogen) applied to the preform holes was used to inflate the fibre to obtain a larger draw down ratio, making the fibre core smaller. However, the gas pressure was hard to control, leading to large fluctuations in the fibre size.

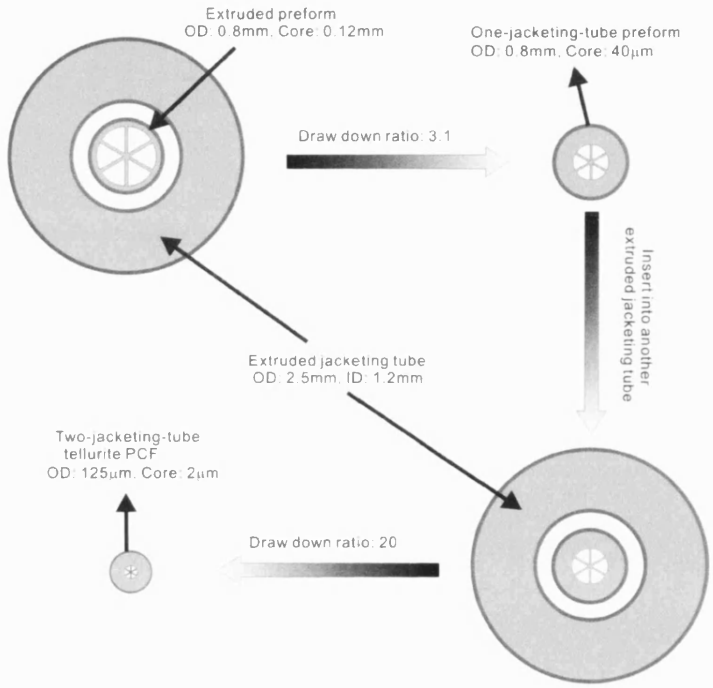

Figure 7.5: Schematic small-core tellurite PCF fabrication process. An extruded tellurite preform was jacketed by a tellurite tube and drawn into one jacket preform with the ratio of 3.1. The one-jacket preform was then jacketed by a second tube and drawn directly to tellurite PCF.

To make a fibre of uniform size, the fabrication process must be stable. The best way to achieve this is to maintain the relative hole character whilst jacketing and drawing the preform twice. This detailed fabrication strategy is presented in Fig. 7.5. An extruded tellurite preform with outer diameter of 0.8 mm was jacketed using an extruded tube with outer diameter of 2.5 mm and simultaneously drawn to a one-jacket preform with a draw down ratio of 3.1. The core size of preform

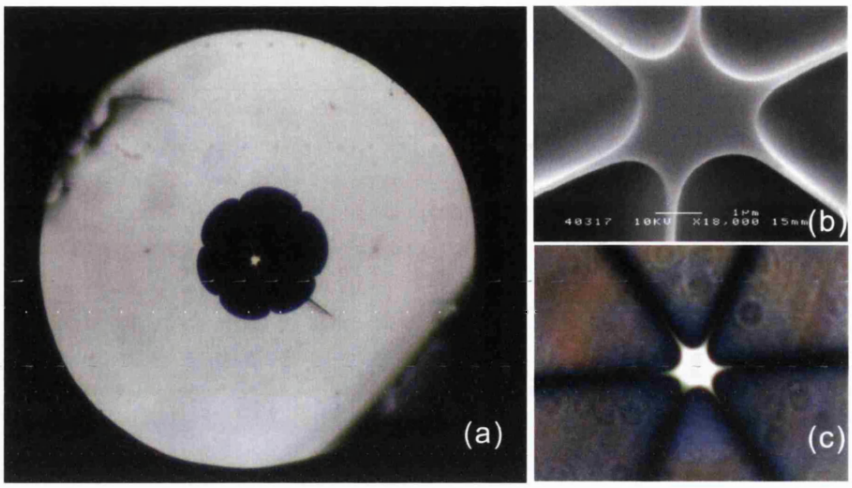

Figure 7.6: (a) Optical micrograph of a tellurite PCF with two jacketing tubes. (b) Scanning electron image of the core region. core size: 2.1 μm, outer diameter: 120 μm, strands: 16 μm long and 120 nm thick. (c) Optical microscopic transmission view of a tellurite PCF.

was decreased from 120 μm to about 40 μm. After jacketing this preform with another extruded tube, the whole structure was then drawn directly to fibre with an outer diameter of 125 μm. The fibre core diameter was expected to be about 2 μm. During this fabrication process, gas pressure was used to keep the holes open, instead of greatly inflating the holes.

Fig. 7.6(a) shows an optical image of the fibre's cross-section. Using a scanning electron image of the core region (Fig. 7.6(b)), the core size of the fibre with outer diameter of 120 μm was measured to be about 2.1 μm. The six strands suspending the core are about 16 μm long and 120 nm thick, enough to isolate the guided light in the core from the solid jacket material. The optical micrograph in Fig. 7.6(c) shows bright guided light transmitted through the core.

7.4 Properties of tellurite PCF

7.4.1 Basic waveguiding properties

The tellurite fibre produced supported many modes due to the large core size (2 μm to 7 μm). However, the fundamental mode could easily be excited using laser sources. The spectral attenuation measured using a white light source and a cut-back technique is shown in Fig. 7.7. The typical minimum measured losses of the fibre (based on **tellurite B** glass) with a core size of 6 μm is about 1.8 dB/m at a wavelength of 1420 nm, and the whole attenuation curve seems to be quite flat from 600 nm to 1750 nm. Compared to the loss measurement result of the first tellurite PCF with a similar core size based on **tellurite A** glass [62] (minimum loss: 2.3 dB/m at 1050 nm, more than 8 dB/m at a wavelength of 1750 nm), our tellurite PCF formed using the new **tellurite B** glass has lower transmission loss, especially in the long wavelength region.

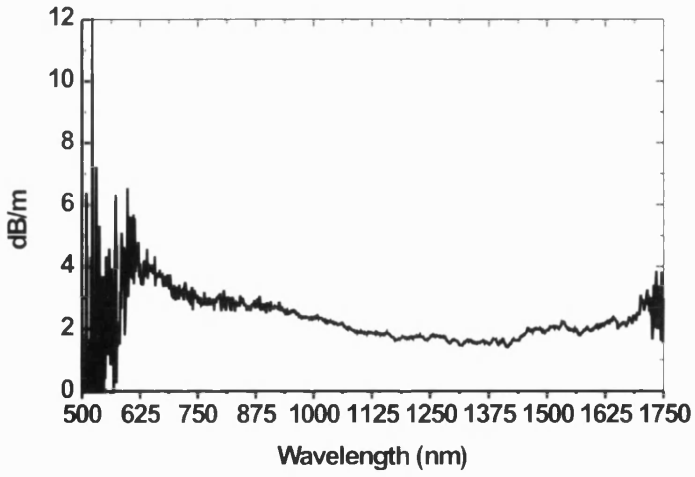

Figure 7.7: Measured spectral attenuation of a tellurite PCF with the core size of 6 μm. The minimum measured loss in this fibre is 1.8 dB/m at a wavelength of 1420 nm. The cutback measurement was carried out based on 2.5 m length of a fibre.

The loss in the fibre is partly due to the bulk glass used for PCF fabrication, and

may be improved by perfecting the fabrication process. Another component of the overall loss is the presence of discrete scattering points in the fibre based on Tellurite A glass (see (Fig. 7.8(a)). These are caused by crystallization during the extrusion process. An example of the cause of such a scattering point due to crystallization in a tellurite A glass PCF is presented in Fig. 7.8(b). This effect can be more serious for smaller-core (2 μm) tellurite fibre where crystallization points attached to the core region greatly increase the transmission loss. The loss of a signal scattering point on the small-core tellurite fibre was measured by cut-back method to be about 0.8 dB.

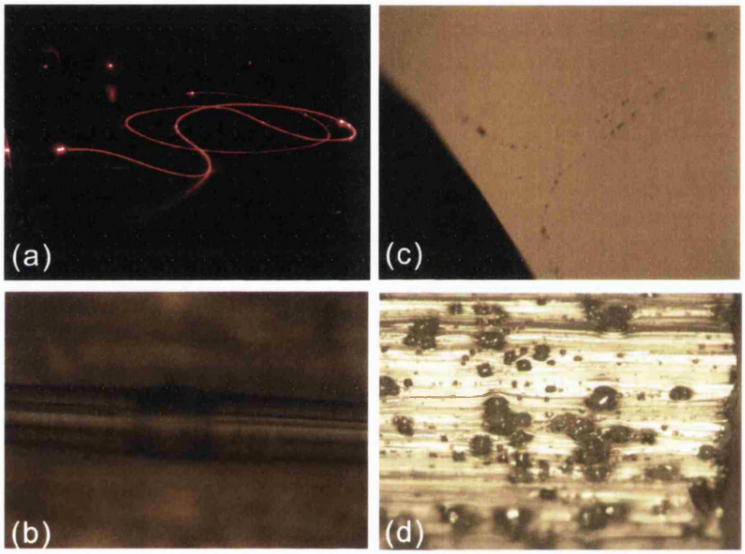

Figure 7.8: (a) Scattering points which cause extra loss in the tellurite PCF. (b) A piece of tellurite PCF with a crystal particle near the fibre core. (c) Internal crystallization caused by mandrel bridges. (d) Surface crystallization on extruded tube. All these pictures are based on Tellurite A glass.

Inspection of an extruded glass tube showed that the outer surface had became rough during the extrusion process. Looking at this tube roughness under the microscope revealed that crystallization had occurred internally as well as on the surface. The internal crystallization formed around the area of the bridges that hold the central mandrel in the extrusion die (see Fig. 7.8 (c) and (d), based on Tellurite A glass). When extruded glass flowed through the metallic dies, a stagnant layer was formed at the metal/glass interface. Crystal growth occurred on the surfaces of the metal die. These crystals grew until they were large enough to enter the glass flow near the die surface and were stripped off. Adjusting the

extrusion temperature and flow rate could decrease the crystal growth which would mean fewer scattering points in the final tellurite fibre. We also noticed that crystal growth rate varied with glass composition [116] and found that the composition of **tellurite A** glass was not the best choice in the tellurite glass family. In fact, better performance was achieved using our new **tellurite B** glass composition.

7.4.2 Group velocity dispersion

Group velocity dispersion of the fibre in Fig. 7.6 was measured using low coherence interferometry and the results are shown in Fig. 7.9. As we discussed in Section 3.3.2, our tellurite PCF can be seen as a tellurite glass strand surrounded by air. The large difference of the core/cladding refractive indices combined with a μm-diameter-sized core provides very strong anomalous waveguide dispersion, which can shift the zero dispersion wavelength of our fibre (the zero dispersion wavelength of bulk tellurite glass is around 2.2 μm [111]) to the telecommunication region (around 1.55 μm). When the core size of the tellurite PCF is reduced to 2.1 μm, the zero dispersion wavelength is shifted to 1.4 μm, as displayed in Fig. 7.9. It is a little below the pump wavelength (around 1.55 μm) of a mode-locked Er fibre laser, facilitating the generation of a broad supercontinuum [27].

7.4.3 Nonlinear coefficient

According to the method described in Section 2.4.2, the effective area of the fibre with a core diameter of 2.1 μm was calculated to be $A_{eff} = 1.7\ \mu m^2$. Using this A_{eff} value and $n_2 = 2.5\times10^{-19} m^2/W$ [112], we calculated the nonlinear coefficient according to Eq.(2.19) with the result: γ=596.1 $km^{-1}W^{-1}$ at 1550nm, much larger than that of the first tellurite PCF (γ=47.8 $km^{-1}W^{-1}$ [62]). It is also more than 5 times higher than the nonlinear coefficient of a silica-based highly nonlinear PCF with 1.8 μm core diameter ($\gamma \sim$95 $km^{-1}W^{-1}$ at 780 nm, NL-PM-750 fibre from Thorlabs).

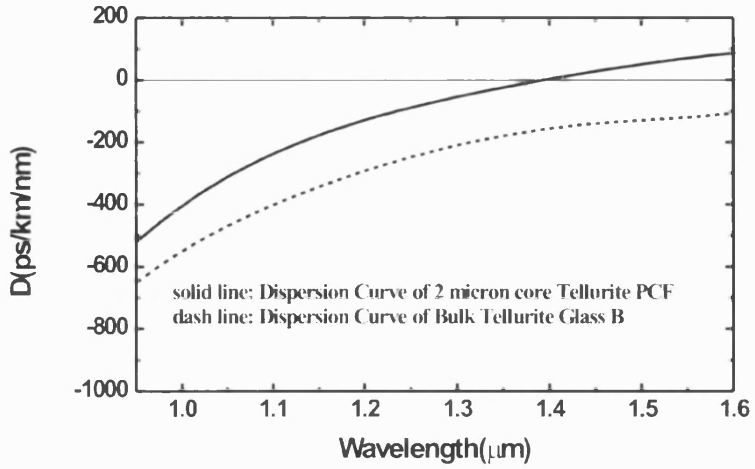

Figure 7.9: Dispersion curves of the fibre with 2.1 μm core (solid line) and bulk **tellurite B** glass (dash line)

7.5 Supercontinuum generation

Pumping at 1.55 μm from an fs Er fibre pump system is a very attractive option for supercontinuum generation. However, such a fibre laser system is not available in our laboratories, so similar femtosecond pulses from an optical parametric amplifier (OPA) were used as the pump to generate mid-infrared supercontinuum in our tellurite PCF with 1.4 μm zero dispersion wavelength. The measurement setup is presented in Fig.7.10.

The Optical Parametric Amplifier (OPA) used as the pump in this experiment is a commercially available Coherent OPA9800 model. For this model, the principle of operation relies on double-passing both the seed and pump wavelengths through a beta barium borate crystal, this generates signal wavelengths from 1200 nm-1600 nm depending on crystal angle. The pump beam is obtained from a Ti:Sapphire-based regenerative amplifier (Coherent RegA9000 model) which is pumped by a solid state Nd:YVO_4 laser (Coherent Verdi V10 model) and seeded by a Ti:Sapphire oscillator (Coherent Mira 900 model) which is also pumped by a Nd:YVO_4 laser (Verdi V5 model). The output of the regenerative amplifier is centred at 800 nm, has a pulse energy of 4 μJ at 250 kHz and a pulse length of

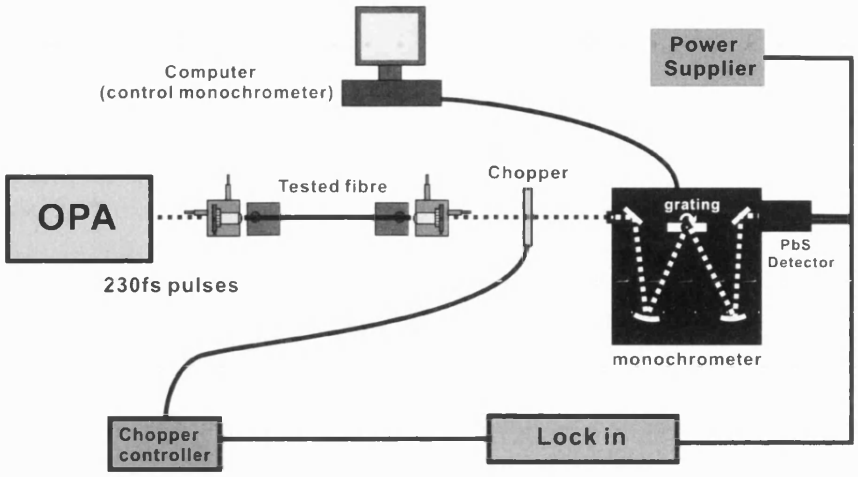

Figure 7.10: Experimental setup to record the supercontinuum spectrum generated in a tellurite PCF using an OPA fs pulse laser at 1.5 μm as a pump.

230 fs in our experiments. On entering the OPA, 25% of this beam power passes through a beam splitter and is focused through a sapphire crystal in order to generate a broadband supercontinuum to act as a seed. The reflected 75% from the beam splitter is used as a pump. The pump and seed beams are subsequently overlapped both temporally and spatially as they make two passes of the crystal. Changing the angle of this crystal by only a few degrees alters the phase matching conditions of the parametric process such that a different seed wavelength from the supercontinuum is amplified. This allows the output signal wavelength to be tuned. The output power depends critically on alignment. For these experiments the pulse energy was around 20 nJ at 1500 nm with a repetition rate of 250 kHz and pulse length of 230 fs.

The pulses from the OPA were launched into our tellurite PCF with core diameter of 2.1 μm. The coupling efficiency was around 8%. Since the output spectrum could reach beyond the range of our OSA (350-1750 nm), for the long wavelength region (>1750 nm) we used a chopper, monochrometer and PbS Infrared detector to measure the generated signals. The monochrometer used was a computer controlled Bentham TMc300F. The grating in the monochromater could measure infrared light up to 5.5 μm. However, the measurement range at the long wavelength edge was limited to about 2.9 μm by the long pass filter in the monochrometer used to block the double frequency diffraction signals from the grating. The detector used to measure output power was a Hamamatsu PbS infrared detector with preamp (thermoelectrically cooled type) P4638 model with

cut-off wavelength of 3.2 μm.

The supercontinuum spectra plotted in Fig. 7.11(A) and (B) were both generated using the same pump source, and correspond to fibre lengths of 15 cm and 4 cm, respectively. Each spectrum is composed of two parts: OSA data for the wavelengths from from 400 nm to 1750 nm and the detector data beyond the OSA range. As we discussed in Section 2.4.6, when femtosecond pulses are launched into a PCF in the anomalous dispersion regime, soliton dynamics play a crucial role in propagation. An input pulse can be seen as a higher-order soliton with soliton number N, which splits into N fundamental solitons with different red-shifted central frequencies and different group velocities. Because of high-order dispersion, every emerging solitons emits blue-shifted phase-matched nonsolitonic radiation (such as in the short wavelength edge of the supercontinuum spectrum in Fig. 7.11). All the split solitons and their corresponding nonsolitonic radiation possess distinct central frequencies, and the width of the generated spectrum increases with increasing initial pulse power and duration. The nonlinear interactions (such as FWM) between the solitons and the blue-shifted waves can generate frequencies falling into these frequency gaps to smooth the supercontinuum spectrum.

As the fibre length was increased from 4 cm to 15 cm, a soliton self-frequency shift effect was observed (see Fig. 7.11). The soliton which appeared near 2.4 μm for 4 cm tellurite fibre was shifted to a longer wavelength by intrapulse Stimulated Raman Scattering, reaching almost 2.8 μm when the fibre length was 15 cm. Furthermore, as the fibre length increased from 4 cm to 15 cm, the supercontinuum spectrum became both smoother and flatter. Supercontinuum measurements for longer tellurite fibres have not been carried out, due to the limited lengths of tellurite fibre we have at present. The best supercontinuum obtained is the result with 15 cm fibre length, spanning more than 2 μm, from 750 nm to wavelengths around 2.8 μm. This result is broader than the result reported (spectral range between 0.9-2.5 μm) using a similarly extruded tellurite microstructured fibre with a triangular core of 2.7 μm diameter [54, 117]. By using longer uniform tellurite PCF, the frequency-shifted soliton is expected to extend into a wavelength region longer than measured in our experiments. However, due to lower transmission beyond 2.75 μm (see Fig. 7.2), increasing the fibre length would have a negative results, so an optimal fibre length needs to be identified in the future. The strong UV-Visible absorption of tellurite glass also restricts

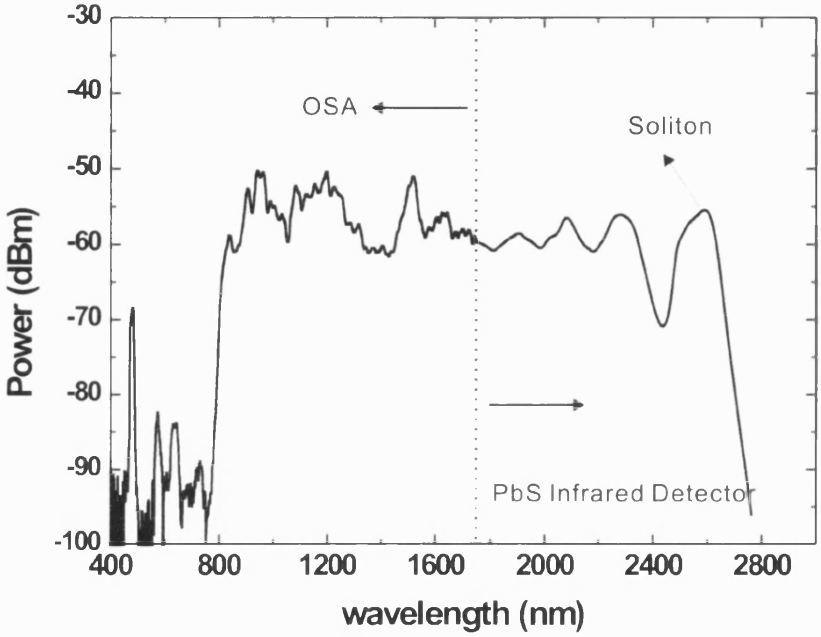

(A) Tellurite PCF:15cm

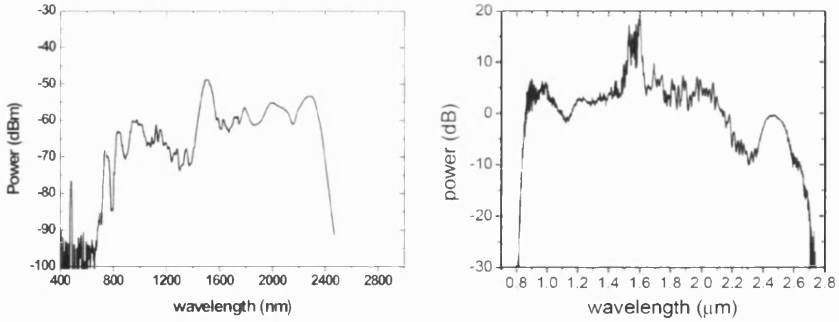

(B) Tellurite PCF: 4cm (C) UV exposed silica HNLF:12cm

Figure 7.11: Supercontinuum measured in tellurite PCFs with fibre lengths of 4 cm (A) and 15 cm (B). The spectrum range from 400-1750 nm was measured by OSA, and the longer wavelength signals were measured by PbS infrared detector. The broadest supercontinuum reported using a silica glass based highly nonlinear fibre is shown in (C) [118].

the supercontinuum performance at the high frequency edge. Uniform low-loss tellurite PCFs with the zero dispersion wavelength closer to the pump wavelength (1.55 μm for Er fibre laser) would help to improve the present supercontinuum results.

The broadest supercontinuum result in the mid-infrared region using a silica glass based optical fibre was reported by J.W. Nicholson, et al [118]. A 12 cm length of highly nonlinear silica fibre (HNLF: A_{eff} = 13.9 μm^2, γ=10.6 $km^{-1}W^{-1}$ at 1550nm), in which 8 cm had been exposed to UV radiation (to enhance supercontinuum generation [119]), was fusion spliced directly to a high power all-fiber source of femtosecond pulses at 1550 nm (similar pulse energy as used in our experiment, but having shorter pulse length and higher coupling efficiency), and the generated supercontinuum spanned approximately 1.65 μm, from 850 nm to wavelengths longer than 2.6 μm, shown in Fig. 7.11(C). Compared to this silica fibre result, our tellurite fibre supercontinuum is a little broader and has a much flatter spectrum especially in the mid-infrared region, where the silica glass fibre is affected by strong absorption.

7.6 Conclusion & Future work

7.6.1 Conclusion

The fabrication of tellurite glasses and tellurite PCF based on the composition **75TeO_2-12ZnO-5PbO-3PbF_2-5 Nb_2O_5** mol% have been described in this chapter. Preforms were fabricated using an extrusion process. The basic waveguiding properties of our tellurite fibre were studied, and highly nonlinear tellurite PCF with a core size of 2.1 μm was measured and found to have a zero dispersion wavelength around 1.4 μm. The small effective area (A_{eff} = 1.7 μm^2) of our fibre and the highly nonlinear refractive index of tellurite glass (n_2= 2.5$\times 10^{-19}$ m^2/W) enabled a nonlinear coefficient of γ=596.1 $km^{-1}W^{-1}$ at 1550nm to be achieved. This highly nonlinear tellurite PCF was expected to generate mid-infrared supercontinuum by using a mode-locked Er fibre ring laser pump with wavelength around 1.55 μm. Even though this desired laser system was not available in our laboratories, similar 230 fs pulses with 1.5 μm wavelength from an OPA were

launched into this fibre, generating broad supercontinuum extending to 2.8 μm. Comparing to other results reported using highly nonlinear silica glass fibre and another tellurite microstructured fibre [117, 118], our supercontinuum is both broader and flatter.

7.6.2 Future work

Optimizing length of tellurite PCF to balance the effects of SSFS at longer wavelength (2.8 μm) and the increasing loss of tellurite glass at these wavelengths needs to be done in the near future. The zero dispersion wavelength of our fibre is expected to be shifted closer to the pump wavelength (1.55 μm for an Er fibre laser) by slightly increasing the core size. All fabrication processes need to be careful controlled to obtain higher-quality PCF with uniform core size and less scattering points, which would contribute to enhanced supercontinuum performance.

Other projects which could be attempted with tellurite glass are to realize an Er-doped tellurite fibre laser at 2.7 μm and to fabricate a hollow-core tellurite PBGF. As we discussed in Section 7.2.1, the high rare earth solubilities and low phonon energy make tellurite glasses good candidates for mid-infrared lasers and amplifiers. Photonic bandgap calculations of a hollow-core PBGF based on high refractive index (>2) predicted the exist of new types of photonic bandgaps, which could be demonstrated in a tellurite hollow-core PBGF.

Chapter 8

Summary and future work

8.1 Summary

This thesis described the fabrications and characterisations of four kinds of microstructured optical fibres and their related applications. In this section, the main conclusions of my thesis work are summarised.

Highly birefringent lamellar core fibre

The fabrication and characterisation of a highly birefringent lamellar-core fibre have been described. With a core size of 1.2 μm, this fibre has a single mode cutoff wavelength of about 1 μm. Direct and indirect methods have been used to measure its birefringence. By direct observation of scattered light, the beat length was measured to be 85 μm at a wavelength of 543 nm, corresponding to the birefringence of 6.4×10^{-3}. This is the highest phase birefringence reported in a single mode optical fibre. The differential group delay was measured using low coherence interferometry providing a group birefringence of 8.8×10^{-3} at 1540 nm. We computed the modal indices using a commercial beam propagation tool, and found that the measured values were not consistent with preservation of the bulk refractive indices within the multilayer stack forming the core. The decreased refractive index contrast within the fibre core was attributed to diffusion of components within the multilayer structure. When accounting for modest diffusion, the modelling results fit well with the experimental results.

Three-level Nd fibre laser incorporating photonic bandgap fibre

Chapter 5 has presented a robust and efficient Neodymium fibre laser configuration incorporating an all-solid bandgap fibre. In this laser system, the in-line fibre filter function of this PBGF has been fully demonstrated, suppressing the four-level transition and obtaining efficient lasing at 907 nm. The laser shows a maximum slope efficiency of 32% and threshold pump power of 70 mw. Further slight improvements are anticipated, which can be realized by improving the splice losses through redesign of the PBGF, and ultimately by incorporating a high gain medium directly into the PBGF. Further demonstrations of its filter function have also been described using several slightly different sizes (corresponding to different transmission spectra) in this Nd laser system, and the potential application to force weak 1.3 μm lasing of a Nd fibre laser has been predicted. Compared to use of a W-index fibre, the PBGF has a high wavelength discrimination, and in principle could also be used to suppress gain at shorter wavelengths, which is not possible with the W-type fibre.

Bend losses of an all-solid photonic bandgap fibre based on an array of oriented rectangular high-index rods

The fabricated low-index-contrast all-solid PBGFs have been used to study the the nature of photonic bandgaps, especially bend losses. The obtained explanation of the bend loss mechanism helps us to understand the bandgap properties, including those of hollow-core PBGFs, and guided us to improve the design of all-solid PBGFs. A direct example is that an all-solid PBGF based on an array of raised-index ring rods can posses improved resistance to bend loss. Different from earlier reported all-solid PBGFs, whose high-index rods in the bandgap cladding have circular symmetry, another new kind of all-solid PBGF based on an array of oriented rectangular rods was fabricated and characterised by myself in this thesis. From the near-field patterns of modes at the band edges, the rod modes defining their corresponding bandgaps were easily identified, coinciding with the numerical modelling of cladding band structures. Arising from this new cladding rod symmetry, directional dependance of bend losses, relative to the orientation of the rectangular rods, has been observed and measured. The detailed directional bend loss properties for each bandgap were explained according to the density of states of the cladding and the directional coupling properties of different cladding

rod modes.

Extruded highly nonlinear PCF formed from tellurite glass for mid-infrared supercontinuum generation

The fabrications and characterisations of tellurite glasses and tellurite PCF based on the composition of **75TeO_2-12ZnO-5PbO-3PbF_2-5Nb_2O_5** mol% have been described in Chapter 7. This tellurite glass has proved to have better performance during the fibre fabrication processes and have higher transmission coefficient (especially in the long wavelength region) than the glass material used to form the first reported tellurite PCF [62]. Based on this tellurite glass, preforms were fabricated using an extrusion process, which were then drawn to fibres with a core size of 2.1 μm. This small-core tellurite PCF was calculated to have a small effective area of A_{eff} = 1.7 μm^2 and high nonlinear coefficient (γ=596.1 $km^{-1}W^{-1}$) at 1550 nm. With the measured zero dispersion wavelength of 1.4 μm, this highly nonlinear tellurite PCF was expected to generate mid-infrared supercontinuum by using a mode-locked Er fibre ring laser pump with the wavelength around 1.55 μm. Even though this desired laser system was not available in our laboratories, similar femtosecond pulses with 1.5 μm wavelength from OPA were used to generate broad supercontinuum extending into 2.8 μm, which was better than the supercontinuum results reported using similar tellurite microstructured fibre with triangle core and silica-glass-based highly nonlinear fibre.

8.2 Future work

Based on above results, some improvements and new research possibilities could be realized in further work.

Further developed fabrication techniques with the soft glasses (glass rod drilling and polishing technique) could be used to enhance the performance of our highly birefringent lamellar core fibre. Lower loss could be obtained by directly drawing a drilled LLF1 glass tube with inserted lamellar structure under vacuum to eliminate air bubbles possibly trapped at the interfaces between adjacent glass plates. Higher birefringence, corresponding to less diffusion occurred during fabrication, could be realized by drawing the preform with multi-jacketing tubes (or SF6 glass

as the most outer tube) to decrease the drawing temperature and steps. This fabrication technique is also quite useful to perfect the fabrication of other kinds of PCFs based on soft glass rods, such as SF6 glass PCF by the 'stack and draw' method.

Rare-earth core-doped all-solid PBGFs have broad applications in adjusting the intrinsic gain profiles of these optical fibres. As an extension of the Nd fibre laser work in Chapter 5, we plan to incorporate a Nd-doped core into an all-solid PBGF directly. With modified gain profile using photonic bandgaps, this fibre could be useful as a fibre laser or amplifier. Obtaining lasing at different wavelengths can be easily realized by changing the fibre diameter to shift the bandgaps locations to the desired wavelengths. Other rare earth dopants are also very interesting to be incorporated into the bandgap fibre, such as Yb [100] or Er ions, to realize related applications. As well as the wavelength discrimination, the anomalous GVD at the wavelength below 1.3 μm, not possessed by conventional optical fibres, can also be quite useful to provide the necessary dispersion compensation in a mode-locked fibre laser system. Both the filter and dispersion compensation functions of our all-solid PBGF could be demonstrated in a mode-locked Nd doped fibre ring laser working around 0.9 μm.

Bandgap engineering has been demonstrated in an all-solid PBGF based on a 2-d array of raised-index cladding rings by re-ordering the cladding modes in such a way as to broaden the photonic band gaps and reduce bend sensitivity. Further engineering of the bandgaps can be obtained through breaking the ring structure into periodic high-index blobs. Preliminary modelling results of photonic density of states (DOS) of such a fibre has shown broad bandgaps and bands, corresponding to low loss and high loss transmission windows of the fibre, respectively. The widths of these bandgaps and bands can be modified by controlling the blob diameter and the value of d/Λ. These broad bandgaps have potential applications in light transmission systems and the broad high loss bands could be used to suppress the undesirable noise components in high-power optical amplifiers or delivery systems, where the amplified noises waste pump power and can potentially overwhelm the desired signals. They could also provide more freedoms for PBGF design, when using a PBGF as an in-line fibre filter (like the work in Chapter 5) or incorporating a rare earth doped core into the PBGF to adjust the gain profile.

Uniform low loss tellurite PCFs with the zero dispersion wavelength closer to the pump wavelength (such as 1.5 μm for Er fibre laser) are intended to be fabricated in the future work. Broader supercontinuum generated from a highly nonlinear tellurite PCF could be obtained by optimizing the tellurite fibre length to balance the effects of soliton self-frequency shift (SSFS) at longer wavelength (2.8 μm) and the increasing loss of tellurite glass at these wavelengths. Other related work based on tellurite glasses are also of interest, such as an Er-doped tellurite PCF for lasing at 2.7 μm and a hollow-core tellurite PBGF.

References

[1] K.C. Kao and G.A. Hockham. Dielectric-fibre surface waveguides for optical frequencies. *Proceedings IEE* **113**:1151 (1966).

[2] P.St.J. Russell. Photonic crystal fibers. *Science* **299**:358 (2003).

[3] J.C. Knight. Photonic crystal fibers. *Nature* **424**:847 (2003).

[4] D. Gloge. Weakly guiding fibers. *Applied Optics* **10**:2252 (1971).

[5] Allan W Snyder and John D Love. *Optical Waveguide Theory.* Chapman & Hall Ltd., London (1983).

[6] Govind P. Agrawal, *Fiber-optic communications systems*, Third Edition, John Wiley & Sons, Inc. (2002).

[7] H.F. Taylor. Bending effects in optical fibers. *Journal of Lightwave Technology* **2**:617 (1984).

[8] Govind P. Agrawal. *Nonlinear Fiber Optics.* Academic Press, Third Edition (2001).

[9] R.B. Dyott. *Elliptical Fibre Waveguides.* Artech House (1995).

[10] D.N. Payne, A.J. Barlow, and J.J. Ramskov-Hansen. Development of low- and high-birefringence optical fibers. *Journal of Quantum Electronics* **QE-18**:477 (1982).

[11] T. Hosaka, K. Okamoto, T. Miya, Y. Sasaki, and T. Edahiro. Low-loss single polarisation fibers with asymmetrical strain birefringence. *Electronics Letters* **17**:530 (1981).

[12] M.P. Varnham, D.N. Payne, R.D. Birch, and E.J. Tarbox. Single-polarization operation of highly birefringent bow-tie optical fibers. *Electronics Letters* **19**:246 (1983).

[13] R.B. Dyott, J.R. Cozens, and D.G. Morris. Preservation of polarization in optical-fiber waveguides with elliptical cores. *Electronics Letters* **15**:380 (1979).

[14] T. Okoshi, K. Oyamada, M. Nishimura, and H. Yokata. Side-tunnel-fiber: An approach to polarization maintaining optical waveguide scheme. *Electronics Letters* **18**:824 (1982).

[15] A.W. Snyder and Xue-Heng Zheng. Optical fibers of arbitrary cross sections. *Journal of the Optical Society of America. A, Optics and Image science* **3**:600 (1986).

[16] Shen YR. *Principles of Nonlinear Optics.* Wiley, New York (1984).

[17] John A. Buck. *Fundamentals of Optical Fibers.* Jon Wiley & Sons, Inc., USA (1995).

[18] A. Boskovic, S.V. Chernikov, J.R. Taylor, L. GrunerNielsen, and O.A. Levring. Direct continuous-wave measurement of n_2 in various types of telecommunication fiber at 1.55μm. *Optics Letters* **21**:1966 (1996).

[19] F.M. Mitschke and L.F. Mollenauer. Discovery of the soliton self-frequency shift. *Optics Letters* **11**:659 (1986).

[20] J.P. Gordon. Theory of the soliton self-frequency shift. *Optics Letters* **11**:662 (1986).

[21] I. Hartl, X.D. Li, C. Chudoba, R. Ghanta, T. Ko, J.G. Fujimoto, J.K. Ranka, R.S. Windeler, and A.J. Stentz. Ultrahigh-resolution optical coherence tomography using continuum generation in an air-silica micostructured optical fiber. *Optics Letters* **26**:608 (2001).

[22] R. Holzworth, J. Reichert, Th. Udem, T.W. Hansch, J.C. Knight, W.J. Wadsworth, and P.St.J. Russell. An optical frequency synthesiser for precision spectroscopy. *Physical Review Letters* **85**:2264 (2000).

[23] S. Coen, A.HL. Chau, R.L.eonhardt, J.D. Harvey, J.C. Knight, W.J. Wadsworth, and P.S.J. Russell. White-light supercontinuum generation

with 60-ps pump pulses in a photonic crystal fiber. *Optics Letters* **26**:1356 (2001).

[24] A. Ortigosa-Blanch, J.C. Knight, and P.St.J. Russell. Pulse breaking and supercontinuum generationwith 200-fs pump pulses in photonic crystal fibre. *Journal of the Optical Society of America B* **19**:2567 (2002).

[25] A.V. Husakou and J. Herrmann. Supercontinuum Generation of Higher-Order solitons by Fission in Photonic Crystal Fibers. *Physical Review Letters* **87**:230901 (2001).

[26] J. Herrmann, U. Griebner, N. Zhavoronkov, A. Husakou, D. Nickel, J.C. Knight, W.J. Wadsworth, P.St.J. Russell, and G. Korn. Experimental Evidence for Supercontinuum Generation by Fission of Higher-Order Solitons in Photonic Fibers. *Physical Review Letters* **88**:173901 (2002).

[27] Anton V. Husakou and Joachim Herrmann. Supercontinuum generation, four-wave mixing, and fission of higher-order solitons in photonic-crystal fibers. *Journal of the Optical Society of America B* **19**:2171 (2002).

[28] J.K. Ranka, R.S. Windeler, and A.J. Stentz. Visible continuum generation in air-silica microstructure optical fibers with anomalous dispersion at 800nm. *Optics Letters* **25**:25 (2000).

[29] G. Genty, M. Lehtonen, H. Ludvigsen, J. Broeng, and M. Kaivola. Spectral broadening of femtosecond pulses into continuum radiation in microstructured fibers. *Optics Express* **10**:1083 (2002).

[30] W.J. Wadsworth, A.Ortigosa-Blanch, J.C. Knight, T.A. Birks, T.P. Martin Man, and P.St.J. Russell. Supercontinuum generation in photonic crystal fibers and optical fiber tapers: a novel light source. *Journal of the Optical Society of America B* **19**:2148 (2002).

[31] W.J. Wadsworth, N. Joly, J.C. Knight, T.A. Birks, F. Biancalana, and P.St.J. Russell. Supercontinuum and four-wave mixing with Q-switched pulses in endlessly single-mode photonic crystal fibres. *Optics Express* **12**:299 (2004).

[32] Hans Lydtin. PCVD: A Technique Suitable for Large-Scale Fabrication of Optical Fibers. *Journal of Lightwave Technology* **LT-4**:1034 (1986).

[33] J.B. MacChesney, P.B. OConnor, and H.M. Presby. A new technique for preparation of low-loss and graded index optical fibers. *Proceedings of the IEEE* **62**:1278 (1974).

[34] S.R. Nagel, J.B.MacChesney, and K.L. Walker. An overview of the modified chemical vapor deposition (mcvd) process and performance. *IEEE Journal of Quantum Electronics* **MTT-30**:305 (1982).

[35] J.C. Knight, T.A. Birks, P.St.J. Russell, and D.M. Atkin. All-silica single-mode optical fiber with photonic crystal cladding. *Optics Letters* **21**:1547 (1996).

[36] J.C. Knight, T.A. Birks, P.St.J. Russell, and D.M. Atkin. All-silica single-mode optical fiber with photonic crystal cladding. errata. *Optics Letters* **21**:1547 (1997).

[37] T.A. Birks, J.C. Knight, and P. St. J. Russell. Endlessly single-mode photonic crystal fiber. *Optics Letters* **22**:961 (1997).

[38] J.C. Knight, T.A. Birks, R.F. Cregan, P.St.J. Russell, and J.P. de Sandro. Large mode area photonic crystal fibre. *Electronics Letters* **34**:1347 (1998).

[39] R.F. Cregan, B.J. Mangan, J.C. Knight, T.A. Birks, P.St.J. Russell, P.J. Roberts, and D.C. Allan. Single-mode photonic band gap guidance of light in air. *Science* **285**:1537 (1999).

[40] J.C. Knight, J. Broeng, T.A. Birks, P.St.J. Russell. Photonic Band Gap Guidance in Optical Fibers. *Science* **282**:1476 (1998).

[41] A. Abeeluck, N. Litchinitser, C. Headley, and B. Eggleton. Analysis of spectral characteristics of photonic bandgap waveguides. *Optics Express* **10**:1320 (2002).

[42] N.M. Litchinitser, A.K. Abeeluck, C. Headley, and B.J. Eggleton. Antiresonant reflecting photonic crystal optical waveguides. *Optics Letters* **27**:1592 (2002).

[43] N. Litchinitser, S. Dunn, B. Usner, B. Eggleton, T. White, R. McPhedran, and C. de Sterke. Resonances in microstructured optical waveguides. *Optics Express* **11**:1243 (2003).

[44] N. Litchinitser, S. Dunn, P. Steinvurzel, B. Eggleton, T. White, R. McPhedran, and C. de Sterke. Application of an ARROW model for designing tunable photonic devices. *Optics Express* **12**:1540 (2004).

[45] T.A. Birks, D. Mogilevtsev, J.C. Knight, P.St.J. Russell, and J. Broeng. The analogy between photonic crystal fibres and step index fibres. *Optical Fiber Communication Conference (OFC) 1999*, paper **FG4-1**:114 (1999).

[46] G. Bouwmans, F. Luan, J.C. Knight, P.St.J. Russell, L. Farr, B.J. Mangan, H. Sabert. Properties of a hollow-core photonic bandgap fiber at 850nm wavelength. *Optics Express* **11**:1613 (2003).

[47] F. Luan, A.K. George, T.D. Hedley, G.J. Pearce, D.M. Bird, J.C. Knight, and P.St.J. Russell. All-solid photonic bandgap fiber. *Optics Letters* **29**:2369 (2004).

[48] J.C. Knight, J. Arriaga, T A. Birks, A. Ortigosa-Blanch, W.J. Wadsworth, and P.St.J. Russell. Anomalous Dispersion in Photonic Crystal Fiber. *IEEE Photonics Technology Letters* **12**:807 (2000).

[49] W.H. Reeves, J.C. Knight, P.St.J. Russell, and P.J. Roberts. Demonstration of ultra-flattened dispersion in photonic crystal fibers. *Optics Express*, **10**:609 (2002).

[50] W.H. Reeves, D.V. Skryabin, F. Biancalana, J.C. Knight, P.S. Russell, F.G. Omenetto, A. Efimov, and A.J. Taylor. Transformation and control of ultra-short pulses in dispersion engineered photonic crystal fibres. *Nature* **424**:511 (2003).

[51] T.M. Monro, K.M. Kiang, J.H. Lee, K. Frampton, Z. Yusoff, R. Moore, J. Tucknott, D. W. Hewak, H.N. Rutt and D.J. Richardson. High nonlinearity extruded single-mode holey optical fibers. *Optical Fiber Communication Conference (OFC) 2002*, Post deadline paper **FA1** (2002).

[52] V.V.R. Kumar, A. George, W. Reeves, J.C. Knight, P.St.J. Russell, F. Omenetto, and A. Taylor. Extruded soft glass photonic crystal fiber for ultrabroad supercontinuum generation. *Optics Express* **10**:1520 (2002).

[53] K.M. Kiang, K. Frampton, T.M. Monro, R. Moore, J. Tucknott, D.W. Hewak, D.J. Richardson, and H.N. Rutt. Extruded singlemode non-silica glass holey optical fibres. *Electronics Letters* **38**:546 (2002).

[54] X. Feng, T.M. Monro, V. Finazzi, R.C. Moore, K. Frampton, P. Petropoulos, and D.J. Richardson. Extruded singlemode, high-nonlinearity, tellurite glass holey fibre. *Electronics Letters* **41**:835 (2005).

[55] X. Feng, Arshad K. Mairaj, Daniel W. Hewak, and Tanya M. Monro. Non-silica Glasses for Holey Fibers. *Journal of Lightwave Technology* **23**:2046 (2005).

[56] E. Roeder. Extrusion of glass. *Journal of Non-Crystalline Solids* **5**:377 (1971).

[57] E. Roeder. Flow behaviour of glass during extrusion. *Journal of Non-Crystalline Solids* **7**:203 (1972).

[58] A Ortigosa-Blanch, J.C. Knight, W.J. Wadsworth, J. Arriaga, B.J. Mangan, T.A. Birks, and P.St.J. Russell. Highly birefringent photonic crystal fibers. *Optics Letters* **25**:1325 (2000).

[59] B.J. Mangan, J.C. Knight, T.A. Birks, P.St.J. Russell and A.H. Greenaway. Experimental study of dual-core photonic crystal fibre. *Electronics Letters* **36**(16):1358 (2000).

[60] G. Bouwmans, R. M. Percival, W. J. Wadsworth, J. C. Knight, and P. St. J. Russell. High-power Er:Yb fiber laser with very high numerical aperture pump-cladding waveguide. *Applied Physics Letters* **83**(5):817 (2003).

[61] W. J. Wadsworth, R. M. Percival, G. Bouwmans, J. C. Knight, and P. St. J. Russell. High power air-clad photonic crystal fibre laser. *Optics Express* **11**(1):48 (2003).

[62] V.V.R. Kumar, A.K. George, J.C. Knight, and P.St.J. Russell. Tellurite photonic crystal fiber. *Optics Express* **11**:2641 (2003).

[63] X. Feng, T.M. Monro, P. Petropoulos, V. Finazzi, and D. Hewak. Solid microstructured optical fiber. *Optics Express* **11**:2225 (2003).

[64] J.C. Knight, J. Broeng, T.A. Birks, and P.St.J. Russel. Photonic band cap guidance in optical fibers. *Science* **282**:1476 (1998).

[65] B.J. Mangan, L. Farr, A. Langford, P.J. Roberts, D.P. Williams, F. Couny, M. Lawman, M. Mason, S. Coupland, R. Flea, H. Sabert, T.A. Birks, J.C. Knight and P.St.J. Russell. Low loss (1.7 dB/km) hollow core photonic

bandgap fiber. *Optical Fiber Communication Conference (OFC) 2004*, paper **PDP24** (2004).

[66] A. Argyros, T. Birks, S. Leon-Saval, C. M. Cordeiro, F. Luan, and P. S. J. Russell. Photonic bandgap with an index step of one percent. *Optics Express* **13**:309 (2005).

[67] G. Bouwmans, L. Bigot, Y. Quiquempois, F. Lopez, L. Provino, and M. Douay. Fabrication and characterization of an all-solid 2D photonic bandgap fiber with a low-loss region (< 20 dB/km) around 1550 nm. *Optics Express* **13**:8452 (2005).

[68] A. Pureur, A. Betourne, G. Bouwmans, L. Bigot, M. Douay, Y. Quiquempois. Bending losses in all Solid 2D Photonic Band-Gap Fibers: A limiting Factor? *European Conference on Optical Communications (ECOC) 2006*, paper **We3.P.34** (2006).

[69] J.M. Stone, G.J. Pearce, F. Luan, T.A. Birks, J.C. Knight, A.K. George, and D.M. Bird. An improved photonic bandgap fiber based on an array of ring. *Optics Express* **14**:6291 (2006).

[70] Max Born and Emil Wolf. *Principles of Optics*. Sixth Edition, Pergamon, Oxford (1980).

[71] Narbottam P. Bansal and R.H. Doremus. *Handbook of glass properties*. Orlando, Fla. London, Academic Press (1986).

[72] K. Lyytikainen, S. Huntington, A. Carter, P. McNamara, S. Fleming, J. Abramczyk, I. Kaplin, and G. Schötz. Dopant diffusion during optical fibre drawing. *Optics Express* **12**:972 (2004).

[73] M. D. Feit and J. A. Flec. Light propagation in graded-index optical fibers. *Applied Optics* **17**:3990 (1978).

[74] D. Yevick. A guide to electric field propagation techniques for guided-wave optics. *Optical and Quantum Electronics* **26(3)**:S185 (1994).

[75] R. Scarmozzino, A. Gopinath, R. Pregla and S. Helfert. Numerical techniques for modeling guided-wave photonic devices. *IEEE Journal of Selected Topics in Quantum Electronics* **6**:150 (2000).

[76] John M. Fini, Ryan T. Bise, Man F. Yan, Andrew D. Yablon, and Patrick W. Wisk. Distributed fiber filter based on index-matched coupling between core and cladding. *Optics Express* **13**:10022 (2005).

[77] A. Isomäki and O. G. Okhotnikov. Femtosecond soliton mode-locked laser based on ytterbium-doped photonic bandgap fiber. *Optics Express* **14**:9238 (2006).

[78] E. Snitzer. Optical maser action of Nd^{3+} in a barium crown glass. *Physical Review Letters* **7**:444 (1961).

[79] L.F. Johnson and K. Nassau. Infrared fluorescence and stimulated emission of Nd^{3+} in $CaWO_4$. *Proceeding of the Institute of Radio Engineers* **49**:1704 (1961).

[80] E. Snitzer. Neodymium glass laser. *Third International Conference on Quantum Electronics* **1**:999 (1963).

[81] C.J. Keoster, E. Snitzer. Amplification in a fiber laser. *Applied Optics* **3**:1182 (1964).

[82] J. Stone, C.A. Burrus. Neodymium-doped silica laser in end-pumped fiber geometry. *Applied Physics Letters* **23**:388 (1973).

[83] R.J. Mears, L. Reekie, S.B. Poole and D.N. Payne. Neodymium-doped silica single-mode fibre laser. *Electornics Letters* **21**:738 (1985).

[84] L. Reekie, I. M. Jauncey, S. B. Poole and D. N. Payne. Diode-laser-pump Nd^{3+}-doped fibre laser opterating at 938nm. *Electronics Letters* **23**:884 (1987).

[85] F. Hakimi, H. Po, R. Tumminelli, B.C. McCollum, L. Zenteno, H.M. Cho, and E. Snitzer. Glass fiber laser at 1.36μm from SiO_2:Nd. *Optics Letters* **14**:1060 (1989).

[86] J. Swiderski, A. Zajac, Skorczakowski M.,Z. Jankiewicz, and P. Konieczny. Rare-earth-doped high-power fiber lasers generating in near infrared range *Opto-Electronics Review* **12**:169 (2004).

[87] Zhonghong Jiang, Jianhu Yang, and Shixun Dai. Optical sepctroscopy and gain properties of Nd^{3+}-doped oxide glasses. *Journal of the Optical Society of America B* **21**:739 (2004).

[88] Peter D. Dragic and George C. Papen. Efficient Amplification Using the $^4F_{3/2} \longrightarrow ^4I_{9/2}$ Transition in Nd-Doped Silica Fiber. *IEEE Photonics Technology Letters* **11**:1593 (1999).

[89] R.D. Mauer. Operation of Nd^{3+} glass optical maser at 9180Å. *Applied Optics* **2**:87 (1963).

[90] O. G. Okhotnikov and J. R. Salcedo. Spectroscopy of the transient oscillations in a Nd^{3+}-doped fiber laser for the four-level $^4F_{3/2}$-$^4I_{11/2}$ (1060 nm) and three-level $^4F_{3/2}$-$^4I_{9/2}$ (900 nm) transitions. *Applied Physics Letters* **64**:2619 (1994).

[91] P.B. Mauer. Laser action in neodymium-doped glass at 1.37 microns. *Applied Optics* **3**:153 (1964).

[92] M.L. Dakss and W.J. Miniscalco. Fundamental Limits on Nd^{3+}-Doped Fiber Amplifier Performance at 1.3 μm. *IEEE Photonics Technology Letters* **2**:650 (1990).

[93] Anthony L. Cook and Herbert D. Hendricks. Diode-laser-pumped tunable 896-939.5 nm neodymium-doped fiber laser with 43-mW output power. *Applied Optics* **37**:3276 (1998).

[94] Z. Chu, T.D. Wilkerson, and U.N. Singh. Water-vapor absorption line measurements in the 940 nm band by using a Raman-shifted dye laser. *Applied Optics* **32**:992 (1993).

[95] Kazuo Arai, Hiroshi Namikawa, Ken Kumata, Tatsutoku Honda, Yoshiro Ishii and Takashi Handa. Aluminum or phosphorus co-doping effects on the fluorescence and structural properties of neodymium-doped silica glass. *Journal of Appllied Physics* **59**:3430 (1986).

[96] Seongwoo Yoo, Daniel B.S. Soh, J. Kim, Y. Jung, J. Nilsson, J.K. Sahu, Jhang W. Lee and K. Oh. Analysis of W-type waveguide for Nd-doped fiber laser operating near 940 nm. *Optics Communications* **247**:153 (2005).

[97] W.W. Rigrod. Saturation Effects in High-Gain Lasers. *Journal of Applied Physics* **36**:2487 (1965).

[98] E. O. Schulz du Bois. Pulse sharpening and gain saturation in traveling-wave masers. *The Bell System Technical Journal* **43**:625 (1964).

[99] I.P. Alcock, A.I. Ferguson, D.C. Hanna and A.C. Tropper. Tunable, continuous-wave neodymium-doped monomode-fiber laser operating at 0.900-0.945 and 1.070-1.135 μm. *Optics Letters* **11**:709 (1986).

[100] A. Isomäki and O. G. Okhotnikov. All-fiber ytterbium soliton mode-locked laser with dispersion control by solid-core photonic bandgap fiber. *Optics Express* **14**:4368 (2006).

[101] T.P. Handen, J. Broeng, C. Jakobsen, G. Vienne, H.R. Simonsen, M.D. Nielsen, P.M.W. Skovgaard, J.R. Folkenberg and A. Bjarklev. Air-guiding photonic bandgap fibers: spectral properties, macrobending loss, and practical handling. *IEEE Journal of Lightwave Technology* **22**:11 (2004).

[102] G.J. Pearce, T.D. Hedley, and D.M. Bird. Adaptive curvilinear coordinates in a plane-wave solution of Maxwell's equations in photonic crystals. *Physical Review B* **71**:195108 (2005).

[103] T. Birks, D. Bird, T. Hedley, J. Pottage, and P. Russell. Scaling laws and vector effects in bandgap-guiding fibres. *Optics Express* **12**:69 (2004).

[104] W. A. Gambling, H. Matsumura, and C. M. Ragdale. Curvature and microbending losses in single-mode optical fibres. *Optical and Quantum Electronics* **11**:43 (1979).

[105] A. Argyros, T. Birks, S. Leon-Saval, C.M.B. Cordeiro, and P.St.J. Russell. Guidance properties of low-contrast photonic bandgap fibres. *Optics Express* **13**:2503 (2005).

[106] J. Lægsgaard. Gap formation and guided modes in photonic band gap fibres with high-index rods. *Journal of Optics A: Pure Appllied Optics* **6**:798 (2004).

[107] J.E. Goell. A circular-harmonic computer analysis of rectangular dielectric waveguides. *The Bell System Techical Journal* **48**:2133 (1969).

[108] E.A.J. Marcatili. Dielectric rectangular waveguide and directional coupler for integrated optics. *The Bell System Techical Journal* **48**:2071 (1969).

[109] Y. Ohishi, A. Mori, M. Yamada, H. Ono, Y. Nishida, and K. Oikawa. Gain characteristics of tellurite-based erbium-doped fiber amplifiers for 1.5 μm broadband amplification. *Optics Letters* **23**:274 (1998).

[110] A. Mori, H. Masuda, K. Shikano, and M. Shimizu. Ultra-Wide-Band Tellurite-Based Fiber Raman Amplifier. *Electronics Letters* **37**:1442 (2001).

[111] Jonathan H. V. Price, Tanya M. Monro, Francesco Poletti, Vittoria Finazzi, Julie Y. Y. Leong, Periklis Petropoulos, Joanne C. Flanagan, Gilberto Brambilla, Xian Feng, and David J. Richardson. Non-silica microstructured optical fibers for mid-IR supercontinuum generation from 2 μm - 5 μm. *Fiber Lasers III: Technology, Systems, and Applications, Proceedings of SPIE* **6102**:54 (2006).

[112] J.S. Wang, E.M. Vogel, E. Snitzer. Tellurite glass: a new candidate for fiber devices. *Optical Materials* **3**:187 (1994).

[113] R. Stegeman, L. Jankovic, H. Kim, C. Rivero, G. Stegeman, K. Richardson, P. Delfyett, Y. Guo, A. Schulte, and T. Cardinal. Tellurite glasses with peak absolute Raman gain coefficients up to 30 times that of fused silica. *Optics Letters* **28**:1126 (2003).

[114] J. Pottage, D. Bird, T. Hedley, J. Knight, T. Birks, P. Russell, and P. Roberts. Robust photonic band gaps for hollow core guidance in PCF made from high index glass. *Optics Express* **11**:2854 (2003).

[115] G. Pearce, J. Pottage, D. Bird, P. Roberts, J. Knight, and P. Russell. Hollow-core PCF for guidance in the mid to far infra-red. *Optics Express* **13**:6937 (2005).

[116] Herbert Burger, Udo Grunke, and Ivallo Gugov. Optical tellurite glasses for optical waveguide amplifiers and oscillators and process for producing them. *UK Patent* **GB 2378700** (2003).

[117] T. Delmonte, M.A. Watson, E.J. O'Driscoll, X. Feng, T.M. Monro, V. Finazzi, P. Petropoulos, J.H.V. Price, J.C. Baggett, W. Loh, D.J. Richardson, and D.P. Hand. Generation of Mid-IR Continuum Using Tellurite Microstructured Fiber. *Conference on Lasers and Electro-Optics (CLEO) 2006*, paper **CTuA4** (2006).

[118] J.W. Nicholson, A.D. Yablon, P.S. Westbrook, K.S. Feder, and M.F. Yan. High power, single mode, all-fiber source of femtosecond pulses at 1550 nm and its use in supercontinuum generation. *Optics Express* **12**:3025 (2004).

[119] P.S. Westbrook, J.W. Nicholson, K. Feder, and A.D. Yablon. UV processing of highly nonlinear fibers for enhanced supercontinuum generation. *Optical Fiber Communications Conference (OFC) 2004*, paper **PDP27** (2004).

Appendix: publication list

Journal publications

[1] **A. Wang**, G.J. Pearce, F. Luan, D.M. Bird, T.A. Birks, and J. C. Knight. All solid photonic bandgap fiber based on an array of oriented rectangular high index rods. *Optics Express* **14**:10844 (2006).

[2] J.C. Knight, F. Luan, G.J. Pearce, **A. Wang**, T.A. Birks and D.M. Bird. Solid photonic bandgap fibres and applications. *Japanese Journal of Applied Physics PART 1-Regular Papers Brief Communications & Review Papers* **45**:6059 (2006) (invited).

[3] T.A. Birks, F. Luan, G.J. Pearce, **A. Wang**, J.C. Knight, and D. M. Bird. Bend loss in all-solid bandgap fibres. *Optics Express* **14**:5688 (2006).

[4] **A. Wang**, A.K. George, and J.C. Knight. Three-level neodymium fiber laser incorporating photonic bandgap fiber. *Optics Letters* **31**:1388 (2006).

[5] **A. Wang**, A.K. George, J. Liu, and J.C. Knight. Highly birefringent lamellar core fiber. *Optics Express* **13**:5988 (2005).

Main conference presentations

[1] P. Domachuk1, N. A.Wolchover, M. Cronin-Golomb1, F.G. Omenetto1, K. Jang, J. Ahn, **A. Wang**, A.K. George, and J.C. Knight. IR Supercontinuum

in Compact Tellurite PCFs. submitted to *CLEO 2007* Baltimore (USA), May 2007.

[2] G.J. Pearce, F. Luan, J.M. Stone, **A. Wang**, T.A. Birks, J.C. Knight, A.K. George, D.M. Bird. Bend loss in all-solid photonic bandgap fibres. *EOS Annual Meeting 2006*, Paris (Porte de Versailles) (France), October 2006.

[3] **A. Wang**, A.K. George, and J.C. Knight. Three-level neodymium fiber laser incorporating photonic bandgap fiber. *Proceedings of CLEO 2006* **CTuI7**, Long Beach (USA), May 2006.

[4] **A. Wang**, A.K. George, J. Liu, and J.C. Knight. Highly birefringent lamellar core fiber. *Proceedings of ECOC 2005* **Tu1.4.1**, Glasgow (UK), September 2005 (invited).

[5] **A. Wang**, V.V. Ravi Kanth Kumar, A.K. George, J.C. Knight and P. St. J. Russell. Supercontinuum Generation using highly nonlinear PCF formed from tellurite glass. *Proceedings of PREP 2005*, Lancaster (UK) March 2005.

[6] **A. Wang**, V.V. Ravi Kanth Kumar, A.K. George, J.C. Knight and P. St. J. Russell. Extruded tellurite photonic crystal fibre. *POWAG 2004*, Bath (UK), July 2004.

Articles appeared in technical press from work carried out during this PhD

[1] Photonic Bandgap Fiber Forces a Weak Line to Lase. *Photonics Spectra*, USA, Breck Hitz (editor), **40**(7), 99-100, July 2006.

[2] Highly Birefringent fiber has Layered Core. *Photonics Spectra*, USA, Breck Hitz (editor), **39**(12), 84-85, December 2005.